MODELLING OF MULTISTAGE AXIAL-CENTRIFUGAL COMPRESSOR CONFIGURATION USING THE STREAMTUBE APPROACH

A Thesis
Presented to
The Academic Faculty

By

Abhishek Mishra

In Partial Fulfillment
of the Requirements for the Degree
Doctor of Philosophy in the
School of Aerospace Engineering

Georgia Institute of Technology

August 2019

MODELLING OF MULTISTAGE AXIAL-CENTRIFUGAL COMPRESSOR CONFIGURATION USING THE STREAMTUBE APPROACH

Approved by:

Dr. J. V. R. Prasad, Advisor
School of Aerospace Engineering
Georgia Institute of Technology

Dr. Yedidia Neumeier
School of Aerospace Engineering
Georgia Institute of Technology

Dr. Lakshmi N. Sankar
School of Aerospace Engineering
Georgia Institute of Technology

Dr. Jechiel I. Jagoda
School of Aerospace Engineering
Georgia Institute of Technology

Dr. Rakesh Srivastava
Senior Technical Manager
Honeywell International Inc.

Date Approved: March 12, 2019

The important thing is not to stop questioning. Curiosity has its own reason for existing. One cannot help but be in awe when he contemplates the mysteries of eternity, of life, of the marvelous structure of reality. It is enough if one tries merely to comprehend a little of this mystery each day. Never lose a holy curiosity.

- Albert Einstein

Dedicated to my wife, parents and sisters

ACKNOWLEDGEMENTS

I would like to acknowledge several people who have helped me directly and indirectly in making this thesis possible. First, I would like to thank my doctoral advisor Dr. J.V.R. Prasad for giving me the opportunity to work on this interesting research area related to compressor flow modelling. His support and guidance during the course of this work have been really helpful. Also, I would like to thank my co-advisor Dr. Yedidia Neumeier for helping me in overcoming several technical difficulties faced throughout my years at Georgia Tech. His insights about flow physics, readiness towards problem-solving and availability at non-conventional hours were highly motivational. He has always been a source of inspiration for me during the course of this project.

Next, I would like to thank Dr. Jechiel Jagoda for serving on my thesis committee and giving useful technical and non-technical suggestions whenever needed. His continuous support as a faculty member towards graduate students is highly appreciable. Also thanks to Dr. Lakshmi Sankar for serving on my doctoral committee. A great thanks to Dr. Yingjie Liu, Dr. Sung Ha Kang and Dr. Martin Short from school of mathematics for giving useful lectures on various numerical methods for PDEs and ODEs.

The financial support provided by Honeywell International Inc. in the completion of this research work is gratefully acknowledged. The useful feedback, several technical suggestions and data provided by Mr. Darrell James and Dr. Mahmoud Mansour have ultimately made it possible to benchmark the model simulations. Also, thanks to Dr. Rakesh Srivastava for participating in numerous discussions and for serving on my thesis committee.

Further, I would like to acknowledge my current and former labmates for their support and assistance: Satyam Patel, Yong-Boon Kong, Mark J. S. Lopez, Juan P. Afman, Chams E. Mballo, Vinodhini Comandur, Feyyaz Guner, and Robert Walters.

A heartfelt thanks to my wife Bhawna for her patience and love during my last few years at Georgia Tech. I am also grateful to my parents and sisters for their unwavering support.

TABLE OF CONTENTS

LIST OF TABLES

LIST OF FIGURES

NOMENCLATURE

Letter Symbols

$\dot{m}$	mass flow rate
A	cross-section area of the blade passage
B	B-parameter
b	streamtube width
c	speed of sound
C_f	skin friction coefficient
c_p	specific heat at constant pressure
C_q	heat loss due to cooling
c_v	specific heat at constant volume
D	diameter
D_f	diffusion factor
D_{sp}	separation degree factor
e	internal energy
F	physical flux vector
f	bounded function of Mach number

H	numerical flux vector
h	static enthalpy
L	characteristic wave amplitude
M	Mach number
m	mean-line coordinate
N_D	number of diffuser blades
N_I	number of impeller blades
p	static pressure
Pr	pressure ratio
Q	source vector
R	universal gas constant
r	radial location
Re	Reynolds number
S	minmod slope limiter
s	entropy
T	static temperature
t	time
Tr	temperature ratio
U	blade rotational speed/conserved variable vector
u	flow velocity

V mean-line velocity

V_p plenum volume

W velocity in relative frame

x axial location

Greek Symbols

α incidence or angle of attack

β blade angle

δ_{dev} trailing edge deviation angle

η mean-line inclination with respect to axial direction

γ specific heat ratio

λ friction factor

λ_i characteristic wave speeds (i = 1,2,3)

μ dynamic viscosity

Ω angular speed of rotation

ω_{loss} stagnation pressure loss coefficient

ϕ flow coefficient

ρ fluid density

σ blade solidity/slip factor

τ_w wall shear stress

θ_c camber angle

ξ_{ml} mixing loss factor

Subscripts

1 at the location 1

2 at the location 2

amb at the ambient condition

b at the bleed port

$char$ on the characteristic curve

D at the downstream node

e at the exit of blade row

i at the inlet of blade row

$leak$ over the tip leak

s stagnation value

t at the throat of inlet turning element

tip at the blade tip

U at the upstream node

Acronyms

BL Blade Loading

DF Disk Friction

$HECC$ High Efficiency Centrifugal Compressor

RC Recirculation

SUMMARY

Quasi-1D flow models based upon mean-line analysis are quite popular for design and performance evaluation of multistage axial and centrifugal compressors. However, they are not so readily used for analyzing the dynamic behavior of the compressor. In this work, an unsteady 1D axial-centrifugal compressor model is developed, whereby the stage elements, i.e., rotors and stators are modelled as diffusing streamtube elements. The analysis, being independent of any stage aerodynamic force and work terms, accurately predicts the performance of axial and axial-centrifugal compressors by the incorporation of various loss mechanisms compounding to stagnation pressure losses within stage elements. The off-design performance, especially close to the surge and choke line, is captured using novel models, particularly developed for incidence/sudden turning and mixing losses. These inlet turning and mixing loss models constitute an important feature of this work and are implemented by the inclusion of a single model parameter. This parameter called mixing loss factor, is then tuned for nominal shaft speed and is subsequently used to predict the compressor performance for different speeds ranging from 50% to 105%. The surge line is also accurately predicted by correlating the slope change criteria of constant speed characteristic curve to the instability onset point, which aligns well with the suitable choice of critical/stall incidence angle for the stage elements. Furthermore, the tuned model is used to predict the performance of the axial-centrifugal compressor at the aforementioned range of speeds. The diffuser loss, diffuser incidence angle and throat Mach number are calculated for the well-known UTRC-High Efficiency Centrifugal Compressor (HECC) and the results are validated with data from the literature.

The dynamic communication between two connected streamtubes is established using a novel boundary element called Compact Interface Element (CIE), which is developed by making use of the characteristics-based approach. The CIE achieves reference frame transformation between the successive diffuser elements and also incorporates complex loss

mechanisms due to sudden flow turning, mixing, shocks etc. Within the streamtube, 1D time-dependent conservation equations are solved using the second-order accurate Kurganov-Tadmor scheme, while at the boundary between the streamtubes, the dynamic compact element updates the interface conditions in time.

Another aspect of compressor operation is the observance of aerodynamic instabilities as the compressor is throttled towards stall. Several simulations indicate onset of instabilities close to the peak of compressor characteristic when a large plenum is present at the compressor end. Without any end plenum or low speed operation, it is found that few stable points exist on the positively-sloped portion of the characteristic curve. Importantly, Greitzer's B-parameter provides a good qualitative validation of the instability onset point. Further throttle closure, however, leads to oscillations, where the low frequency mode represents the fundamental axial mode of the compressor. It is shown that the instability modes obey a general Rayleigh's criterion, where they are affected by the phase between pressure fluctuations and shaft power addition oscillations.

The model finds applications in compressor design and analysis where the simulation results together with the test data using pressure signatures, provide the identification of stalling and choking stages.

CHAPTER 1

INTRODUCTION AND LITERATURE REVIEW

1.1 Problem Motivation and Background

In modern aircraft engines, the operation of compression system is vital for the performance of overall gas turbine. The thermal efficiency of Brayton cycle (or Joule cycle) which still constitutes the core thermodynamic cycle of air-breathing engines is limited by the temperature ratio (Tr) across the compressor. For a reversible adiabatic process, the thermal efficiency (η_c) can be related to a more commonly used performance parameter, i.e., compressor pressure ratio (Pr) as shown below:

$$\eta_c = 1 - \frac{1}{Tr} = 1 - \frac{1}{Pr^{(\gamma-1)/\gamma}} \tag{1.1}$$

where γ is the specific heat ratio of the working fluid, essentially air.

However, compression systems are often prone to aerodynamic instabilities especially when operating close to the peak of constant speed characteristic curve. Such instabilities manifest themselves in the form of rotating stall and/or surge which could be detrimental for the performance of overall system. A number of studies [1, 2, 3, 4, 5, 6] in the past have focused on analyzing these instabilities using theoretical, computational and experimental means. While extensive literature is available on the theoretical and experimental studies, recent advances in computational tools have made it possible to analyze three-dimensional aerodynamic instabilities in a multistage compressor [7].

From a designer's point of view, a novel computer program which could perform accurate and reliable pre- and post-stall analysis of a generic compressor is a highly sought after engineering tool. Mean-line methods employing quasi-1D analysis are quite popular for design and steady state performance evaluation of axial, centrifugal and mixed-flow

compressors. However, they have not been so readily used for dynamic performance analysis of the compressors used in gas turbines. It was shown by Moore and Greitzer [1] in their seminal work that an axial compression system operating in rotating stall has significantly different equilibrium curve than the axisymmetric characteristic. They further pointed out that the occurrence of surge does not only depend upon the operation of compressor and connected ducts, but also on the dynamics of entire system within which it is placed. Henceforth, the outcomes of this study indicate that it is imperative to predict the overall compressor performance operating at design and off-design conditions, and in particular, the inception of instabilities.

Heavy-duty gas turbines requiring high compression ratio generally employ twin-spool compressors: a Low Pressure Compressor (LPC) and a High Pressure Compressor (HPC). Some aero-engines, particularly those employed in rotorcraft, achieve this overall pressure ratio by combining axial stages with single or multiple high pressure ratio centrifugal stages. Earlier studies have focused on developing computational codes for either axial or centrifugal compressor. However, a unified modelling strategy encompassing both the axial and centrifugal components is necessary for such mixed flow machines. As a centrifugal compressor can produce higher per stage pressure ratio, issues like efficiency and stability of the overall axial-centrifugal compressor could be significantly different than the individual stages. For comprehensive understanding, it is essential to develop both steady and unsteady models as it is evident that a compressor undergoing transients performs quite differently compared to its steady state behavior.

A detailed analysis of rotating stall requires at least two-dimensional modelling approach with the inclusion of circumferential flow gradients. As an initial step, however, this work undertakes a quasi-1D unsteady flow analysis of axial-centrifugal compressor by modelling blade passages as diffusing streamtube elements with compact interfaces or velocity addition junctions. In this approach, each blade row has been modelled in its own reference frame, thereby making the approach more intuitive from the physical point of view. Figure 1.1

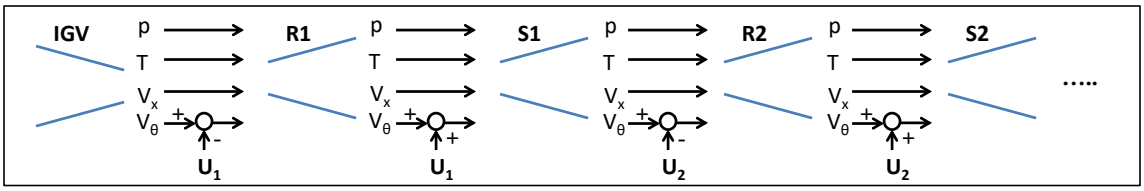

Figure 1.1: Multistage axial compressor modelled as successive diffusers with velocity addition junctions

shows a schematic diagram depicting multistage axial compressor stages modelled as successive diffusers with velocity addition junctions where the incoming velocity vector gets transformed into relative reference frame of the corresponding row through tangential velocity addition.

However, for any useful dynamic compressor analysis for surge/stall predictions, a steady state performance evaluation is vital, especially when the compressor is operating at off-design conditions. A constant speed operating line in such case is generally a smooth curve, often marked with a surge inception point. One could model the steady state performance by extracting the blade aerodynamic forces, and apply them as source terms in the flow governing equations. A number of earlier studies [8, 9, 10] have followed a similar approach for computing the steady state by time evolution of the unsteady flow equations. This approach is capable of capturing compressor performance. However, it is limited by a number of issues. First, for applying the distributed blade forces as source terms, it is required to have stage-wise compressor maps for each rotor and stator. In most cases, such detailed data is difficult to obtain or might be unavailable for a particular compressor. Further, this approach does not account for relative rotation between the rotors and stators, so acoustic events like wave transmission and reflection occurring at the row inlet cannot be properly captured. To overcome these limitations, this work focuses on solving the governing flow equations in curvilinear coordinate system within local reference frame, where the flow velocity always points in the direction of local mean-line. Further focus is on validating model results with test data of various compressors by the inclusion of novel loss model which estimates stagnation pressure losses occurring due to various mechanisms (details

of which are presented in sections 2.1.3 and 2.1.4). Using this more intuitive approach which is independent of any external aerodynamic sources, this work addresses the complex compressor issues like losses and instabilities.

1.2 Compressor Performance Evaluation

In this section, various approaches for modelling a compression system both in the steady state and transient operation are discussed. Broadly, the existing compressor simulation models could be classified into the following categories in terms of increasing complexity.

1. The so-called *lumped parameter model* [11] where only temporal dependence of flow variables is resolved. This leads to a coupled system of ordinary differential equations which can be advanced in time for obtaining both the steady state and transient results. DYNGEN, a popular computer program developed by Sellers and Daniele [12] at NASA Lewis Research Center for the performance analysis of turbojet and turbofan engines, is an example of such lumped parameter model. As a viable simulation tool, DYNGEN can perform transient analysis of many multi-spool engine configurations, given the relevant component maps and pertinent design-point parameters.

2. A *dynamic model* which includes both the spatial and temporal gradients in governing flow equations, thus results in partial differential equations. For modelling the compressor instabilities, it is necessary to include axial flow dependence as a locally generated stall event in a multistage configuration might not get detected in a lumped parameter model.

3. A detailed three-dimensional *CFD model* which solves viscous, compressible flow equations through the multistage compressor configuration.

Although three-dimensional CFD simulations are warranted for obtaining a detailed flow picture, complex modelling issues related to losses cannot be so easily dealt with, especially during preliminary design stages. A lumped parameter model, on the other hand, might be

insufficient for handling the matters of compression system instabilities. Hence, this work is in the direction of developing a quasi-1D dynamic model by retaining necessary terms in the governing equations, thus enabling the capture of crucial flow physics.

1.2.1 Stable Operation and Compressor Map

The basic task of a compressor used in a gas turbine is to increase the air pressure so that the combustion process becomes efficient. A compressor can operate at various shaft speeds and mass flow rates, hence its performance is generally expressed as a function of percent of corrected shaft speed in the form of so-called *compressor map*. A compressor map is generated for a particular compressor after core rig testing or by detailed computer simulations. A typical compressor map, as shown in Figure 1.2, depicts total pressure ratio and adiabatic efficiency versus corrected mass flow for various shaft speeds. The design

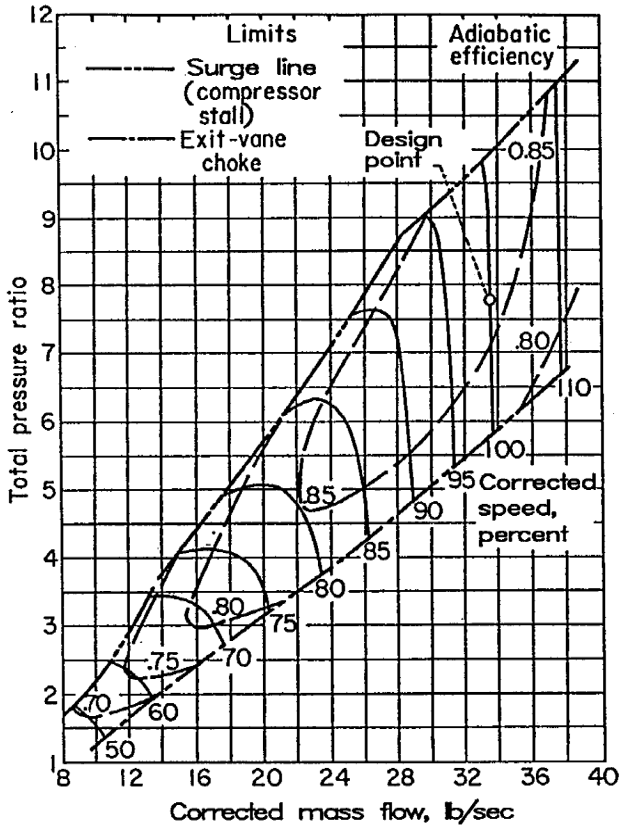

Figure 1.2: A compressor map showing surge line and choke line, Ref. [13]

point is marked on the map at 100% speed, shown by an open circle in Figure 1.2. At low mass flow rates, the stable operation of the compressor is limited by the aerodynamic instabilities as shown by the surge line on the left side of the map. On the right side, there is a slanted choke line which further limits the compressor operation at high mass flow rates. Under the stable operation, small transients generated due to flow disturbances die down and the compressor settles into steady state given by a fixed point on the compressor map. In practice, the steady state or equilibrium point can be determined by the intersection of exit throttle curve and the compressor operating line.

1.2.2 A Review of Previous Modelling Approaches

Several conceptual studies have focused on the development of modelling tools that could generate and further analyze such compressor performance curves. During model development virtually a number of design and flow parameters appear, which could easily become unmanageable to be quantified accurately. Mean streamline aerodynamic analysis due to its owning simplicity and usefulness have turned out to be a preferable choice by many compressor designers.

Veres [14] at Glenn Research Center developed a mean-line computer code called COMDES for conceptual sizing of axial and centrifugal compressors during early design phase. The code which was based on the compressible fluid flow equations could be used to evaluate compressor performance both at design and off-design conditions. Particularly at the off-design operation, the compressor stages were matched aerodynamically by varying inlet guide vanes and stator geometry angles. At part-speed operation, this variable blade geometry helped in having a safe compressor operation by improving the overall surge margin. At the nominal speed, COMDES was designed to provide a better understanding of the aerodynamic parameters like diffusion factor and stage loading. The losses due to rotor incidence and inlet guide vanes reset angle were estimated at off-design using simple empirical models. Further correlations for compressor surge were proposed for NASA stage

37 and NASA 74-A compressors, providing accurate estimates for most speeds.

Another compressor research work at NASA by Steinke [15] led to the development of STGSTK program. This program which was written in FORTRAN implemented mean-line stage-stacking method which could be used for predicting both the stage and cumulative compressor performance. STGSTK which was based on one-dimensional compressible flow equations was relatively simple in comparison to two and three-dimensional models, and minimized model complexity to maintain high computational efficiency. The code also provided with an option to input non-dimensional stage characteristics or to calculate the same using aerodynamic inputs available from other compressor design codes. Some correlations were used from experimental data to model real flow effects induced by high inlet blade relative Mach numbers. Further options were also provided to modify the rotor design deviation angles at the off-design conditions. The real flow adjustments were made to stage characteristic for part-speed operation by expanding the flow coefficient range and changing the stage adiabatic efficiency level.

Schmidt [16] developed an off-design axial-flow compressor code at NASA Lewis Research Center, which could predict the off-design aerodynamic performance of fans and multistage compressors. This program, being an improvement on previous studies, modelled two-dimensional steady axisymmetric flow in the meridional plane (r-z) and used streamline curvature method for performing calculations at the stations located outside the blade rows. This program included empirical loss and deviation correlation models and was capable of incorporating bleed flows as well as blade geometry adjustments for the first five stators. As only the profile and shock losses were taken to be the stagnation pressure loss mechanisms, the program, as a result, validated well the performance of fans and moderately-loaded multistage compressors. However, it required large reset adjustments for highly-loaded multistage compressors.

Johnson [17] developed one-dimensional, stage-by-stage steady model for performance analysis of multistage axial compressor and validation of the loss and deviation correlations.

His proposed stage stacking method was different from the traditional simplified approaches, in a sense that it did not require any stage characteristic, but it calculated the stage performance using the mechanism of losses and blade exit flow deviation correlations. The loss and deviation curves, which were obtained using two-dimensional cascade tests, depicted large drag/loss coefficients for high positive and negative blade incidences, and large flow deviations for only high positive incidences. The effect of boundary layer blockages were simulated by reducing the inlet and exit flow areas to match the design-point axial velocities given in the literature. Overall, the two compressors undertaken for model calibration and analysis studies showed good match with the test data, though predicted higher choked flow rates for most speeds. As only generic correlations were used, it was repeatedly stressed that the loss and deviation curves can be replaced as desired by the user.

Several years of compression system modelling efforts at Arnold Engineering Development Center (AEDC) resulted in the development of a compressor program called DYNamic Turbine Engine Compressor Code, DYNTECC [18]. This program, which was developed for quasi one-dimensional unsteady analysis of multistage compressors, numerically solved Euler equations with aerodynamic source terms using an explicit finite difference method. The stage force and work inputs were provided by a set of quasi-steady characteristics which incorporated various regions like pre-stall operation, rotating stall and reverse flow region. Since a compressor operating under rotating stall has relatively quick dynamics, the quasi-steady characteristics were modified using a first-order lag equation for accurate simulations of the post-stall events. The analysis capabilities of the program were demonstrated through unsteady flow simulations and were validated with experimental results. Stability limits of single and dual-spool compressors were detected at various speeds and the stall initiating stage was identified using the pressure traces. Post-stall analysis of the ten-stage single-spool axial compressor showed the occurrence of rotating stall and validated the stage behaviors well with the experimental data. Further, the single-spool distortion analysis investigated the effects of inlet temperature and pressure distortions, in which case

the temperature distortions were found out to be more severe and detrimental in reducing the overall stall margin.

To demonstrate the applications of CFD analysis on multistage compressor performance and design, Mansour and co-workers [19, 20] from Honeywell Engines & Systems used a three-dimensional, viscous code called "APNASA" based on an Average-Passage Flow Model (originally developed by J. J. Adamczyk [21] at NASA Glenn Research Center), for steady flow simulations through the multistage compressors. The code, which was first used to validate and calibrate the performance of two different multistage axial-centrifugal compressors, eliminated the empiricism associated with the axisymmetric through-flow models by accurately capturing the blade-passage boundary layers and exit flow deviations. Overall, the radial distribution of pressure and temperature obtained from this CFD code matched well with the test data, and further, detailed flow features near the end wall regions were predicted accurately. Moreover, the axisymmetric through-flow model was employed in conjunction with the APNASA code to obtain the design-intent conditions. The design-intent profiles were then specified as the inlet conditions for single-row analysis of a new compressor whose results compared well with the multistage APNASA results if the right amount of blockage was used. Through detailed blade design and optimization, the results from APNASA program were deemed quite good and led to significant cost savings in a new engine development program.

Turning attention to the centrifugal and mixed-flow compressors, Aungier [22] performed mean streamline analysis of centrifugal compressor stages and compared the predictions with experimental data of over one hundred different stages. The work was mainly focused on impeller performance prediction methods and complemented previous models developed by the same author for vaned and vaneless diffusers [23, 24]. The model included work input terms due to impeller blades, windage and disk friction, seal leakage, and recirculation. The slip factor formulation was based on the paper by Wiesner [25], which holds valid when the impeller mean-line radius ratio is below some limiting value. Additionally, a corrected

slip factor was used when the actual radius ratio exceeded this limiting value. Extensive validation studies were conducted for stages with flow coefficients ranging from 0.009 to 0.15 and the results were found out to be good for turbocharger stages having pressure ratios up to 3.5.

NASA designed a single-stage high pressure ratio centrifugal compressor called CC3 in 1970s for use in advanced gas turbine engines, power generation and rotorcraft applications. The CC3's impeller which could be used with both vaned and vaneless diffusers was computationally analyzed by Kulkarni *et al.* [26]. The undertaken RANS computations investigated two turbulence models, i.e., k-ϵ and k-ω with nominal (6.8 million grid points) and refined (14 million grid points) meshes. Considering overall compressor performance, the refined k-ω model predicted total pressure ratio and efficiency within one percent of the test data, and was generally more accurate than both the nominal and refined k-ϵ cases. However, the k-ω model predicted lower choked flow rate than the data due to slightly larger growth in pressure side boundary layer leading to extra blockage. This study was useful in understanding the choice of turbulence model and grid density on the compressor performance predictions.

Recent collaborative efforts between NASA and United Technology Research Center (UTRC) towards the development of a new compressor have led to "High Efficiency Centrifugal Compressor" (HECC) which has higher overall pressure and temperature ratio than the CC3 compressor. With design intent adiabatic efficiency of more than 88% ($\eta_{p,tt}$), HECC was successfully tested by Braunscheidel *et al.* [27] at NASA Small Engine Components Test Facility at Glenn Research Center. The test results demonstrated overall lower pressure ratios and adiabatic efficiencies than the design intent, however, comparison of spanwise distribution of local pressure coefficients at impeller exit was quite good. It was found that the minimum loss of each sub-component did not occur at the same flow rate due to discrepancies with the design-intent performance. The HECC choked due to the choking of the vaned diffuser leading to higher losses close to the choked flow rate. But the diffuser

loss levels were significantly reduced as the compressor was throttled towards the stall.

Galvas at NASA Lewis Research Center [28] worked on developing a FORTRAN program for predicting the off-design performance of the centrifugal compressors. Empirical correlations were used for modelling losses at the nominal and part-speed operations. A brief theoretical approach on enthalpy loss calculations particularly due to inlet guide vanes, inducer non-optimal incidences, blade-loading, skin and disk friction, recirculation, vaned and vaneless diffusers was presented. However, the shock losses were neglected throughout the program. Importantly, the compressor operating range was correlated with the vaned diffuser leading edge Mach number with an assumption that this component governed the compressor surge point location. The choking, on the other hand, was controlled by the inducer at 100 percent speed and by the vaned diffuser at part-speeds. Overall, the model predicted pressure ratios quite well, however, predicted efficiencies were considerably lower than the experimental values. While operating close to the nominal speed, choked flow rates were also not predicted adequately as the choking was mainly governed by the impeller rather than the vaned diffuser. Some of the predictions could have been better if shock losses were included in the analysis.

In study by Li *et al.* [29], an axial-radial combined compressor was simulated through the numerical solution of 3D RANS equation with Spalart-Allmaras turbulence model. Specifically, the focus was on analyzing the influence of circumferential inlet distortion on centrifugal impeller inlet flow at various spanwise locations. The wake characteristics varied along the span with maximum distortion and losses occurring at low blade span, i.e., near the hub. Blade loading which is important from the structural point of view, turned out to vary in periodic fashion versus stator pitch angle, with its maximum amplitude occurring at the blade leading edge.

1.2.3 Parametric Effects on Compressor Performance

Variability in a number of geometry and flow parameters can affect the compressor performance both in positive and negative sense. A brief overview of few of the important parameters like blade sweep, dihedral, swirl distortions, tip clearance etc., is presented in this section.

It has been reported in literature [30] that compressor blade aerodynamic efficiencies can be improved by introducing forward sweep and/or positive dihedral, i.e., having a high obtuse angle between the suction surface and end-wall. Sasaki & Breugelmans [31] studied sweep and dihedral effects in a linear compressor cascade using three-dimensional measurements inside the blade passage. In this analysis, both forward and backward swept blades were investigated, where the sweeping was introduced only near to the end-wall regions. In their experimental research, the forward swept blades generally led to lower losses when the incidences were small. On the other hand, the losses were higher or nearly the same as the straight blades for larger incidences. This was mainly due to the flow separation that occurred on the blade suction surface around mid-span as a result of large adverse pressure gradients. The backward swept blades, in comparison, always resulted in higher losses than the straight blades. Incorporation of positive dihedral was more effective than forward sweep, which lowered the losses over a wider range of incidence angles. Overall, the flow measurements showed that, in most cases, forward sweep and positive dihedral led to lower losses.

Garzon & Darmofal [32] worked on quantifying the role of blade geometric variability on compressor performance indicators typically aerodynamic performance, pressure ratio, and overall efficiency. A principal-component analysis (PCA) based approach was used to build a high-fidelity probabilistic model which was then combined with a compressible, viscous blade-passage analysis to estimate the aerodynamic performance statistics. For their flank-milled integrally bladed rotor, the impact of geometric variability was found out to be low, however, for elevated geometric variability levels the mean loss turned out to be

20% higher than the nominal value. A similar result was also obtained for a multistage compressor using a mean-line model, where elevated geometric variability levels resulted in near 1% drop in the compressor efficiency.

The gap between blade tip and end-wall plays a major role in the local and overall compressor aerodynamic performance. In general, increasing the blade tip clearance deteriorates the compressor performance by lowering down the pressure ratio and overall efficiency due to the increased flow leakage. In first-of-a-kind research, Graf *et al.* [33], studied the effect of non-axisymmetric tip clearance on axial compressor performance and stability through theoretical and experimental tools. It was found that in comparison to axisymmetric tip clearance, this kind of clearance turned out to be more detrimental, which lowered the compressor performance and reduced the stall margin significantly. Using a reduced-order fluid-mechanic model, the authors were able to identify the key model parameters like local pressure rise characteristic slope, flow inertia parameter, wavelength of asymmetry, which manipulate the sensitivity of clearance asymmetry on the compressor performance. Further, they were able to validate the roles of these parameters using the test results. Their parametric analysis concluded that (a) compressor with steep characteristic close to the peak pressure is more sensitive to tip clearance asymmetry, (b) decreasing the wavelength of asymmetry/nonuniformity improves the overall stall margin.

Sheoran *et al.* [34], investigated the performance of a single-stage compressor in the presence of inlet swirl distortions using three-dimensional CFD analysis. A realizable k-ϵ turbulence model with wall functions was employed for performing flow computations using the commercial code FLUENT. An interesting part of their research was detailed classification of various swirl patterns using three main swirl descriptors, namely Swirl Intensity (SI), Swirl Directivity (SD) and Swirl Pair (SP). For example, the *twin swirl* pattern shown in Figure 1.3 with fixed SI value and no overall direction is denoted by $SD = 0$ and $SP = 1.0$. However, as co-rotating swirl becomes dominant, the *offset swirl* pattern with fixed SI value gets identified by $SD > 0$ and $0.5 < SP < 1.0$. Through their

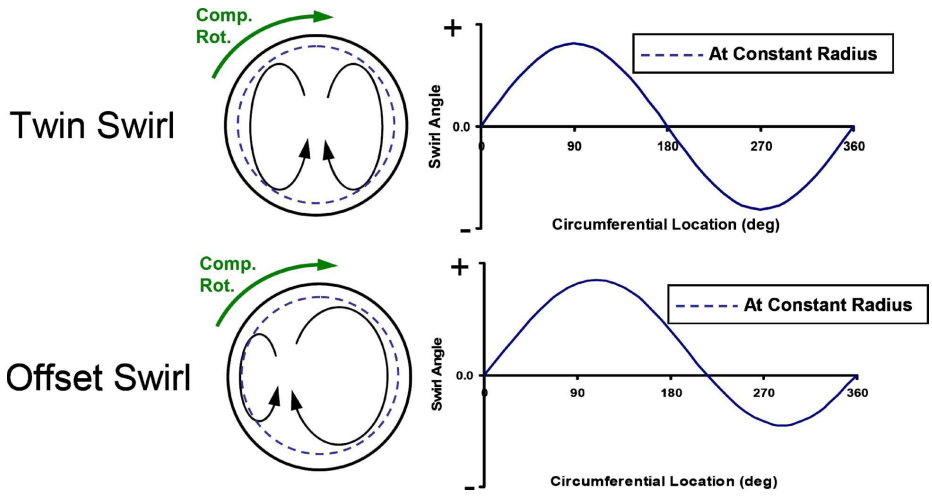

Figure 1.3: Twin swirl and offset positive swirl patterns at Aerodynamic Interference Plane (AIP), Ref. [34]

combined compressor-swirl generator CFD analysis, it was shown that co-rotating/positive bulk swirl decreases the operating flow rates, pressure and temperature ratios, while counter-rotating/negative bulk swirl increases them. Other complex inlet swirl patterns like twin and offset swirl result in intermediate values. In their analysis, the shifts in compressor curves were mainly due to the reduction in adiabatic efficiencies as a result of distorted inflows.

It is common for centrifugal compressors to operate with both vaned and vaneless diffusers with former being more common industry practice. Inoue & Cumpsty [35] performed experimental investigations of flow discharging from impeller to vaned and vaneless diffusers. Their test results showed that vaned diffuser, in comparison to vaneless diffuser, led to significant amounts of flow reversal close to vane leading edges. However, the strength of reversed flow became weak as the number of vanes was increased. The compressor operation with vaned configuration was clearly helpful in reducing the flow unsteadiness and circumferential nonuniformity within the diffuser.

1.2.4 A Brief Discussion on Loss Mechanisms

Achieving high efficiency for turbomachines is a major goal of most designers and gas-turbine operators. As a turbine operates in favorable pressure gradient environment, it is

relatively easier to design a high efficiency turbine compared to a compressor. However, in recent years due to the advancements in computational technologies, CFD and other detailed design tools have played an important role in the development of highly efficient compressors [27]. This section is devoted to a short discussion on various mechanisms which contribute to the loss of stagnation pressure, hence reduce the efficiency of turbomachines.

Denton in his seminal paper [36], utilizing over 20 years of experience, has given a comprehensive overview of various loss mechanisms occurring in turbomachines. He presented the idea that losses should be dealt in terms of entropy generation rates as by using this approach, useful thermodynamic relations can be easily formulated from basic theory without loss of generality. Further for a compressor, the flow is mostly adiabatic and for small changes between the static and stagnation conditions, the stagnation pressure loss (shown as overall pressure ratio, p_{s2}/p_{s1}) and efficiency (η_c) can be represented in terms of entropy change (Δs) as shown below:

$$\frac{p_{s2}}{p_{s1}} = \exp(-\Delta s/R) \tag{1.2}$$

$$\eta_c = 1 - \frac{T\Delta s}{\Delta h} \tag{1.3}$$

Some of the important mechanisms leading to direct or indirect efficiency reduction in axial and centrifugal compressors are described next.

Boundary Layer Loss

Due to their viscous nature, boundary layers are inherently non-isentropic and lead to significant entropy generation. Inside compressor blade rows, the boundary layers are mostly turbulent and depending upon flow conditions could be quite thick on end-walls and near blade aft regions. The complexity of boundary layers is explained in a series of four papers by Halstead *et al.* [37, 38, 39, 40], where they dedicated their efforts in analyzing, assessing and describing the development of boundary layers in axial compressors and

turbines. Overall, the entropy generation within two-dimensional boundary layers can be calculated by figuring out the dissipation coefficient C_D (see Ref. [36]), for various Reynolds numbers and integrating the same over blade surfaces.

Incidence/Turning Loss

Except at the design point, the stages of a multistage compressor are rarely perfectly matched. Flow entering a stage element at off-design conditions has to turn suddenly to follow the blade profile. This leads to the loss of stagnation pressure known as incidence or turning loss, with possible leading edge flow separation.

Mixing Loss

Mixing occurs in regions of high shear typically close to the blade trailing edges and end-walls. Wake issuing from the trailing edge becomes uniform as the high momentum flow mixes up with the low momentum flow. This process essentially creates entropy and is referred to as mixing loss.

Shock Loss

Particularly in transonic compressors, the flow in front rotors in blade reference frame could be supersonic. This results in the formation of shocks attached to the blade leading and trailing edges, thus leading to losses. Depending upon the Mach number of incoming flow, the loss of stagnation pressure could be significant. The expression for total pressure ratio across a normal shock for calorically perfect gas is given by

$$\frac{p_{s2}}{p_{s1}} = \left[\frac{(\gamma+1)M^2}{(\gamma-1)M^2+2}\right]^{\frac{\gamma}{\gamma-1}} \left[\frac{(\gamma+1)}{2\gamma M^2-(\gamma-1)}\right]^{\frac{1}{\gamma-1}} \tag{1.4}$$

The above expression shows that the loss of stagnation pressure is approximately 1% for $M = 1.23$, however reaches staggering 28% for $M = 2.00$. While shocks are effective

means of compression, it is generally advisable to reach the desired compression through a series of oblique rather than normal shocks.

Tip Leakage Loss

Flow leaks from the high pressure to low pressure side due to the gap between blade tip and end-wall. A jet issuing from the gap mixes up with the suction side flow and leads to losses due to (a) irreversible expansion and mixing process, (b) increase in mass flow rate within the blade passage causing reduction in the pressure rise.

Heat Transfer Loss

Any transfer of heat from a high temperature to low temperature zone is an irreversible process and creates entropy. Although most compressors operate with nearly adiabatic conditions, small turbochargers could have significant amount of heat loss to the surroundings. However, the heat transfer losses are generally important for turbines where the coolant fluid takes some of the heat away from blades causing a lower overall machine work output.

End-wall and Trailing Edge Losses

The losses close to the end-wall region in a compressor cascade are dominated by the secondary flows which arise as a result of thick boundary layers and significant flow turning. As the boundary layers develop in adverse pressure gradient environment, they tend to separate and promote the formation of secondary flows like passage vortices. Further, the boundary layers leaving the blade surface at the trailing edge mix out and lead to additional trailing edge losses. A detailed analysis of these complex flows is only possible through the solution of three-dimensional Navier-Stokes equations.

Disk Friction Loss

In a centrifugal compressor, the flow leaving the impeller leaks into the side of backplate and creates entropy through viscous torques which act on the rotating disk. This is known as disk friction loss and can be estimated by calculating the skin factor coefficient on the rotating surfaces exposed to the flow. Additional entropy generation might occur when the heat released due to viscous dissipation mixes up with the mainstream flow and so increases the work input of downstream stages, if any.

In their seminal work, Koch and Smith [41] from General Electric company devised a method for predicting the efficiency potential of both low and high-speed compressors at design conditions. They considered a total of four sources of losses, namely blade profile loss, end-wall boundary layer loss, shock loss and part-span shroud loss. Further, they validated their method with test data for a number of low and high-speed compressors with wider ranges of aspect ratio, solidity, clearance, stagger angle and reaction. In another study by Koch [42], a stall prediction methodology was developed where the maximum pressure rise capability of multistage axial compressors was correlated with passage geometry parameter. Effects of a number of parameters like Reynolds number, blade tip clearance, blade axial length, vector diagrams etc., were identified. Being simple in approach, this kind of stall prediction methodology can be employed for preliminary design analysis.

While the literature review in this section highlights the importance of compressor performance prediction methods at various stable operating conditions, it is equally important to have a good idea of prediction methodologies when the stable operation is no longer possible and the compressor encounters instabilities.

1.3 Overview of Compressor Instabilities

Instabilities in compression systems have always been a crippling problem for gas turbine engine designers and airline operators. Fundamentally, a state of any dynamical system

can be said to be unstable if a small disturbance in system variables grows in space or time, necessarily unaided by any external forcing. Numerous studies in the past have tried to model a compressor by considering it as a dynamic component of an overall system, connected to various ducts and volumes. One of the well-known research work in this regard was conducted by Greitzer [43] where he considered a compact pump connected to a duct cavity on its discharge side and interfaced with the ambient on its suction side. The duct cavity was joined into a plenum with a throttle connected at its end. The mass flow through the entire system was controlled by the throttle which essentially discharged to the same pressure as the ambient. Greitzer modelled the pumping system as a lumped parameter model by developing a mechanical analogy to mass-spring-damper configuration. Using this system, he was able to prove that in the case of a large end plenum, the system becomes dynamically unstable when the pumping characteristic curve (i.e., pressure versus mass flow plot) changes its slope from negative to positive.

The study conducted by Greitzer was quite novel in its approach and can be used to elucidate the important concepts of static and dynamic instability [44].

- *Static Instability*, is mainly operational in nature and is related to steady state characteristics of the system. For a compression system, the static instability arises when the slope of compressor characteristic curve becomes larger than the slope of throttle curve. In mass-spring-damper system, this corresponds to having negative spring constant, essentially resulting in exponential growth of disturbances. Mathematically, this can be expressed as

$$S_C > S_T \tag{1.5}$$

  where S_C is the slope of compressor characteristic curve and S_T is the throttle curve slope. This criterion for static instability can be observed on the left side of Figure 1.4, where the points A and C are stable and B is unstable.

- *Dynamic Instability*, on the other hand, is related to unsteady behavior created due

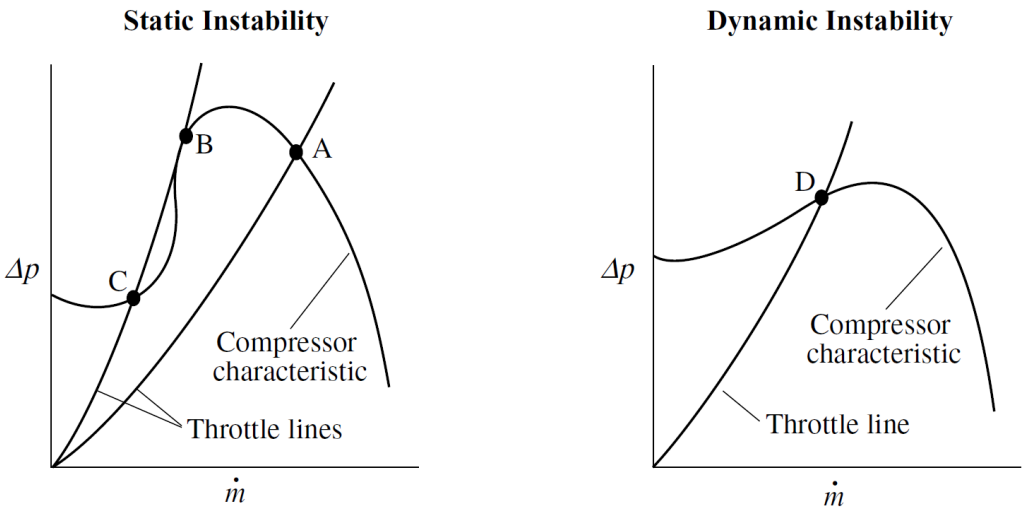

Figure 1.4: Static and dynamic instabilities in a compression system, Ref. [44]

to flow imbalances inside the compression system and the ability of throttle to provide necessary damping. In the second order mass-spring-damper system, dynamic instabilities arise when the overall system damping becomes negative. This leads to a general instability criterion, which can be expressed in terms of well-known B-parameter [45] as shown below:

$$S_C \cdot S_T > \frac{1}{B^2} \tag{1.6}$$

The B-parameter itself is defined in terms of compressor parameters as

$$B = \frac{U}{2c}\sqrt{\frac{V_p}{A_c L_c}} \tag{1.7}$$

where U is compressor shaft speed, c is acoustic speed, V_p is volume of end plenum, A_c is compressor duct area, and L_c is length of compressor duct.

While the static instability is just an operational limit, it is the dynamic instability which is generally observed in practice when the compressor is throttled to low mass flow rates.

1.3.1 Rotating Stall and Surge

The aerodynamic instabilities in compression system appear in the form of two modes: rotating stall and surge. *Rotating Stall* which was first observed in 1940's, can be described as a single or multiple propagating stall cells in circumferential direction, which move from blade to blade in the direction of compressor shaft rotation. This produces continuous loading and unloading of the blades resulting in large blade vibrations, which could ultimately lead to structural failures. It should be further noted that due to the system hysteresis effects, the rotating stall initiated by closing of throttle cannot be mitigated just by opening it again. *Surge*, on the other hand, is often described as an instability of compression system rather than just of compressor itself, and is a large amplitude oscillation which, once initiated, results in complete breakdown of flow inside the compressor.

Owing to considerable interest, several researchers have focused their attention on developing fundamental understanding of rotating stall and surge. Any fluid dynamic model development in this direction, in turn, has always focused on the notion that the surge is a large amplitude unsteady oscillation of annulus-averaged flow, which is independent of the circumferential location. Hence, many unsteady 0D or 1D modelling approaches, bereft of gradients in the circumferential direction have proved to be sufficient for the simulation of a compressor surge cycle. On the other hand, rotating stall is a circumferentially propagating non-axisymmetric disturbance, but can be made steady in a frame of reference moving at a fraction of shaft speed, essentially the stall speed. Moore [3] followed a similar approach for analyzing rotating stall in multistage axial compressors, and modelled stall as a modal perturbation propagating with some unknown speed. The propagation speed was found by solving the eigenvalue problem obtained by matching pressure across the complete system including compressor, inlet and exit ducts, guide vanes and plenum. However, experiments performed by Day [5] clearly indicated that modal perturbations are not always present prior to stall, and when present, have little effect on the formation of stall cells. His research led to the conclusion that modal perturbations and formation of finite amplitude stall cells are two

different phenomena, occurring roughly at the peak pressure of compressor characteristic. An earlier work by Emmons *et al.* [46] was focused on analyzing the rotating stall using linearized analysis by assuming infinitesimal disturbances. As his analysis undertook only small deviations from the equilibrium position, it was not capable of predicting the finite amplitude stall cells.

Non-linear models, due to the limitations of linear models, have been the focus of many subsequent studies. Moore & Greitzer [1, 2] built a general non-linear fluid dynamic model to encompass both rotating stall and surge type of disturbances. Their research was mainly concentrated on the evolution of post-stall transients and role of different parameters on the final state of the system. Hot wire measurements taken by Greitzer at rotor inlet in another study [45] are in shown Figure 1.5. An often mentioned distinction between the rotating stall and the surge cycle can be seen from the figure, that the frequency of rotating stall is typically one order of magnitude higher than that of the surge.

The value of earlier described B-parameter plays a key role in the evolution of post-stall transients into pure rotating stall or pure surge. Greitzer found that for their compression system model, above some critical value of B-parameter, large amplitude surge like oscillations

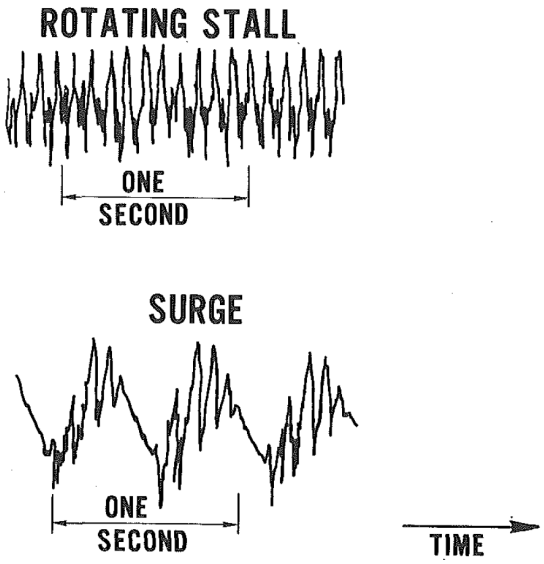

Figure 1.5: Rotating stall and surge cycle measurements at compressor inlet, Ref. [45]

get encountered at the stall line; while below this critical value it is the rotating stall which gets exhibited. One way to manipulate B-parameter is by changing the plenum volume at the compressor end, thereby enabling the appearance of both kinds of instability modes. Another parameter studied was the compressor length, and it was shown that the smaller values of compressor length prefers evolution of transient behavior into surge, whereas larger values tend to stabilize into rotating stall.

1.3.2 Instability Onset Criteria

It is quite clear that several previous researchers have tried to develop a generalized instability onset criterion which could hold valid for various geometry parameters and compressor designs. Leiblein [47] proposed a parameter called *Diffusion Factor* (D_f), based upon the growth of boundary layers on suction surface in adverse pressure gradient environment to predict the onset of stall. His experimental work on two-dimensional cascades showed that around D_f value greater than 0.6, the losses increase rapidly leading to flow separation and stall. However, stall of a particular stage barely represents the instability of entire compressor. It is well-known and has also been reported in the literature that a multistage compressor can operate in a stable manner with one or several stalled stages.

Another popular instability criterion which is still in use is the one proposed by Dunham [48]. He stated that the rotating stall would be initiated at the peak of total-to-static pressure rise characteristic (ψ_{TS}) plotted versus axial velocity parameter (ϕ). This criterion has been successfully derived by other investigators also. Most extensive of all is Moore-Greitzer's work on compression systems as described earlier. Using a lumped fluid dynamic model, they were able to re-derive the zero-slope of pressure characteristic as the instability criterion. It was also shown by Greitzer [43] that the zero-slope might not be a necessarily valid criterion for all the compressors. Exceptions were found for high-speed compressors where the stall inception occurred on the negatively-sloped region of the characteristic curve.

1.4 Objectives of this Thesis

The literature review and discussion presented in this chapter outline the important compressor related issues like performance evaluation at various speeds, losses estimation and compression system instabilities. While some work has been done on the mean-line compressor code development, fundamental stagnation pressure loss mechanisms are still unclear to many compressor designers. Specifically at the off-design operation, when the stages do not operate at their design blade angles, moderate to severe blade stalling and so generated flow non-uniformities give rise to stagnation pressure losses. Developing accurate models for capturing these losses based on physical arguments is a challenging task and sometimes require tuning of several model parameters. In the scenario of HPC being a centrifugal stage, a unified mean-line approach with a general loss model for axial-centrifugal compressor has still not been pursued.

During the unsteady compressor operation, rotating blade rows communicate with stationary ones through the propagation of acoustic waves. In a compressor simulation program, it is important to establish this communication through a dynamic interface between the row elements. Regarding the compressor stability, Greitzer's lumped system model [45] for axial compressors has been an accepted norm in the turbomachinery community. However many underlying assumptions in his model limit it to be used as a generalized stability criterion. It would be interesting to observe the behavior of overall configuration when a centrifugal stage gets attached at the end of axial stages. Practical experience suggests that under some conditions, an axial-centrifugal compressor can operate in stable manner even if the front stages are stalled. In this regard, it would be important to figure out where the overall compressor surges leading to the complete breakdown of flow.

This work addresses the above issues by developing a quasi-1D unsteady compressor fluid dynamic model applicable for both the axial and centrifugal configurations. Objectives of this work are identified as follows:

- Develop a steady flow model for axial-centrifugal compressor by capturing essential stagnation pressure losses using a novel loss model with minimum tuning parameters.
- Establish dynamic interaction between two neighboring blade rows rotating relative to each other and integrate it within the underlying numerical scheme employed for the solution of governing equations.
- Perform dynamic analysis of the axial-centrifugal compressor for various operating conditions and estimate the instability initiation point on the compressor curve.
- Demonstrate compressor stalling and choking phenomena using dynamic simulations and further investigate "abrupt stall" occurrence on the negatively-sloped region of the compressor characteristic.

Subsequent chapters of this thesis are organized as follows. *Chapter 2* discusses steady and unsteady fluid dynamic model along with various loss models using streamtube analysis for the axial-centrifugal compressor. *Chapter 3* presents the numerical solution of governing equations and the dynamic compact interfaces along with the boundary conditions. *Chapter 4* assesses the compressor model and validates the steady state results against the measured data. Results for the axial-centrifugal compressor and UTRC-HECC are also presented. *Chapter 5* explores compressor instabilities through dynamic simulations and also investigates compressor choking, low-speed stall and abrupt stall phenomena. *Chapter 6* performs sensitivity studies on compressor performance with respect to the geometry parameters. *Chapter 7*, finally, presents conclusions of this thesis and recommends directions for future research work.

CHAPTER 2

STREAMTUBE FLUID DYNAMIC MODEL DEVELOPMENT

A compressor performance model development requires detailed fluid dynamic analysis of the machine and associated components under various operating conditions. In this chapter, a quasi-1D streamtube based mean-line analysis of flow through the compressor blade passages is discussed. For a stage element, say rotor or stator, the annular space between the hub and shroud forms a streamtube, and the aerodynamic blades guide the flow through this streamtube. Similarly, a multistage compressor can just be considered as a combination of consecutive streamtubes with alternating reference frames.

In the next sections, theoretical steady and unsteady models based upon conservation principles applicable for axial, centrifugal or mixed flow compressors are presented. For the axial stages considered in this study, the mean-line inclination with respect to the axial direction is not very significant. Therefore, while analyzing the flow just through the axial stages, the contribution of mean-line inclination to streamtube cross-sectional area has been particularly ignored.

2.1 Steady State Model

For evaluating the steady state performance, the blade passage within a stage element, say a rotor or stator, is modelled as a diffuser section which continuously raises the static pressure. As flow enters the rotor from stator or vice-versa, there is a jump in stagnation pressure and stagnation temperature due to the tangential velocity addition or subtraction as shown in the Figure 1.1. In the diffuser section, stagnation temperature can also change due to the work done by centrifugal force if the mean-line has significant radial inclination. But in the case of pure axial stage with relatively small mean-line inclination, the mean-line radius remains nearly constant. As a result, the work done by centrifugal force comes out to be zero, which

further keeps the stagnation temperature same within the diffuser section. The stagnation pressure, however, lowers down due to the losses which turn out to be a significant part of the proposed model development process.

To start with, an ideal stage diffusion process in an axial stage is considered, which is further modified to obtain the general stage equation with the inclusion of stagnation pressure losses.

2.1.1 The Ideal Diffusion Process in Axial Compressor Stage

Consider a steady flow of ideal fluid passing through an axial blade passage as shown in Figure 2.1. Flow enters the passage at non-zero angle of attack or incidence angle α, with effective area being $A_i\cos(\beta_i + \alpha)$ and leaves with the effective area of $A_e\cos(\beta_e)$. Although the difference between A_i and A_e could be small, it is the difference between blade angles $(\beta_i - \beta_e)$ which is generally significant and governs the overall flow turning. The stage diffusion process can be understood by considering the conservation laws for mass and energy. The governing system is then closed by adding isentropic relation for an ideal fluid.

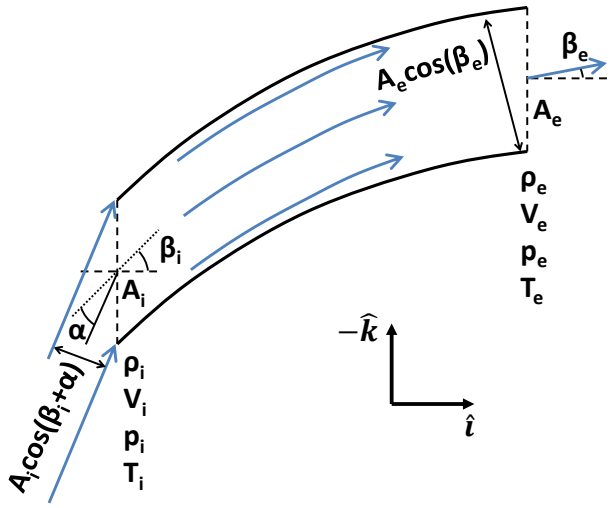

Figure 2.1: Blade passage modelled as a diffuser section with flow entering at non-zero angle of attack

Continuity

$$\rho_i V_i A_i \cos(\beta_i + \alpha) = \rho_e V_e A_e \cos(\beta_e) = \dot{m} \tag{2.1}$$

Energy

$$c_p T_i + \frac{1}{2} {V_i}^2 = c_p T_e + \frac{1}{2} {V_e}^2 \tag{2.2}$$

Isentropic Relation

$$\frac{p_i}{{\rho_i}^\gamma} = \frac{p_e}{{\rho_e}^\gamma} \tag{2.3}$$

After combining the above equations (2.1)-(2.3), following relationship can be obtained:

$$\left(\frac{p_e}{p_i}\right)^{\frac{2}{\gamma}} \left(1 + \frac{1}{{M_i}^2} \left(\frac{2}{\gamma - 1}\right) \left(1 - \left(\frac{p_e}{p_i}\right)^{\frac{\gamma-1}{\gamma}}\right)\right) = \Psi \tag{2.4}$$

where

$$\Psi = \left(\frac{A_i}{A_e}\right)^2 \frac{\cos^2(\beta_i + \alpha)}{\cos^2(\beta_e)} \tag{2.5}$$

Here, Ψ is an indicator of extent of flow diffusion taking place inside the passage and is a function of blade geometry and angle of attack. For large inlet angles $\beta_i + \alpha$, the value of Ψ is small and particularly for $\beta_i + \alpha = 90$ degrees, $\Psi = 0$. Under this condition, equation (2.4) gets reduced to

$$\frac{p_e}{p_i} = \left(1 + \left(\frac{\gamma - 1}{2}\right) {M_i}^2\right)^{\frac{\gamma}{\gamma-1}} \tag{2.6}$$

Through a careful observation of equation (2.6) for typical values of inlet Mach number, it can be witnessed that in this case the exit static pressure is essentially same as the inlet stagnation pressure, which implies complete flow diffusion. However, it can also be noticed that inlet velocity in this case is normal to the flow area which amounts to zero mass flow through the passage.

For positive angle of attack ($\alpha > 0$), the incoming area $A_i \cos(\beta_i + \alpha)$ is smaller than the flow area which would be observed just after entering the passage, i.e., $A_i \cos(\beta_i)$. This area change amounts to sudden flow turning, which being equivalent to sudden expansion

in a channel, therefore results in stagnation pressure losses. Modelling these inlet turning losses constitutes an important feature of this work. On the contrary, for negative angle of attack ($\alpha < 0$), the area of incoming stream is larger than the inlet passage area. This results in sudden flow contraction and if incoming Mach number is too high (though still subsonic), the flow could choke essentially choking the entire compressor. In this case, the sudden drop in compressor pressure, as generally observed for high mass flow rates, would be obtained. However, if the incoming flow Mach number is quite low to create a choked throat, the stage may go into a "negative stall" (i.e., stall at high negative angle of attack).

2.1.2 General Stage Equation with Losses

The ideal diffusion process does not account for stagnation pressure losses which might occur due to various mechanisms as discussed later. To model a general stage diffusion process, let us consider two points inside the passage, say 1 and 2, and represent the flow diffusion from 1 to 2 as a difference between isentropic process and stagnation pressure loss ($\Delta p_{s,loss}$) as shown below:

$$p_{s2} = p_{s2,isen} - \Delta p_{s,loss} = p_{s1}\left(\frac{T_{s2}}{T_{s1}}\right)^{\frac{\gamma}{\gamma-1}} - \Delta p_{s,loss} \tag{2.7}$$

During the diffusion process, the stagnation temperature between these two points could change due to the work done by the centrifugal force. By energy balance, this work done can be integrated to calculate the stagnation temperature at point 2 as shown below:

$$c_p T_{s2} = c_p T_{s1} + \frac{1}{2}\Omega^2\left({r_2}^2 - {r_1}^2\right) \tag{2.8}$$

For both the compressors and turbines, loss of stagnation pressure is generally quantified in terms of loss of dynamic pressure [36]. The pressure loss coefficient (ω_{loss}) representing

deviation from ideal performance is given by

$$\omega_{loss} = \frac{p_{s2,isen} - p_{s2}}{p_{s2,isen} - p_2} = \frac{\Delta p_{s,loss}}{p_{s2,isen} - p_2} \tag{2.9}$$

After the introduction of above definition for the pressure loss coefficient (ω_{loss}), the stage equation (2.7) gets recast into the following form:

$$p_{s2} = p_{s1}\left(\frac{T_{s2}}{T_{s1}}\right)^{\frac{\gamma}{\gamma-1}}(1-\omega_{loss}) + \omega_{loss}p_2 \tag{2.10}$$

To simplify this analysis, let us introduce another variable f which is purely a function of Mach number M and specific heat ratio γ, and relates the stagnation temperature to static temperature as shown below:

$$T = T_s f(M,\gamma) \tag{2.11}$$

where

$$f = \left(1 + \left(\frac{\gamma-1}{2}\right)M^2\right)^{-1} \tag{2.12}$$

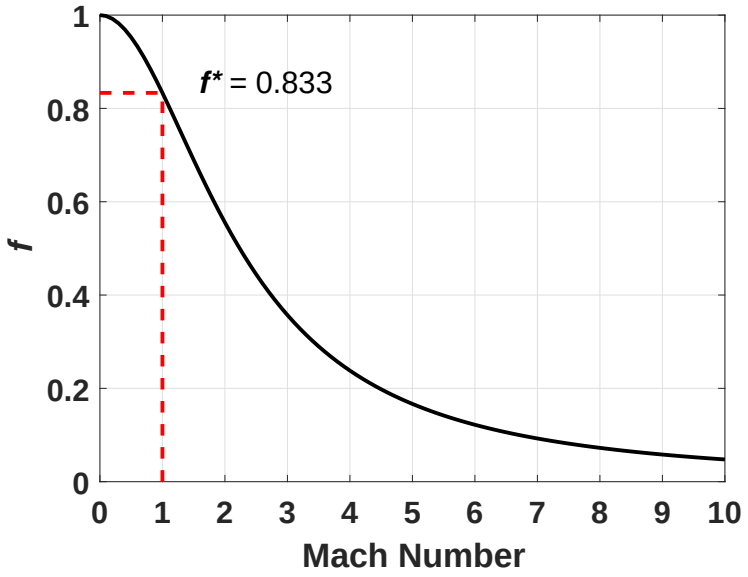

Figure 2.2: Plot of function f versus Mach number for $\gamma = 1.4$ with f^* calculated at $M = 1$

The plot of f versus mach number M for $\gamma = 1.4$ is shown in Figure 2.2, which indicates that f remains bounded between 0 and 1 even though Mach number could be unbounded. Equation (2.10) can be completely represented in terms of function f if the static pressure p, and stagnation pressure p_s are obtained in terms of f.

For steady quasi-1D analysis, the mean-line velocity is given by

$$V = \sqrt{2c_p(T_s - T)} = \sqrt{2c_p T_s}\sqrt{1 - f} \tag{2.13}$$

Imposing the mass flow rate constraint, density can be expressed using the continuity equation as

$$\rho = \frac{\dot{m}}{AV} = \frac{\dot{m}}{A}\frac{1}{\sqrt{2c_p T_s}\sqrt{1 - f}} \tag{2.14}$$

where A is the flow cross-section area. Using the perfect gas equation ($p = \rho RT$) and equations (2.11) and (2.14), the relations for static pressure and stagnation pressure can now be expressed as

$$p = \frac{\dot{m}}{A}\frac{\gamma - 1}{\gamma}\sqrt{\frac{c_p T_s}{2}}\frac{f}{\sqrt{1 - f}} \tag{2.15}$$

$$p_s = p f^{\frac{\gamma}{1-\gamma}} = \frac{\dot{m}}{A}\frac{\gamma - 1}{\gamma}\sqrt{\frac{c_p T_s}{2}}\frac{f^{\frac{1}{1-\gamma}}}{\sqrt{1 - f}} \tag{2.16}$$

where γ is the specific heat ratio. By substituting the expressions from equations (2.15) and (2.16) into equation (2.10) and making use of equation (2.8), the following single equation is obtained, which relates the value of f at station 2 (f_2) to its value at station 1 (f_1):

$$\frac{{f_2}^{\frac{1}{1-\gamma}} - \omega_{loss} f_2}{\sqrt{1 - f_2}} = G \tag{2.17}$$

where

$$G = (1 - \omega_{loss})\frac{A_2}{A_1}\left(1 + \frac{\Omega^2({r_2}^2 - {r_1}^2)}{2c_p T_{s1}}\right)^{\frac{\gamma+1}{2(\gamma-1)}}\frac{{f_1}^{\frac{1}{1-\gamma}}}{\sqrt{1 - f_1}} \tag{2.18}$$

Equation (2.17) is the general stage equation where the right hand side, i.e., G can be

completely determined for a given compressor geometry, inlet condition and an underlying loss model. This enables the calculation of f_2 which upon using relations given by equations (2.13)-(2.16) provides all the flow variables at point 2. Clearly for no losses ($\omega_{loss} = 0$) and negligible changes in mean-line radius ($r_2 = r_1$), it is the pure flow diffusion that governs the stage exit condition.

2.1.3 Estimation of General Losses

The performance of an industrial compressor, far from being ideal, can be accurately predicted by the inclusion of a novel loss model encompassing various physical mechanisms. This section considers models for different direct and indirect sources of stagnation pressure losses, and essentially gives an estimate of ω_{loss} term featured in the stage equation (2.17).

Shock and Inlet Turning Losses

As mentioned earlier, streamline entering a stage element at non-zero incidence or attack angle has to turn suddenly for following the blade passage, which essentially leads to stagnation pressure loss. It is assumed that this sudden inlet turning results in flow separation at the blade leading edge with further reattachment at some downstream distance. At positive angle of attack, the turning process is represented as flow through a channel with sudden area expansion as shown in Figure 2.3. Similarly at negative angle of attack, the area of incoming stream is larger than the passage area, which is analogous to sudden flow contraction process, also shown in the figure.

Often for a transonic compressor operating at high speeds, Mach number in blade relative frame could turn out to be more than 1.0, thus making the flow locally supersonic. In such a case, a normal shock is modelled at the passage inlet and the Mach number behind the shock is calculated using the following relationship:

$$M_1{}^2 = \frac{(\gamma - 1)M_{in}{}^2 + 2}{2\gamma M_{in}{}^2 - (\gamma - 1)} \tag{2.19}$$

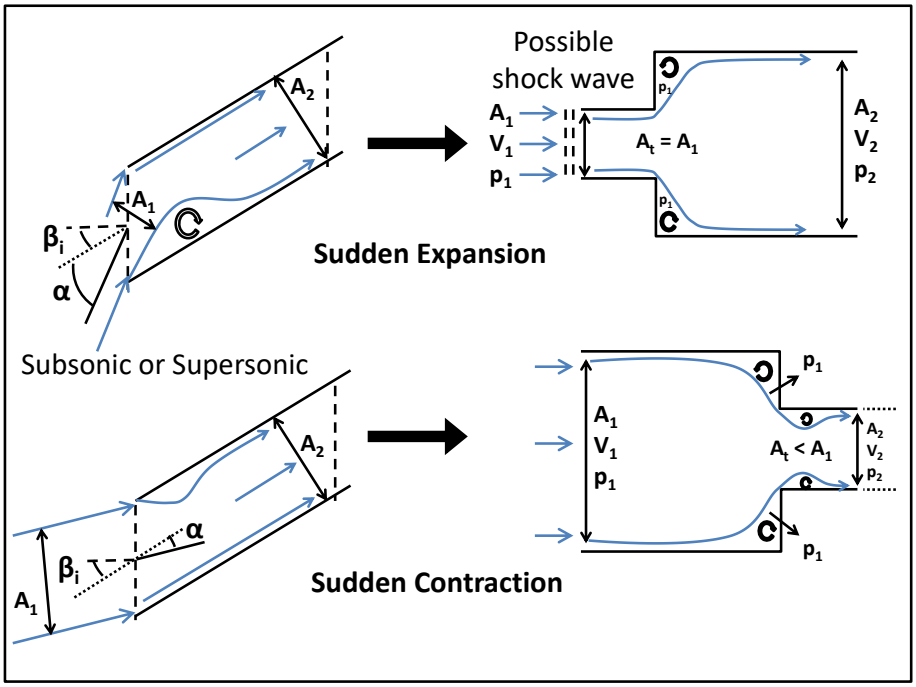

Figure 2.3: Inlet turning process where the flow entering at positive angle of attack is represented as sudden expansion, while the flow entering at negative angle of attack is shown as sudden contraction

The post-shock condition is then used as the inlet condition for the turning element. The flow contraction results in the formation of a throat which is identified as the smallest area in the turning element. For positive angle of attack ($\alpha > 0$), the throat area A_t is taken to be same as the inlet area A_1. However, at negative attack angle ($\alpha < 0$), there is a severe area reduction and the throat area is given by Weisbach formula [49] as written below:

$$\frac{A_t}{A_2} = 0.63 + 0.37 \left(\frac{A_2}{A_1} \right)^3 \tag{2.20}$$

Overall, the complete inlet turning process has been divided into two steps: a) an isentropic flow contraction between the inlet and throat with no stagnation pressure loss, b) subsequent expansion from the throat to exit resulting in loss. The mathematical equivalent of the first step can be expressed as

$$p_{st} = p_{s1} \tag{2.21}$$

which upon using equation (2.16) gets converted to

$$\frac{f_t{}^{\frac{1}{1-\gamma}}}{\sqrt{1-f_t}} = \frac{A_t}{A_1}\frac{f_1{}^{\frac{1}{1-\gamma}}}{\sqrt{1-f_1}} \tag{2.22}$$

Depending upon the inlet angle of attack, the throat area is either kept same as the incoming stream area or calculated using equation (2.20). This in turn is used to calculate the throat function f_t using equation (2.22) and subsequently throat Mach number M_t using equation (2.12). Particularly for negative angles of attack, if A_t/A_1 is too low, the throat Mach number could turn out to be supersonic (physically an impossible situation). In practice, however, the throat becomes choked imposing an upper limit on the throat Mach number, i.e., $M_t = 1$.

For expressing second step of the turning process, it is assumed that the flow separation occurring due to sudden area change maintains a constant static pressure across the throat cross-section. By taking flow to be incompressible and neglecting viscous effects, momentum balance equation between the throat and the exit can be simply written as

$$\dot{m}(V_2 - V_t) = A_2(p_t - p_2) \tag{2.23}$$

Using the expressions for velocity and static pressure in terms of function f, the above equation gets rewritten as

$$\sqrt{1-f_2} + \frac{\gamma-1}{2\gamma}\frac{f_2}{\sqrt{1-f_2}} = \sqrt{1-f_t} + \frac{A_2}{A_t}\frac{\gamma-1}{2\gamma}\frac{f_t}{\sqrt{1-f_t}} \tag{2.24}$$

The two-step inlet turning process expressed in terms of equations (2.22) and (2.24), is required to be solved by invoking Weisbach formula using areas A_1 and A_2. After solving for f_2, the pressure loss coefficient given in equation (2.9) determines the loss due to inlet turning or incidence. Using the relations for static and stagnation pressures, this can be

expressed as

$$\omega_{turn,loss} = \frac{1 - \left(\frac{f_1}{f_2}\right)^{\frac{1}{\gamma-1}} \sqrt{\frac{1-f_1}{1-f_2}} \frac{A_1}{A_2}}{1 - f_1^{\frac{\gamma}{\gamma-1}}} \tag{2.25}$$

The turning process, however, does not consider losses that could occur due to the flow separation inside a blade passage and subsequent mixing which can become quite severe as a result of flow non-uniformities. When the flow conditions are close to stall, separation initiates near the blade leading edge with no downstream flow reattachment, essentially making the second step of turning process a constant pressure expansion. Under such extreme condition, equation (2.23) becomes

$$p_2 = p_t \tag{2.26}$$

which upon using equation (2.15) results in

$$\frac{f_2}{\sqrt{1-f_2}} = \frac{A_2}{A_t} \frac{f_t}{\sqrt{1-f_t}} \tag{2.27}$$

Both inlet turning and blade passing mixing can now be expressed using a single *sliding scale equation* by introducing mixing loss factor $0 \leq \xi_{ml} \leq 1$, as a model parameter. ξ_{ml} which represents the extent of mixing, is now used to combine equations (2.24) and (2.27) as shown below:

$$\begin{aligned} (1-\xi_{ml})\sqrt{1-f_2} + \left(\frac{\gamma-1}{2\gamma}(1-\xi_{ml}) + \xi_{ml}\right) \frac{f_2}{\sqrt{1-f_2}} \\ = (1-\xi_{ml})\sqrt{1-f_t} + \frac{A_2}{A_t}\left(\frac{\gamma-1}{2\gamma}(1-\xi_{ml}) + \xi_{ml}\right) \frac{f_t}{\sqrt{1-f_t}} \end{aligned} \tag{2.28}$$

It can be observed from the above equation that $\xi_{ml} = 0$ implies no mixing losses and equation (2.24) is recovered back. On the other hand, $\xi_{ml} = 1$ results in maximum mixing losses, essentially giving back equation (2.27). For calculation purposes, the sliding scale equation can be easily converted into a quadratic equation by substituting $x = \sqrt{1-f_2}$.

Wall Friction Loss

The loss due to wall friction turns out to be significant if thick boundary layers develop over the compressor blades and end-wall casing. To account for this loss, the theory of flow inside pipes has been taken into consideration, where the pressure loss Δp gets expressed in terms of friction factor λ as shown below:

$$\frac{\Delta p}{l} = \frac{\lambda}{D_h}\frac{\rho V^2}{2} \tag{2.29}$$

where l is the length of pipe and D_h is the hydraulic diameter. The friction factor λ is related to local Reynolds number Re as shown by Schlitchting [50] for pipes of different shaped cross-sections like triangular, square, rectangular etc. Particularly for turbulent flow inside a smooth circular pipe, the friction factor can be determined by Blasius correlation [50] as given below:

$$\lambda = \frac{0.316}{Re^{1/4}} \tag{2.30}$$

For the case of low to moderate Mach numbers, the friction loss represented as stagnation pressure loss can be approximated by the loss of static pressure, i.e., $\Delta p_{s,loss} = \Delta p$. Using equation (2.29) and the definition of pressure loss coefficient, this can be mathematically expressed as

$$\omega_{f,loss} = \frac{\Delta p}{\frac{1}{2}\rho V^2} = \lambda\sigma = \frac{0.316}{Re^{1/4}}\sigma \tag{2.31}$$

where $\sigma = l/D_h$ is the representative blade solidity. For typical flow conditions inside the blade passages, Reynolds numbers are well above 10000 resulting in λ to be less than 3%.

For unsteady flows, however, local wall shear stress τ_w is required to be determined for inclusion into the flow equations. For quasi-1D analysis, this is estimated by writing a force balance between the pressure and shear forces for incompressible flow, which gives

$$\Delta p\frac{\pi {D_h}^2}{4} = \tau_w \pi D_h L \tag{2.32}$$

Substituting for Δp from equation (2.29), the wall shear stress gets expressed as

$$\tau_w = \frac{\lambda}{8}\rho V^2 \tag{2.33}$$

Comparing the above relationship with the definition of wall shear stress, it can be seen that the skin friction coefficient C_{fw} is 1/8th of the friction factor λ. Further, the above relationship represents wall shear force per unit area. For calculating the force per unit length (as generally is required for mean-line analysis), τ_w must be multiplied by local streamtube width b. In the unsteady model (as would be discussed in section 2.2), above analysis is kept as a guideline for setting C_{fw} value. However, for better model tuning a slightly modified value has been used.

Tip Leakage Loss

During cascade testing, blades arranged in linear or annular fashion are firmly attached to the hub and shroud, thus allowing no flow leakage from one blade passage to another. In an actual compressor, on the other hand, there is a small but finite clearance between the blades and casing installations through which flow can leak from the high pressure to low pressure or suction side. The bulk stagnation pressure loss model, in this case, has been approached by calculating the kinetic energy of the leakage jet that gets dissipated. Details of the underlying theoretical model for tip leakage loss are shown in Appendix A. Further, the reader can refer to the paper presented by Mishra *et al.* [51] for a primitive formulation. Using the energy dissipation approach, the pressure loss coefficient gets simplified to the below formula:

$$\omega_{tip\_leak,loss} = \frac{\lambda_{tip}(2\theta_c)^{3/2}\dfrac{1}{\sqrt{\sigma}}}{1 + \lambda_{tip}(2\theta_c)^{3/2}\dfrac{1}{\sqrt{\sigma}}} \tag{2.34}$$

where λ_{tip} is non-dimensional parameter representing the ratio of tip gap to blade height, σ is the blade solidity, and θ_c is the camber angle. Through this analysis, it can be observed

that a high solidity blade leads to lower stagnation pressure loss. Equation (2.34) is in a good agreement with the approach and corresponding measurements presented by Senoo and Ishida [52].

Trailing Edge Flow Deviation

Flow leaving the trailing edge of a blade passage generally deviates by some angle δ_{dev} from the design blade angle β_e. Although the trailing edge deviation does not impose any stagnation pressure loss directly, it changes the total blade passage diffusion by reducing the effective flow turning. In most cases, the deviation approach based upon Carter's rule [53, 54] works good. As per this rule, the deviation angle is given by

$$\delta_{dev} = m\frac{\theta_c}{\sigma^n} \tag{2.35}$$

where m is a parameter dependent on stagger angle and blade airfoil, θ_c is the camber angle, σ is the blade solidity, and n is an exponent typically close to 1.0 for small inlet flow angles, but drops to 0.5 for high inlet flow angle values. For the purpose of 1D compressor flow modelling in this study, the following expression for the trailing edge flow deviation angle (δ_{dev}) has been used:

$$\delta_{dev} = 0.2\frac{\theta_c}{\sigma} = 0.2\frac{(\beta_i - \beta_e)}{\sigma} \tag{2.36}$$

The above developed loss model is now used to predict the losses in a virtual cascade test, results of which are shown in Figure 2.4. In this prediction, the mechanism of extra mixing losses has been ignored, i.e., ξ_{ml} is set 0. This simplification is expected to underpredict losses at angles close to the stall. Since the stall may occur at relatively low negative angles of attack, one should perceive the results at negative incidence as being overly optimistic. Still, there is a significant agreement with the published results of the cascade test. The model in its basic form (i.e., $\xi_{ml} = 0$) shows that an increase in inlet Mach number from 0.4 to 0.8 has relatively mild effect on the increase of losses. This finding is well supported by

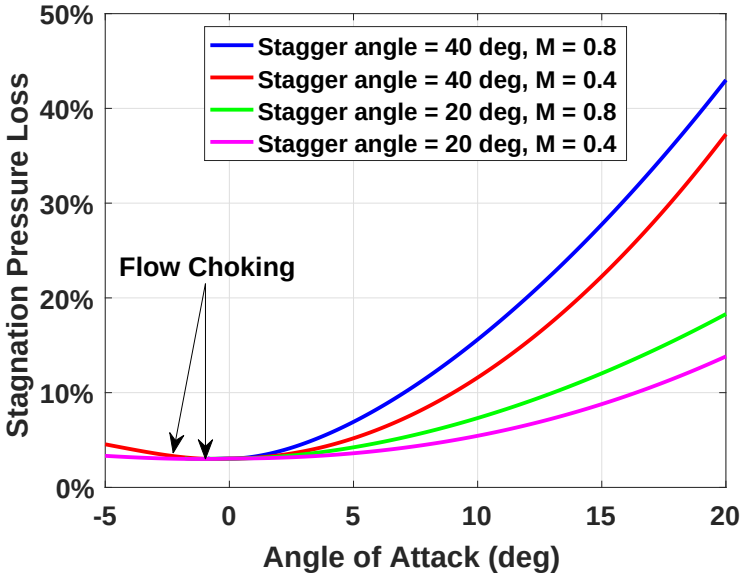

Figure 2.4: Turning losses prediction in a virtual cascade test at various inlet Mach numbers and stagger angles

the data obtained by Andrews [55]. Contrary to the mild effect of the Mach number, the stagger angle appears to have a significant effect on the losses, a sensitivity also reported by Yocum and O'Brien [56]. A seemingly subtle yet important fact is that flow choking is encountered at $M = 0.8$ when the angle of attack is only slightly negative, thus not yet close to the stall.

2.1.4 Estimation of Centrifugal Stage Specific Losses

The losses introduced in the previous section due to off-design incidence, shock formation, wall friction, etc., are quite general and has been used for calculating losses in both the axial and centrifugal compressors. Exception is the trailing edge deviation which is implemented only for the axial stages. This section deals with losses specific to the centrifugal stage. Due to the finite number of impeller blades, a slip factor has also been included.

Disk Friction, Blade Loading and Recirculation Losses

Disk friction loss is due to the viscous torque exerted by the fluid moving in the side gap or backplate onto the impeller or rotating component. In comparison to other frictional losses, this loss component could be quite significant for an impeller rotating at high tip speeds. In this research work, NASA computational model of 1970's developed at Lewis Research Center (LRC) [28] has been taken as the reference for calculating centrifugal stage specific losses. To start with, losses are first represented in the form of an enthalpy loss function and are subsequently converted into an overall stagnation pressure ratio. Since the majority of impeller losses discussed here occur inside the vaneless space or close to the impeller exit, the resulting overall pressure ratio is imposed across the vaneless space, i.e., between the impeller and diffuser. The enthalpy loss due to impeller disk friction [28] is given by

$$\Delta h_{DF} = 0.01356 \frac{\rho_e}{\dot{m} Re^{0.2}} {U_e}^3 {D_e}^2 \tag{2.37}$$

where

$$Re = \frac{\rho_{amb} U_e D_e}{\mu_{amb}} \tag{2.38}$$

is the Reynolds number calculated using impeller exit rotational velocity U_e, exit diameter D_e, and the compressor ambient conditions. The subscript e denotes the impeller exit value and $\dot{m}$ is the mass flow rate.

Blade loading loss accounts for secondary flow effects due to high tangential blade-to-blade pressure gradients and the boundary layers. According to NASA LRC model, this loss component is directly related to the impeller exit speed U_e and the diffusion factor D_f. The enthalpy loss due to blade loading [28] is given by

$$\Delta h_{BL} = 0.05 {D_f}^2 {U_e}^2 \tag{2.39}$$

where D_f is the diffusion factor,

$$D_f = 1 - \frac{W_e}{W_{i,tip}} + \frac{K_{BL} q_{aero}}{\frac{W_{i,tip}}{U_e}\left[\frac{N_I}{\pi}\left(1 - \frac{D_{i,tip}}{D_e}\right) + 2\frac{D_{i,tip}}{D_e}\right]} \tag{2.40}$$

In the above expression, the subscript i, tip denotes the tip value at impeller inlet, N_I is the number of impeller blades and K_{BL} has a value 0.75 for conventional impellers and 0.60 for impeller with splitter blades. The dimensionless head q_{aero} is the ratio of total enthalpy rise across the impeller and exit speed squared as shown below:

$$q_{aero} = \frac{\Delta h_s}{{U_e}^2} \tag{2.41}$$

which comes out to be unity from classical energy conservation approach across the impeller.

Recirculation loss occurs when the fluid inside the vaneless space gets recirculated back into the impeller leading to extra work input and impeller efficiency reduction. The enthalpy loss due to recirculation, as shown below, is a function of impeller exit absolute flow angle α_e, diffusion factor D_f and exit rotational speed U_e as shown below:

$$\Delta h_{RC} = 0.02\sqrt{\tan(\alpha_e)}{D_f}^2{U_e}^2 \tag{2.42}$$

The loss mechanisms, as discussed above, are incorporated as an equivalent stagnation pressure ratio across the vaneless space. Converting the sum of enthalpy loss functions into an equivalent pressure ratio results in

$$\frac{p_{s2}}{p_{s1}} = \left(1 - \frac{\Delta h_{DF} + \Delta h_{BL} + \Delta h_{RC}}{c_p T_{se}}\right)^{\frac{\gamma}{\gamma - 1}} \tag{2.43}$$

where T_{se} is impeller exit stagnation temperature. Now according to the pressure loss coefficient (equation (2.9)), this gets converted to

$$\omega_{imp,loss} = \frac{1 - p_{s2}/p_{s1}}{1 - p_1/p_{s1}} \tag{2.44}$$

Upon knowing the impeller exit conditions, the above impeller losses are implemented in the centrifugal stage model to calculate the diffuser entry conditions.

Losses in Vaned Diffuser

Vaned diffusers are generally advantageous over vaneless ones as they achieve the required diffusion or pressure rise over smaller effective length. The flow discharging from the impeller has high velocity, which upon entering the diffuser could lead to supersonic flow and thus to shock formation. The shock loss and the incidence loss, as discussed in the previous section 2.1.3, are incorporated in compact form at the diffuser entry. Subsequently, the wall friction and tip leakage losses are also implemented.

Few studies like [57] have shown that the diffusers with large expansion angle could lead to flow separation inside the passage. To quantify the loss due to separation, let us consider the separation process inside two different passages as shown in Figure 2.5. In the case of diffusion with gradual area increase, flow separates as the boundary layers can no

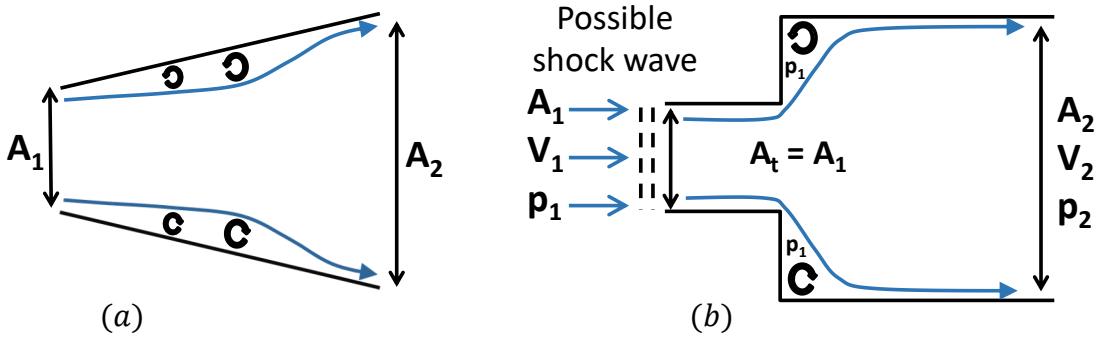

Figure 2.5: Separation process inside a two-dimensional (a) diffuser, (b) backward facing step

longer remain attached in the adverse pressure gradient environment. In the vaned diffusers, this gradual separation can be observed experimentally, however difficulties in quantifying such process renders the modelling efforts fruitless. In the present model, separation in backward facing step, as shown on the right side, is taken as the reference for quantifying the diffuser separation loss. To approach this problem, the sudden expansion process as shown systemically in Figure 2.3 has been considered. Upon balancing momentum between the throat and exit of the step, equation (2.24) gets recovered, which after transforming into a quadratic equation can be written as

$$ax^2 + bx + c = 0 \tag{2.45}$$

where $x = \sqrt{1 - f_2}$ and the coefficients a, b and c are given by

$$\begin{aligned} a &= \gamma + 1 \\ b &= -2\gamma\sqrt{1 - f_t} - \frac{A_2}{A_t}(\gamma - 1)\frac{f_t}{\sqrt{1 - f_t}} \\ c &= \gamma - 1 \end{aligned}$$

The loss in the sudden expansion step, by definition, is given by an expression similar to the equation (2.44) as

$$\omega_{step,loss} = \frac{1 - p_{s2}/p_{st}}{1 - p_t/p_{st}} \tag{2.46}$$

which upon using equations (2.15) and (2.16) gives

$$\omega_{step,loss} = \frac{1 - \left(\frac{f_t}{f_2}\right)^{\frac{1}{\gamma-1}} \sqrt{\frac{1 - f_t}{1 - f_2}} \frac{A_t}{A_2}}{1 - f_t^{\frac{\gamma}{\gamma-1}}} \tag{2.47}$$

It should be noted that $\omega_{step,loss}$ can be obtained for a range of subsonic and supersonic flows in the inlet. Once the step loss $\omega_{step,loss}$ is calculated, the inline separation loss is estimated

using a separation degree factor $0 \leq D_{sp} \leq 1$, assigned to the diffuser. The separation degree factor D_{sp}, is a function of diffuser geometry and shaft speed.

$$\omega_{sp,loss} = D_{sp} \cdot \omega_{step,loss} \tag{2.48}$$

To obtain the D_{sp} value, a comprehensive diffuser data analysis is required that can provide a correlation measure. However, from the measured data of the very compact diffuser of HECC [27], mentioned in Chapter 1, a value between 0.3 to 0.4 seems to provide a good agreement as long as the diffuser is not close to the choke. After a certain high throat Mach number, D_{sp} increases gradually and reaches a value of 1.0 as the diffuser chokes.

Slip Factor Formulation

Flow leaving the impeller blades hardly follows the design blade exit angle and deviates by some degree. This is known as fluid slip and is quantified in terms of a slip factor σ. One of the possible reasons for this is the existence of tangential pressure gradient in response to the Coriolis force near the blade outlet. High pressure at the leading blade face and low pressure at the trailing blade face result in nonuniform velocity distribution at any radial location. Particularly at the impeller exit, the tangential velocity becomes high enough so that the flow leaves at angle β_e' deviating from the original blade angle β_e.

Slip factor depends upon a number of parameters, namely number of impeller blades, amount of boundary layer blockage, extent of flow separation, blade geometry, etc. Wiesner [25] presented a review of various methods that can be used for the estimation of slip factor. One of the popular expressions proposed by Stanitz [58] is given by

$$\sigma = 1 - \frac{1.98}{N_I(1 - \phi_e \cot(\beta_e))} \tag{2.49}$$

where N_I is the number of impeller blades, ϕ_e is the exit flow coefficient, and β_e is the blade exit angle. For high exit blade angle ($\beta_e > 45$ deg.), as typically is the case for the

compressors studied in this work, equation (2.49) is approximated as

$$\sigma = 1 - \frac{1.98}{N_I} \tag{2.50}$$

2.1.5 Vaneless Space and Interstage Gap Model

The use of a zone between the impeller and vaned diffuser in which the flow can expand without vanes to subsonic speed is very common [44]. Flow leaving the impeller enters the vaneless space at an absolute angle α_1 and leaves at an angle α_2, as shown in Figure 2.6. For one-dimensional analysis, the vaneless space model is approached by conserving mass, energy and angular momentum across the two radii, i.e., r_1 and r_2.

Upon conserving mass flow rate between r_1 and r_2, and making using of equation (2.16) lead to

$$\frac{p_{s2}}{p_{s1}} \frac{1}{A_1 \cos(\alpha_1)} \frac{f_1^{\frac{1}{1-\gamma}}}{\sqrt{1-f_1}} = \frac{1}{A_2 \cos(\alpha_2)} \frac{f_2^{\frac{1}{1-\gamma}}}{\sqrt{1-f_2}} \tag{2.51}$$

where A_1 and A_2 are radial cross-section areas depending upon local radius and streamtube width b. The conservation of energy is essentially embedded in the above equation, which makes the stagnation temperature same at the two radial locations. It should be further observed that the vaneless space is not required to be isentropic and could have significant stagnation pressure loss. Moreover, in this work, the impeller losses represented in terms

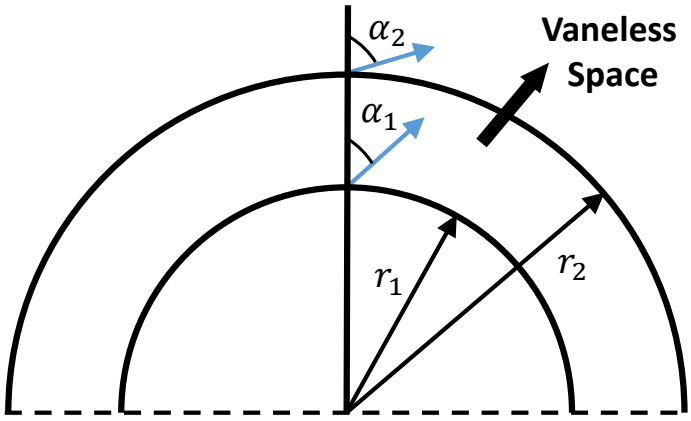

Figure 2.6: Flow direction at the inlet and exit of vaneless space

of overall stagnation pressure ratio (see equation (2.43)) are implemented in compact form across the vaneless space.

Let us now relate the area ratio (A_2/A_1) to radius ratio (r_2/r_1) using a function $g(r_2/r_1)$ as shown below:

$$\frac{A_2}{A_1} = g\left(\frac{r_2}{r_1}\right)\frac{r_2}{r_1} \tag{2.52}$$

In a more specific case where the width of streamtube is constant throughout the vaneless space, the function $g(r_2/r_1)$ is just unity. Conservation of angular momentum dictates

$$r_1 V_1 \sin(\alpha_1) = r_2 V_2 \sin(\alpha_2) \tag{2.53}$$

and further using f formulation for velocity, i.e., equation (2.13) results in

$$r_1 \sin(\alpha_1)\sqrt{1-f_1} = r_2 \sin(\alpha_2)\sqrt{1-f_2} \tag{2.54}$$

Now combining equations (2.51), (2.52) and (2.54) gives

$$\frac{\tan(\alpha_2)}{\tan(\alpha_1)} = g\left(\frac{r_2}{r_1}\right)\left(\frac{f_2}{f_1}\right)^{\frac{1}{\gamma-1}}\frac{p_{s2}}{p_{s1}} \tag{2.55}$$

Equations (2.54) and (2.55) represent a system of two equations with two unknowns, i.e., α_2 and f_2 which can be obtained in an iterative manner. Since f is bounded between 0 and 1, first a value for $f_2 > f_1$ is guessed and then α_2 is calculated using equation (2.55). Next, it is checked whether the values of f_2 and α_2 satisfy equation (2.54), else the guess for f_2 is updated. The process is repeated until the iterations converge. Finally upon using the relations given by equations (2.13)-(2.16), all other flow quantities at the exit of vaneless space are obtained.

In a similar fashion, interstage gaps dictated by a stagnation pressure ratio p_{s2}/p_{s1} can be treated. In this case, the width of streamtube generally changes across the gap, hence the function $g(r_2/r_1)$ turns out to be slightly important.

2.1.6 Inclusion of Compressor Bleed Ports

Air is bled from the compressor mainly for cooling turbine blades and improving the stability margin. To incorporate the bleed ports in the steady state analysis, let us consider that the air is bled at a constant mass flow rate $\dot{m}_b$, as shown in Figure 2.7. In turn, this changes the downstream flow condition which is required to be evaluated. In case of bleed air stagnation enthalpy h_{sb} being same as the upstream value h_{s1}, it can be shown by conservation of energy that the downstream stagnation enthalpy does not change, i.e., $h_{s2} = h_{s1}$. Further the mass conservation implies

$$\dot{m}_2 = \dot{m}_1 - \dot{m}_b \tag{2.56}$$

An important thing to consider while incorporating bleed ports is to minimize the losses. Considering no loss of stagnation pressure due to the bleed port, the downstream stagnation pressure p_{s2} remains same as the upstream stagnation pressure p_{s1}. Upon using equation (2.16) and taking negligible change in the flow stream cross-section area A, the following equation is obtained:

$$\dot{m}_2 \frac{f_2^{\frac{1}{1-\gamma}}}{\sqrt{1-f_2}} = \dot{m}_1 \frac{f_1^{\frac{1}{1-\gamma}}}{\sqrt{1-f_1}} \tag{2.57}$$

With known upstream state and using equation (2.56), the above equation can be solved for f_2. Since h_{s2} and p_{s2} are already known, other required flow variables are obtained using relations given in equations (2.13)-(2.16).

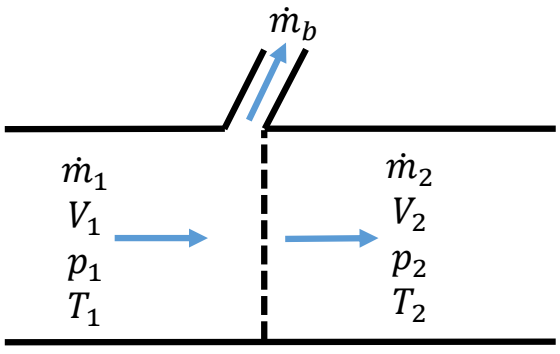

Figure 2.7: Compressor bleed port with incoming and outgoing flow streams

2.1.7 Flow Separation and Stall Considerations

Stall is traditionally associated with severe flow separation. The flow could separate inside a blade passage if the inlet angle of attack or incidence angle is large. A common notion is that a stage stalls when the static pressure rise over the stage reverses its slope with respect to the flow coefficient. The question, however, is what shall be the effect of such a stall on an individual stage and on the compressor as a whole. In many cases, compressor stall refers to the point where the compressor as a whole loses stability and plunges into surge. However, surge is a dynamic response of the entire machine and is not representative of the stall of an individual stage. In fact, the compressor may be able to operate stably with one or more stalled stages, or otherwise may get into surge with most of its stages operating without a stall. In general, as shown in Figure 2.8, flow separates close to the blade trailing edge leading to small mixing losses. However, when the incidence angle in combination with other loading parameters crosses the critical/stall value, the boundary layer could separate right at the leading edge, thus inducing high losses.

In this model, two different of kinds of stall have been considered: (a) the progressive or gradual stall where the pressure rise characteristic of the compressor gradually changes its slope, (b) the abrupt or sudden stall where the compressor characteristic drops suddenly and attains larger slope than the throttle characteristic. The mixing loss factor ξ_{ml} in case of gradual stall changes smoothly, hence leads to continuous loss progression. However, as

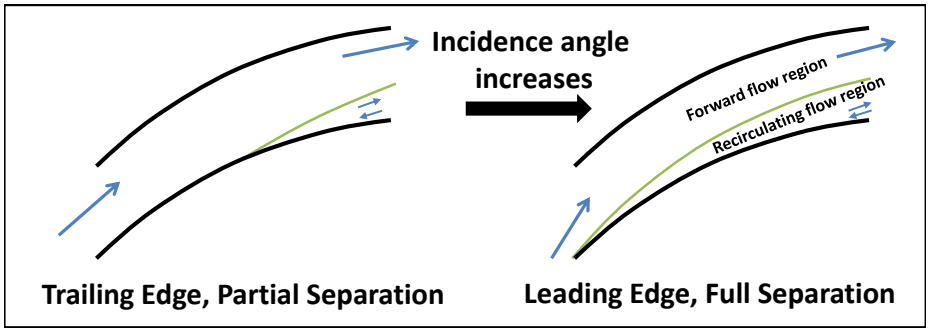

Figure 2.8: Trailing edge separation which gets converted to leading edge separation as the incidence angle increases

the separation occurs at the leading edge, a sudden jump in losses leads to sharp dynamic transition pushing the compressor into violent stall. In this case, ξ_{ml} reaches its maximum value of 1.0.

2.2 Unsteady Streamtube Analysis

The steady analysis including general stage diffusion model can be used for predicting the performance of a compressor operating without any transients. In this section, an unsteady model based upon streamtube analysis including centrifugal work and force terms in the flow governing equations is considered. The mean streamline within the streamtube is a smooth curve in three-dimensional space, whose rotation around the shaft axis results in a surface of revolution. The flow conservation equations are formulated by following this mean streamline and the surrounding streamtube.

2.2.1 Mean-line Construction

Consider mean-line m (m-line) which is the trajectory of bulk flow through the streamtube element defined by the passage between two blades. In general case, the mean-line lies on the surface of revolution as shown in Figure 2.9. An element dm is associated with a nominal cross-section area A, which represents the area of the surrounding streamtube and a characteristic width b, which represents the shape factor of this surrounding streamtube. The orientation of the m-line is defined by the stagger angle β and radial angle η with respect to the axial direction. The equation of the m-line can be derived by considering basic frame of reference to be the rotation axis x and radial coordinate y with corresponding unit vectors $\vec{i}$ and $\vec{j}$, respectively. The z-direction with corresponding unit vector $\vec{k}$, according to right hand rule, points outwards perpendicular to the xy plane. Next, consider a plane containing the point of m-line whose unit vectors $\vec{i'}$ and $\vec{j'}$ are on plane xy, but are rotated by angle η in the counter-clockwise direction. The third unit vector $\vec{k'}$ always points out of this xy plane, hence when $\eta = 0$, $\vec{i'} = \vec{i}$, $\vec{j'} = \vec{j}$ and $\vec{k'} = \vec{k}$. Now, let us consider the unit vector $\vec{m}$, which

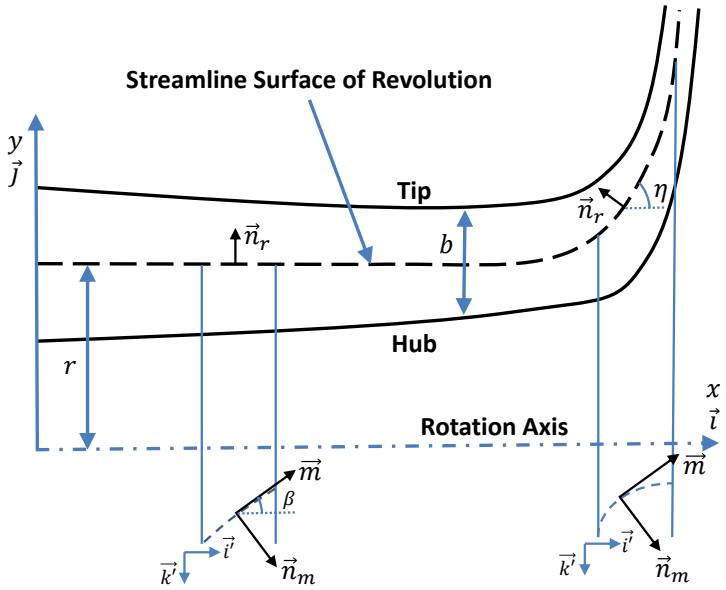

Figure 2.9: Geometrical and vector notation of generic streamtube with mean streamline

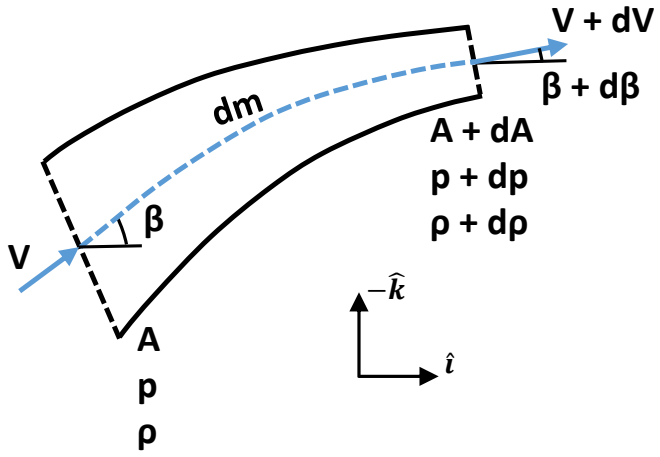

Figure 2.10: Schematic of curved streamtube with the mean-line in xz plane

is tangent to the line m at the corresponding point and lies on the plane $\vec{i'}\vec{k'}$ as shown in Figure 2.10. This vector overlaid on the trace of m is shown at the bottom of Figure 2.9 at two places, one representing mostly the axial flow and other transitioning to the radial flow. From Figure 2.9, $\vec{m}$ can be represented in terms $\vec{i'}$ and $\vec{k'}$ as

$$\vec{m} = \cos(\beta) \cdot \vec{i'} - \sin(\beta) \cdot \vec{k'} \tag{2.58}$$

Since the flow cannot cross the bounding surface and vector $\vec{j'}$ is normal to $\vec{m}$, the third vector $\vec{n}_m$ in the streamline system can be calculated as

$$\vec{n}_m = \vec{m} \times \vec{j'} = \sin(\beta) \cdot \vec{i'} + \cos(\beta) \cdot \vec{k'} \tag{2.59}$$

Further, the unit vectors $\vec{i'}$, $\vec{j'}$ and $\vec{k'}$ are just the rotational transformations of Cartesian unit vectors. This gives

$$\begin{aligned} \vec{i'} &= \cos(\eta) \cdot \vec{i} + \sin(\eta) \cdot \vec{j} \\ \vec{j'} &= -\sin(\eta) \cdot \vec{i} + \cos(\eta) \cdot \vec{j} \\ \vec{k'} &= \vec{k} \end{aligned} \tag{2.60}$$

Substituting equation (2.60) into equations (2.58) and (2.59) results in

$$\begin{aligned} \vec{m} &= \cos(\beta)\cos(\eta) \cdot \vec{i} + \cos(\beta)\sin(\eta) \cdot \vec{j} - \sin(\beta) \cdot \vec{k} \\ \vec{n}_m &= \sin(\beta)\cos(\eta) \cdot \vec{i} + \sin(\beta)\sin(\eta) \cdot \vec{j} + \cos(\beta) \cdot \vec{k} \end{aligned} \tag{2.61}$$

It can be verified that the magnitude of each unit vectors $\vec{m}$ and $\vec{n}_m$ is unity.

$$\begin{aligned} |\vec{m}| &= \sqrt{\cos^2(\beta)\cos^2(\eta) + \cos^2(\beta)\sin^2(\eta) + \sin^2(\beta)} = 1 \\ |\vec{n}_m| &= \sqrt{\sin^2(\beta)\cos^2(\eta) + \sin^2(\beta)\sin^2(\eta) + \cos^2(\beta)} = 1 \end{aligned} \tag{2.62}$$

Scaling the mean-line unit vector $\vec{m}$ and making it dm in magnitude leads to

$$d\vec{m} = \cos(\beta)\cos(\eta)dm \cdot \vec{i} + \cos(\beta)\sin(\eta)dm \cdot \vec{j} - \sin(\beta)dm \cdot \vec{k} \tag{2.63}$$

On the other hand, the mean-line differential vector can also be represented in terms of Cartesian variables as

$$\vec{dm} = dx \cdot \vec{i} + dy \cdot \vec{j} - dz \cdot \vec{k} \tag{2.64}$$

Comparing equations (2.63) and (2.64) and noting that $dy = dr$ finally give

$$\begin{aligned} dm &= \frac{dx}{\cos(\beta)\cos(\eta)} \\ dm &= \frac{dr}{\cos(\beta)\sin(\eta)} \end{aligned} \tag{2.65}$$

It is to be noted that in the axial stages where the inclination angle η is small, all the geometrical parameters are represented in terms of x, namely $r(x)$, $\eta(x)$ and $\beta(x)$. For obtaining mean-line in this case, the upper formula in equation (2.65) is used. In the radial stage, however, η approaches 90 degrees and hence x is replaced by r as the independent variable such that the geometrical functions become $x(r)$, $\eta(r)$ and $\beta(r)$ and the bottom formula is used. After numerically integrating equation (2.65), the desired mean-line functions $r(m)$, $\eta(m)$ and $\beta(m)$ and the corresponding mean-line area $A(m)$ are obtained. As shown in the next section, these mean-line quantities are used for formulating the mean-line flow equations.

2.2.2 Flow Governing Equations

In some streamtube sections, the m-line is attached to a stationary row (inlet duct, IGV, stator, diffuser section) and in other sections, it is in a non-inertial rotating frame attached to the rotor. The accelerating rotating frame introduces inertial forces, namely the centrifugal force and the Coriolis force. The centrifugal acceleration is always in the direction of the unit vector $\vec{j}$ and its magnitude is $\Omega^2 r$. The components of centrifugal acceleration along

and normal to m coordinate are given by

$$F_{centrif,m} = \Omega^2 r\vec{j} \cdot \vec{m} = \Omega^2 r\cos(\beta)\sin(\eta)$$
$$F_{centrif,n} = \Omega^2 r\vec{j} \cdot \vec{n}_m = \Omega^2 r\sin(\beta)\sin(\eta) \tag{2.66}$$

The Coriolis force per unit mass is given by

$$\vec{F}_{Cor} = 2\vec{\Omega} \times \vec{V} = 2\Omega V(\vec{i} \times \vec{m}) = 2\Omega V(\sin(\beta)\vec{j} + \cos(\beta)\sin(\eta)\vec{k}) \tag{2.67}$$

where V is the mean-line velocity amplitude. The cross product implies that the resultant force is perpendicular to both $\vec{\Omega}$ and $\vec{V}$. Since $\vec{V}$ is oriented along m, the Coriolis acceleration has no component along the m-line. The component along $\vec{n}_m$ is

$$F_{Cor,n} = 2\Omega V\sin(\eta) \tag{2.68}$$

It can be seen from above that the effect of Coriolis force is null when $\eta = 0$ and is maximum in pure radial flow, i.e., $\eta = 90$ degrees.

Now considering the mean-line differential element as shown in Figure 2.10, the conservation laws including centrifugal force and work terms can be expressed as

Continuity

$$\frac{\partial}{\partial t}(\rho A) + \frac{\partial}{\partial m}(\rho V A) = 0 \tag{2.69}$$

Energy

$$\frac{\partial}{\partial t}(\rho e_s A) + \frac{\partial}{\partial m}(\rho V h_s A) = \rho V A\Omega^2 r\cos(\beta)\sin(\eta) - C_q \tag{2.70}$$

Momentum along the mean-line

$$\frac{\partial}{\partial t}(\rho V A) + \frac{\partial}{\partial m}(\rho V^2 A) = -A\frac{\partial p}{\partial m} + \rho A\Omega^2 r\cos(\beta)\sin(\eta) - C_f \rho V^2 b \tag{2.71}$$

where C_q represents the heat loss due to cooling and is taken to be zero, C_f is the friction coefficient representing wall friction, Ω is the shaft angular speed, η is the inclination of mean-line, e_s and h_s are total energy and total enthalpy, respectively, and are defined as

$$\begin{aligned} e_s &= \frac{p}{\rho(\gamma-1)} + \frac{1}{2}V^2 \\ h_s &= h + \frac{1}{2}V^2 \end{aligned} \tag{2.72}$$

In addition to the above equations, the perfect gas law is used to relate the thermodynamic variables

$$p = \rho RT \tag{2.73}$$

Equations (2.69)-(2.73) represent any configuration that can be encountered in a compressor including pure axial, pure centrifugal, or mixed flow. Considering now the energy equation without any time-derivatives and assuming no heat losses, the energy equation gets reduced to the following form:

$$\frac{\partial}{\partial m}(\rho V h_s A) = \rho V A \Omega^2 r \cos(\beta)\sin(\eta) \tag{2.74}$$

This equation shows that for an adiabatic, pure axial stage where $\eta = 0$ degrees (i.e., radius of the mean-line is constant), the total enthalpy is constant along the stage implying

$$\rho V h_s A = \text{constant} \tag{2.75}$$

On the other hand, in a radial impeller where $\eta = 90$ degrees, there is a total enthalpy increase as a result of the work done by the centrifugal force. Also as pointed out earlier, whenever there is a change in the reference frame from stationary to rotating and vice-versa, a source of lateral velocity is applied, which raises the stagnation temperature and stagnation pressure.

2.3 Summary of Streamtube Fluid Dynamic Model

In this chapter, a quasi-1D fluid dynamic model for predicting the steady and unsteady performance of a multistage axial-centrifugal compressor has been developed. Few key features of the model are summarized below:

- Instead of approaching compressor from the aerodynamic point of view, a successive diffusers based philosophy has been adopted, which makes the analysis independent of any external force/work function.

- Differentiating a real stage from an ideal one, models for various mechanisms of losses have further been developed, which can predict the general stage performance through the evaluation of ω_{loss} term.

- By performing stage-by-stage mean-line calculation with transformations at the rotor-stator interfaces, the model is expected to estimate the operating curves for multistage transonic compressors including both the axial and centrifugal stages at various speeds.

- The unsteady streamtube model based upon conservation principles results in a system of partial differential equations. Clearly, these equations are applicable within a diffuser passage, however there is a need of boundary interface that can establish the communication between two streamtube segments in a dynamic manner. This is a crucial part of this work and is dealt systematically in the next chapter.

CHAPTER 3

NUMERICAL METHOD AND DYNAMIC COMPACT INTERFACES

The equations (2.69)-(2.73) are model partial differential equations (PDEs) and govern the flow dynamics within the passages of rotors and stators. Since, an analytical solution of the governing equations is not possible, these equations are required to be solved numerically. Further, between the sections, an interface is required to accommodate frame transformation that manifests itself as a source of normal velocity addition. In addition, within the interface, "sharp" flow changes such as passage through shock waves, sudden flow turning and intense mixing need to be also accommodated. The theory and implementation of this interface form a novel part of this work. This chapter focuses on introducing a central-difference based numerical scheme and a dynamic interface, referred to as Compact Interface Element (CIE) herein, which can be seamlessly integrated within the central scheme.

3.1 Numerical Scheme

While solving the Euler equations using numerical methods, it is common to employ some kind of interpolation like linear or higher-order within the cell, which thus leads to the so-called Riemann problem at the cell interface. Exact Riemann solvers that follow the eigenvalues or characteristic velocities of the flow equations and the corresponding eigenvectors are, by nature, very suitable for the solution of these equations cast in the conservative form. However, due to the inherent complexities of the iterative procedure required for finding the eigenvectors, approximate Riemann solvers like Roe, HLL solver, etc., became more popular. Roe solver [59] is very robust and has high resolution near the shocks and other discontinuities. However, in a general case with source terms, decomposing conservation equations into eigenvalues and the respective eigenvectors might be a time-consuming task. In a paper by Mohanraj *et al.* [60], modifications to the Roe scheme for

inclusion of source terms were established. Still, finding the eigenvectors of the linearized Jacobian matrix involves significant computational efforts. In contrast, Riemann-solver-free central schemes, which rely on flux calculations directly in terms of physical fluxes, are straight forward and thus are computationally alluring. However, the original stable central scheme introduced by Lax [61] was of low resolution. Significant modifications by Kurganov and Tadmor [62] enabled high resolution while keeping the advantages of simplicity and computation efficiency of the central scheme. The so-called KT scheme can be used in both fully-discrete form (converting PDEs directly into algebraic equations) and semi-discrete form (converting PDEs first into ODEs). The semi-discrete formulation has been followed and the resulting system of ODEs is then solved in time using modified Euler's method.

The model PDEs after slight modifications can be rewritten as a general one-dimensional conservation law as shown below:

$$\frac{\partial U}{\partial t} + \frac{\partial F(U)}{\partial m} = Q(U) \tag{3.1}$$

where

$$U = \begin{bmatrix} \rho A \\ \rho V A \\ \rho e_s A \end{bmatrix} \quad F = \begin{bmatrix} \rho V A \\ \rho V^2 A + pA \\ \rho V h_s A \end{bmatrix} \quad Q = \begin{bmatrix} 0 \\ p\dfrac{\partial A}{\partial m} + \rho A \Omega^2 r \cos(\beta)\sin(\eta) - C_f \rho V^2 b \\ \rho V A \Omega^2 r \cos(\beta)\sin(\eta) - C_q \end{bmatrix}$$

The semi-discrete form of the conservation law using central differencing at the j^{th} location can be expressed as

$$\frac{\partial U_j}{\partial t} = -\frac{H_{j+1/2} - H_{j-1/2}}{\Delta m_{j,c}} + Q(U_j) \tag{3.2}$$

with the spatial grid size calculated using central differences as

$$\Delta m_{j,c} = \frac{m_{j+1} - m_{j-1}}{2} \tag{3.3}$$

In the KT scheme, numerical flux H is written in terms of physical flux F after reconstructing the conserved variable inside a cell centered at j^{th} location. The flux $H_{j+1/2}$ at the interface between j^{th} and $(j+1)^{th}$ cells can be expressed as

$$H_{j+1/2} = \frac{1}{2}(F(U^+_{j+1/2}) + F(U^-_{j+1/2})) - \frac{a_{j+1/2}}{2}(U^+_{j+1/2} - U^-_{j+1/2}) \tag{3.4}$$

where $U^+_{j+1/2}$ and $U^-_{j+1/2}$ are linearly reconstructed variables at $j+1/2$ location corresponding to the j^{th} and $(j+1)^{th}$ cells respectively and are given by

$$\begin{aligned} U^+_{j+1/2} &= U_{j+1} - S_{j+1}\frac{\Delta m_{j+1,c}}{2} \\ U^-_{j+1/2} &= U_j + S_j\frac{\Delta m_{j,c}}{2} \end{aligned} \tag{3.5}$$

The second term on the right side of equation (3.4) is the numerical dissipation component and is essentially zero when there is no discontinuity across the interface. $a_{j+1/2}$ is the maximum local wave speed and is mathematically represented as

$$a_{j+1/2} = \max(|V^+_{j+1/2}+c^+_{j+1/2}|, |V^+_{j+1/2}-c^+_{j+1/2}|, |V^-_{j+1/2}+c^-_{j+1/2}|, |V^-_{j+1/2}-c^-_{j+1/2}|) \tag{3.6}$$

where V is the mean-line velocity and c is the local speed of sound. Following the above steps, $H_{j-1/2}$ can be similarly expressed in terms of $U^+_{j-1/2}$ and $U^-_{j-1/2}$. In the equation (3.5), the derivatives S_{j+1} and S_j are determined with minmod limiter of Van Leer's one parameter family:

$$\begin{aligned} S_j = \text{minmod}\left(\theta\frac{U_j - U_{j-1}}{m_j - m_{j-1}}, \frac{U_{j+1} - U_{j-1}}{m_{j+1} - m_{j-1}}, \theta\frac{U_{j+1} - U_j}{m_{j+1} - m_j}\right) \\ \text{where} \qquad \theta \in [1, 2] \end{aligned} \tag{3.7}$$

The minmod operator returns the term with minimum magnitude along with its sign if all terms have the same sign and returns zero otherwise. θ is the dissipation parameter and

can be varied from 1 to 2 to reduce the dissipation of numerical scheme. When $\theta = 1$, and assuming that all terms have the same sign, the minmod operator chooses the least amplitude derivative resulting in dampening of the spurious oscillations, but enhancing numerical diffusion. With larger values of θ, the minmod operator delivers a derivative larger in magnitude than the minimum but always lesser in magnitude than that based upon the central difference. This lessens the numerical damping, bounded by the least diffusive central difference term.

After explicit calculation of the flux and source terms at each time-step, the semi-discrete form, i.e., equation (3.2) is integrated using modified Euler's method. Let us denote the right hand side of equation (3.2) as $J(U_j^n)$ calculated at j^{th} spatial location and n^{th} time step. The modified Euler's method involves predictor-corrector steps similar to the first order Euler's method, where the conservative variable U_j at $t_n + \Delta t$ is calculated by averaging its value at the end of the two steps as shown below:

$$
\begin{aligned}
U_j^* &= U_j^n + \Delta t \cdot J(U_j^n) \\
U_j^{**} &= U_j^* + \Delta t \cdot J(U_j^*) \\
U_j^{n+1} &= \frac{U_j^n + U_j^{**}}{2}
\end{aligned}
\tag{3.8}
$$

Above integration strategy being second-order accurate in time makes the overall numerical scheme second-order accurate both in space and time. This central-difference based numerical scheme is implemented only at the internal nodes which are not on the rotor-stator interfaces or the external boundaries with the ambient. Furthermore, as can be seen from above, for updating an internal node in time, information at two upstream and two downstream nodes is required. Consequently, the above scheme needs to be replaced by a different scheme (or modified thereof) near the interfaces and boundaries. This issue has been addressed after the discussion of compact interfaces that follows herein.

3.2 Compact Interface as a Boundary Element

The communication between two neighboring streamtubes belonging to different elements, say rotor 1 and stator 1, does require not only change of frame, but also the inclusion of inlet turning and mixing losses in a dynamic manner. In addition to this, the flow processes that take place in the vaneless space are also required to be included inside the compact interface. Further complexity is due to the fact that rather than dealing with a boundary between the computational domain and the ambient, a boundary between two computational domains needs to be considered [63]. Proper application of boundary conditions is always a challenging issue and has not been fully resolved. Particularly, the general approach that each boundary treatment is unique in nature and needs to be tailored to the internal scheme is reflected in the paper by Griffin and Anderson [64]. Another interesting work by Poinsot and Lele [65] approached the subject of boundary conditions in a more fundamental way and established that the framework of characteristics is the most general way to approach this subject. Still in their work, they were looking for explicit algebraic connections between the characteristics to provide the required relationships. To meet the challenges associated with the development of a dynamic interface, a general approach has been followed, which should be able to work in any possible scenario, while being entirely independent of the numerical scheme that is used in the internal domain. Details of the developed theoretical framework are shown in the Appendix B, but a brief implementation procedure is described in this section.

Consider a regular grid point N which marks the interface between a rotating and a stationary element, and subsequently bifurcate this point into two nodes: an upstream node and a downstream node as shown in Figure 3.1. These two node points shown as N_U and N_D in the figure, thus constitutes an internal domain or Compact Interface Element (CIE). In a discretized geometry, CIE becomes a control volume satisfying the conservation laws. Upon using the characteristics-based approach as described in the references [65, 66], the

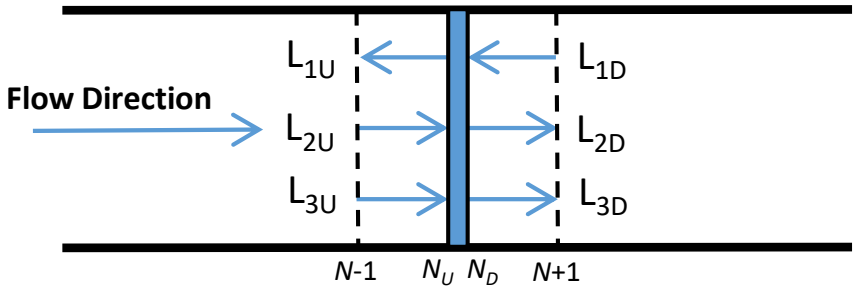

Figure 3.1: Compact Interface Element (CIE) with upstream and downstream nodes showing incoming and outgoing waves for subsonic flow

compressible Euler equations at each node can be represented in terms of three incoming, known characteristic waves (L_{1D}, L_{2U}, L_{3U}) and three outgoing, unknown characteristic waves (L_{1U}, L_{2D}, L_{3D}). For example, at the upstream node N_U, the time-derivatives of mass, momentum and energy fluxes can be written using the amplitudes of characteristic waves L_{iU}'s where $i = 1$, 2 and 3 as shown below:

$$\frac{\partial}{\partial t}(\rho A)_U = -(\rho V)_U \frac{\partial A}{\partial m} - \frac{A}{{c_U}^2}\left(L_{2U} + \frac{1}{2}(L_{1U} + L_{3U})\right) \tag{3.9}$$

$$\begin{aligned}\frac{\partial}{\partial t}(\rho V A)_U = &- (\rho V^2)_U \frac{\partial A}{\partial m} - \frac{A}{{c_U}^2}\left(\lambda_{2U} L_{2U} + \frac{1}{2}(\lambda_{1U} L_{1U} + \lambda_{3U} L_{3U})\right) \\ &+ (\rho A \Omega^2 r \cos(\beta)\sin(\eta))_U - C_f(\rho V^2 b)_U\end{aligned} \tag{3.10}$$

$$\begin{aligned}\frac{\partial}{\partial t}(\rho e_s A)_U = &- (\rho V h_s)_U \frac{\partial A}{\partial m} - \frac{A}{2}\left[\frac{L_{1U}}{\lambda_{1U}}\left(\frac{\gamma V_U - c_U}{\gamma - 1} + \frac{1}{2}\frac{{V_U}^2}{{c_U}^2}(V_U - 3c_U)\right)\right. \\ &\left. + \frac{L_{2U}}{\lambda_{2U}}\frac{{V_U}^3}{{c_U}^2} + \frac{L_{3U}}{\lambda_{3U}}\left(\frac{\gamma V_U + c_U}{\gamma - 1} + \frac{1}{2}\frac{{V_U}^2}{{c_U}^2}(V_U + 3c_U)\right)\right] \\ &+ (\rho V A \Omega^2 r \cos(\beta)\sin(\eta))_U - C_q\end{aligned} \tag{3.11}$$

where $\lambda_{1U} = V_U - c_U$, $\lambda_{2U} = V_U$ and $\lambda_{3U} = V_U + c_U$ are the velocities of characteristic waves for the upstream node and c is the speed of sound. It can be noted that the above equations

include streamtube area variation and source terms for better accuracy of the procedure. In a similar way, the conservation equations can also be written for the downstream node N_D using the amplitudes of characteristic waves L_{iD}'s where $i = 1$, 2 and 3. To update the flow variables in time at both the nodes, it is required to determine all the incoming and outgoing waves. The incoming waves represent the flow information coming from inside the compressor domains, and so their amplitudes are related to the spatial gradients of flow variables computed at the nodes of CIE. The relations for these waves are given by

$$L_{1D} = \lambda_{1D} \left(\frac{\partial p}{\partial m} - (\rho c)_D \frac{\partial V}{\partial m} \right) \tag{3.12}$$

$$L_{2U} = \lambda_{2U} \left({c_U}^2 \frac{\partial \rho}{\partial m} - \frac{\partial p}{\partial m} \right) \tag{3.13}$$

$$L_{3U} = \lambda_{3U} \left(\frac{\partial p}{\partial m} + (\rho c)_U \frac{\partial V}{\partial m} \right) \tag{3.14}$$

The above gradients in terms of mean-line coordinate m are calculated using one-sided differences in the relevant direction. For determining the outgoing waves, three additional relations are required to be specified along with the equations (3.12)-(3.14). Based upon the physics of CIE, following relations are proposed as governed by the conservation laws:

1. *Conservation of mass*: The incoming mass flux at N_U should be same as the outgoing mass flux at N_D. This gives

$$(\rho V A)_U = (\rho V A)_D \tag{3.15}$$

2. *Conservation of energy*: The interface is adiabatic and does not generate or lose energy in any form. Hence, the total enthalpy on either side of the interface must be

the same. This gets expressed as

$$\left(h + \frac{1}{2}V^2\right)_U = \left(h + \frac{1}{2}V^2\right)_D \tag{3.16}$$

3. *Conservation of momentum*: Figure 2.3 shows that the inlet turning process results in the formation of a throat having cross-section A_t. This inlet turning process is implemented in CIE, and as a result, one could approach the throat from both the upstream and downstream nodes. In either case, Mach number at the throat should come out to be the same, which readily gives the necessary matching condition as

$$\begin{aligned} (M_t)_U &= (M_t)_D \qquad \text{if} \quad (f_t)_U \geq f^* \\ (M_t)_U &= 1.0 \qquad \text{if} \quad (f_t)_U < f^* \end{aligned} \tag{3.17}$$

   At high subsonic inlet Mach number, the throat could get choked (particularly valid for high mass flow rates or high compressor speeds). In such case, the bottom condition shown in equation (3.17) must be used.

The throat Mach number M_t is related to the f value at the throat, i.e., f_t according to the equation (2.12). It should be stressed that the upstream Mach number $(M_t)_U$ is calculated using $(f_t)_U$ which satisfies equation (2.22) if the throat is approached from the upstream node. Similarly, the downstream Mach number $(M_t)_D$ is determined using $(f_t)_D$ which satisfies the sliding scale equation (2.28).

A general procedure for updating the flow variables at the CIE's upstream and downstream nodes at every time step is summarized as follows:

1. Calculate the incoming characteristic wave amplitudes (L_{1D}, L_{2U}, L_{3U}) using equations (3.12)-(3.14) by taking one-sided gradients. The characteristic velocities λ_{1D}, λ_{2U} and λ_{3U} are essentially evaluated at the respective nodes.

2. Guess initial values of unknown characteristic wave amplitudes (L_{1U}, L_{2D}, L_{3D}) and

update the flow variables at each node in time using equations (3.9)-(3.11) for the upstream node and similar equations for the downstream node.

3. Calculate the differences between left and right hand sides of the equations (3.15)-(3.17) and formulate an error vector containing three components (details of the procedure for a compact orifice are shown in Appendix B).

4. Perturb the unknown characteristic amplitudes one at a time, obtain 3×3 Jacobian matrix and determine the corrections for the initial guesses of the unknown amplitudes using Newton's method (details of the procedure are shown in Appendix C).

5. Go back to the previous step and repeat until the iterations converge as the specified tolerance criteria is met.

6. With all the characteristic amplitudes known, integrate the compressible flow equations to determine the state at the next time step.

Note that in the case of flow choking, the above described procedure breaks down into two sub-steps. The first step uses the bottom condition of equation (3.17) to obtain the one unknown characteristic amplitude at the upstream node, i.e., L_{1U}. The second step utilizes equations (3.15)-(3.16) and formulates a 2×2 Jacobian matrix during Newton's iterations for determining the unknown amplitudes, i.e., L_{2D} and L_{3D}.

3.3 Treatment for External Boundaries

The computational domain with streamtube sections and Compact Interface Elements is bounded at the ends by the inlet and outlet nodes. The boundary conditions at these ends are specific cases of the more general compact interface present between two domains (discussed in details in the Appendix B) and as such can be handled in a similar way. The treatment for these boundaries has been done using the characteristics-based approach, where the direction of these waves are shown in Figure 3.2. For subsonic inlet and subsonic outlet,

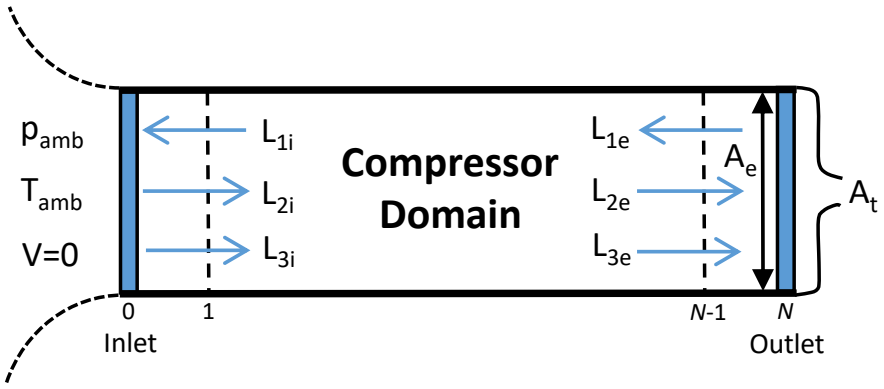

Figure 3.2: Direction of characteristic waves at the domain boundaries

three wave amplitudes (L_1, L_2, L_3) associated with the boundary element are required to be determined for updating the compressible flow equations at every time step. Each boundary is treated based upon the conditions known at that boundary.

3.3.1 Inlet Boundary

At the inlet, there is one characteristic wave L_{1i} which emerges from the domain and travels outwards. This characteristic amplitude is determined using the below expression:

$$L_{1i} = \lambda_{1i}\left(\frac{\partial p}{\partial m} - (\rho c)_i \frac{\partial V}{\partial m}\right) \tag{3.18}$$

where the wave velocity $\lambda_{1i} = V_i - c_i$, is calculated at the inlet boundary. To evaluate the unknown wave amplitudes (L_{2i}, L_{3i}), it is necessary to impose two additional constraints. The inlet boundary is exposed to the ambient and in the case of isentropic inlet, below two conditions get imposed:

1. *Total Pressure*: The total pressure at the inlet node should be same as the ambient pressure,

$$(p_s)_i = p_{amb} \tag{3.19}$$

2. *Total Temperature*: Similarly, the total temperature should be equal to the ambient

temperature,

$$(T_s)_i = T_{amb} \tag{3.20}$$

Specifically, two error functions are formulated using equations (3.19) and (3.20). Thereafter, Newton's iterations, as shown in appendix C, are performed to evaluate L_{2i} and L_{3i}.

3.3.2 Outlet Boundary

The compressor exit is connected to a choked throttle and there is only one unknown amplitude L_{1e} corresponding to one constraint. The known wave amplitudes are calculated using the following relations by taking one-sided gradients along the mean-line:

$$L_{2e} = \lambda_{2e}\left({c_e}^2\frac{\partial \rho}{\partial m} - \frac{\partial p}{\partial m}\right) \tag{3.21}$$

$$L_{3e} = \lambda_{3e}\left(\frac{\partial p}{\partial m} + (\rho c)_e\frac{\partial V}{\partial m}\right) \tag{3.22}$$

where $\lambda_{2e} = V_e$ and $\lambda_{3e} = V_e + c_e$. Flow from the compressor exit to the throat of choked throttle is taken to be isentropic, and the throat area A_t is expressed in terms of compressor exit area A_e and Mach numbers at those two locations. Using compressible flow area ratio relation [67], this gives

$$\frac{A_t}{A_e} = \frac{M_e}{M_t}\left(\frac{2+(\gamma-1){M_t}^2}{2+(\gamma-1){M_e}^2}\right)^{\frac{\gamma+1}{2(\gamma-1)}} \tag{3.23}$$

For the choked throttle, $M_t = 1$ and $A_t = A^*$ which upon substituting in the above equation readily results in

$$\frac{A^*}{A_e} = M_e\left(\frac{\gamma+1}{2+(\gamma-1){M_e}^2}\right)^{\frac{\gamma+1}{2(\gamma-1)}} \tag{3.24}$$

In the above, the choked throttle area A^* is specified according to a particular throttle setting and then used as the necessary error formulation condition to determine the unknown wave

amplitude L_{1e}.

3.4 Inclusion of Large Plenum as a Lumped Element

A large plenum can be included as a lumped element at the compressor end. Here, the problem is approached by neglecting any kinetic energy inside the volume, thus ignoring the propagation of acoustic waves that would otherwise be present inside a real plenum. Consider the schematic shown in Figure 3.3, where the flow enters the plenum at a rate $\dot{m}_{in}$ and leaves towards ambient through a throttle at flow rate $\dot{m}_{out}$. Assuming the exit flow state to be the same as the plenum state, an energy balance across the volume gives

$$\frac{d}{dt}(M_p c_v T) = \dot{h}_{s,in} - \dot{h}_{s,out} = \dot{m}_{in} c_p T_{s,in} - \dot{m}_{out} c_p T \tag{3.25}$$

where M_p is the mass of air in plenum, $T_{s,in}$ is the total temperature of inflow and T is the plenum temperature. Now using perfect gas law under the plenum condition provides

$$M_p = \frac{pV_p}{RT} \tag{3.26}$$

where V_p is the plenum volume, and uniform pressure and temperature is assumed inside the plenum. In case of choked throttle, the exit mass flow rate becomes a function of plenum

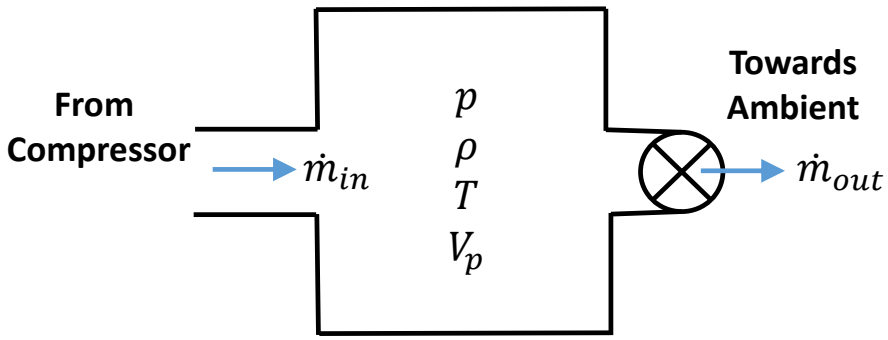

Figure 3.3: Schematic of lumped plenum connected to the compressor exit

temperature and pressure. Using the choked throttle relation, this can be written as

$$\dot{m}_{out} = K\frac{p}{\sqrt{T}} \tag{3.27}$$

where K is the throttle constant and governs the throttle position. Now substituting equations (3.26) and (3.27) into equation (3.25) provides the following first-order equation:

$$\frac{V_p}{\gamma - 1}\dot{p} + Kc_p\sqrt{T}p = \dot{m}_{in}c_pT_{s,in} \tag{3.28}$$

In addition to the energy conservation equation, the conservation of mass gives

$$\dot{M}_p = \dot{m}_{in} - \dot{m}_{out} = \dot{m}_{in} - K\frac{p}{\sqrt{T}} \tag{3.29}$$

Equations (3.28) and (3.29) can be integrated in time to update the plenum pressure and mass. Further, the plenum temperature can be updated using equation (3.26).

Note that under steady state, the plenum temperature is same as the inflow total temperature, i.e., $T = T_{s,in}$ and the throttle constant is given by

$$K = \frac{\dot{m}_{char}\sqrt{T_{s,in}}}{p_{char}} \tag{3.30}$$

where the combination of $\dot{m}_{char}$ and p_{char} is a stable point on the compressor characteristic curve. Hence, K can be easily updated during the unsteady simulations to achieve a different point on the compressor curve.

The above discussed lumped plenum model can be easily integrated within the outlet boundary condition. As shown in Figure 3.2, the exit boundary needs only one characteristic amplitude L_{1e} to be determined. The necessary error condition can be formulated by first calculating $\dot{p}$ from equation (3.28), which is here referred to as $\dot{p}_{plenum}$, and further matching the same with $\dot{p}$ evaluated at the exit node from the 1D compressible flow equations

(3.9)-(3.11). This can be easily expressed as

$$(\dot{p})_e = \dot{p}_{plenum} \tag{3.31}$$

3.5 Numerical Considerations for Nodes Adjacent to Compact Interface

This section addresses the case of numerical integration at the nodes adjacent to the compact interface. It should be noted that the central-differencing based KT scheme requires information at a total of five grid points, including two ahead and two behind. Consequently, when an interface or a boundary is approached, this scheme cannot be applied as the adjacent nodes will require points beyond the interface. For example, if the interface is denoted by node N, updating state variables at the node $N-1$ using the KT scheme would need data at $N-3$, $N-2$, $N-1$, N and $N+1$ grid points. This would, in turn, violate the interface condition and thus would prevent compact interface element to behave as the boundary element. Therefore, an alternative scheme that requires only one extra point at each side is required at the points adjacent to the interface or boundary. For this purpose, the three-point stencil central difference scheme is used, which in semi-discrete form can be written as

$$\frac{\partial U_j}{\partial t} = -\frac{H_{j+1} - H_{j-1}}{2\Delta m_{j,c}} + Q(U_j) \tag{3.32}$$

The numerical flux H in this case is the same as the physical flux F, which implies

$$\begin{aligned} H_{j+1} &= F(U_{j+1}) \\ H_{j-1} &= F(U_{j-1}) \end{aligned} \tag{3.33}$$

3.6 Summary

The central-difference based numerical scheme considered in this chapter is essentially a Riemann-solver-free scheme, which directly calculates the numerical fluxes in terms of the

physical fluxes, so can be easily implemented. Further, the discussed characteristics-based theoretical framework of treating dynamic compact interface as a boundary element presents a general approach for incorporating complex loss mechanisms in the compact form. The choking of the compressor is entirely governed by the choking of one of the compact interfaces implemented between the blade rows. The boundary conditions, in a similar way, have been treated by adopting the characteristics-based approach.

CHAPTER 4

MODEL ASSESSMENT AND VALIDATION STUDIES

In this chapter, the streamtube model as described earlier is used to predict the performance of a four-stage axial compressor with and without a centrifugal stage attached behind it. First, the ideal performance of the axial compressor, i.e., without any losses is predicted. Next, the steady model is tuned by introducing losses and making use of the measured data. Finally, the performance of axial-centrifugal compressor is predicted using the tuned model. Thereafter, a general instability criteria is proposed, which is further validated with the measured data.

4.1 Geometry and Ideal Compressor Performance

The flow path through the simulated compressor is shown in Figure 4.1. The annulus of the axial compressor contains a total of nine blade rows including Inlet Guide Vanes (IGVs), four rotors and four stators. In the nominal configuration, a throttle is placed at the exit of 90 degree bend to control the flow rate through the axial-centrifugal compressor. A

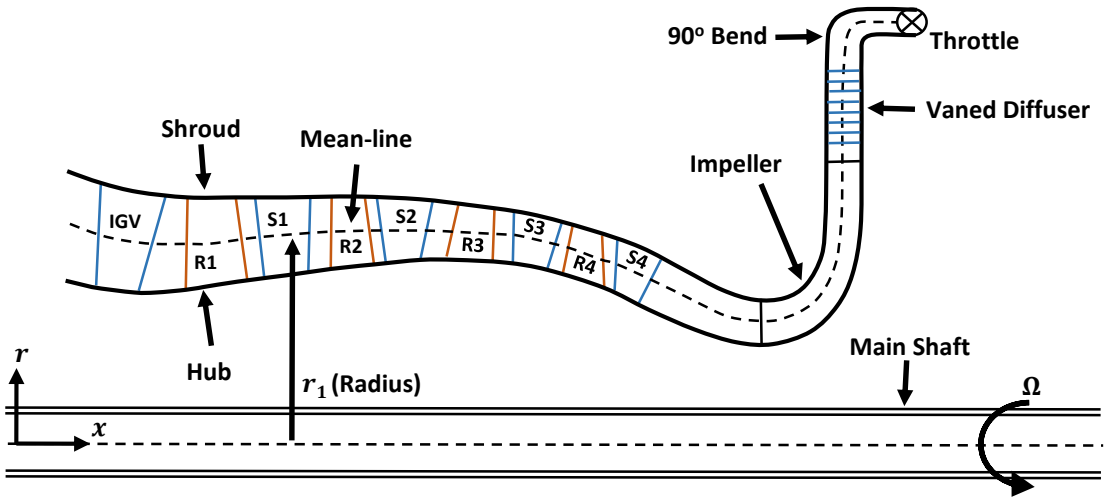

Figure 4.1: Schematic of flow path through the axial-centrifugal compressor

fixed throttle position, if stable, thus determines the equilibrium point on the compressor characteristic curve.

Let us first consider the axial stages of this Honeywell compressor terminated at the exit of stator 4. The ideal stage diffusion model, as described in section 2.1.1, is now implemented to perform the stage-by-stage calculations at nominal speed (100% RPM). Figure 4.2 shows a comparison plot between the compressor performance with ideal diffusion process and the measured data at the nominal speed. The mass flow rate and stagnation pressure ratio have been normalized by suitable reference states. The efficiency has also been normalized by reference value as will be done in the rest of this thesis. As can be clearly seen, the ideal compressor generates significantly higher stagnation pressure, typically more than three to four times than the actual compressor in the relevant range of operation. It should be noted that in this ideal process, the pressure ratio continuously rises as the flow rate is decreased. Further, the adiabatic efficiency is calculated out to 100%. Additionally, the compressor fails to choke even at very high flow rates. The reason behind this deviation between the ideal and actual performance is the loss of stagnation pressure in the diffusion process of actual stage. Due to the absence of losses, this ideal diffusion process fails to capture the

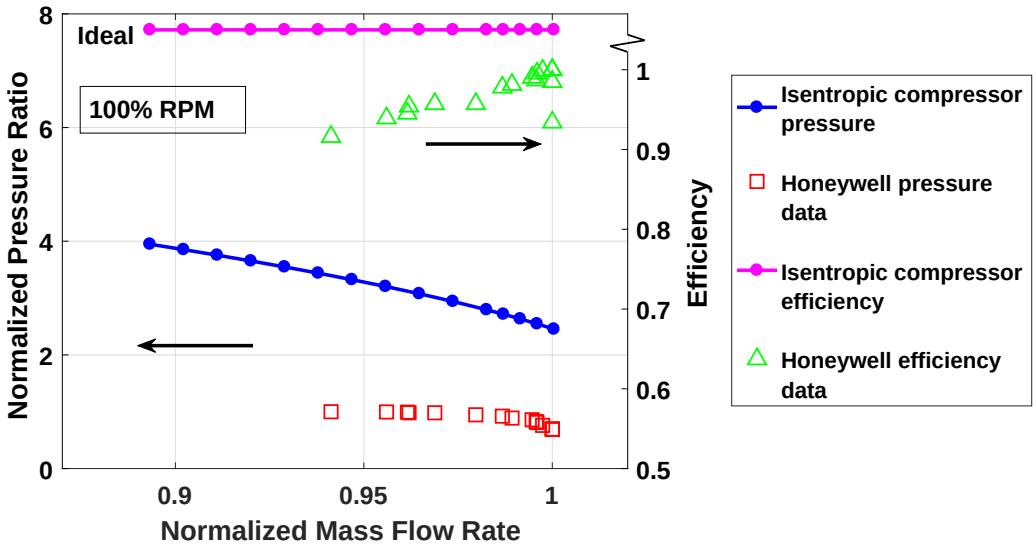

Figure 4.2: Comparison of ideal compressor performance with the measured data for four-stage axial compressor at 100% speed

actual compressor performance. Moreover, the compressor operating line fails to curve properly at high and low flow rates, thus excluding the critical phenomena like flow choking and stalling, which essentially govern the stable range of operation.

4.2 Model Tuning and Steady Performance Results

The steady state model incorporates losses as a mechanism to predict the performance of the four-stage axial compressor whose ideal performance was shown in the previous section. For any useful model prediction, the losses need to be tuned in as accurately as possible. For this, two tuning processes, as explained next, are tried.

4.2.1 First Tuning Process

The model tuning, as shown in Figure 4.3, has been done using the measured data at the 100% speed. To start with, the mixing loss factor ξ_{ml} is taken to be zero, which leaves the inlet turning process independent of any external model parameter. The wall friction and tip clearance losses have been included in all the predictions, which come out to be around 3% for this high-speed compressor. The trailing edge deviation leading to near 20% reduction in the turning angle has also been accounted. The null mixing losses result in predicted choked flow as 0.7% higher than the measured value. Further, upon reducing the mass flow rate, the stagnation pressure ratio comes out to be significantly higher and reaches about 30% larger value at the measured surge flow rate. The predicted efficiency for the desired flow rates, however, seems to follow the data points quite closely. At the measured surge data point, the flow rate is frozen and the parameter ξ_{ml} is gradually increased, which results in significant drop in the pressure with negligible change in the efficiency.

When the predicted pressure reaches the measured value, the mixing loss factor ξ_{ml} which comes out to be around 1.78% is frozen and the entire operating line is traced by increasing the flow rate until the choking occurs. As can be seen in Figure 4.3, the efficiency hardly changes even though the mixing losses are increased substantially, while a significant

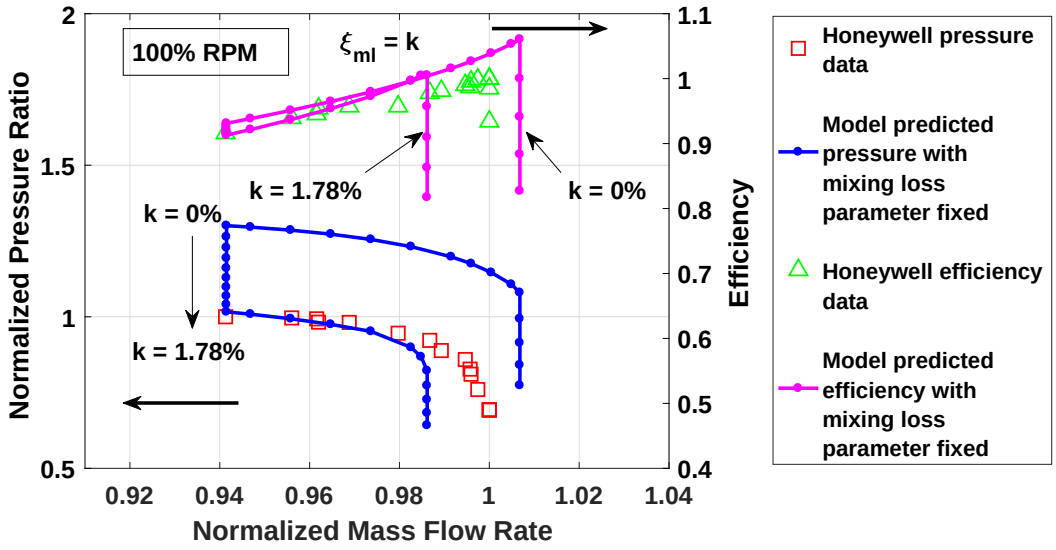

Figure 4.3: Adjustment process of ξ_{ml} at 100% speed for model with $\xi_{ml} = k$

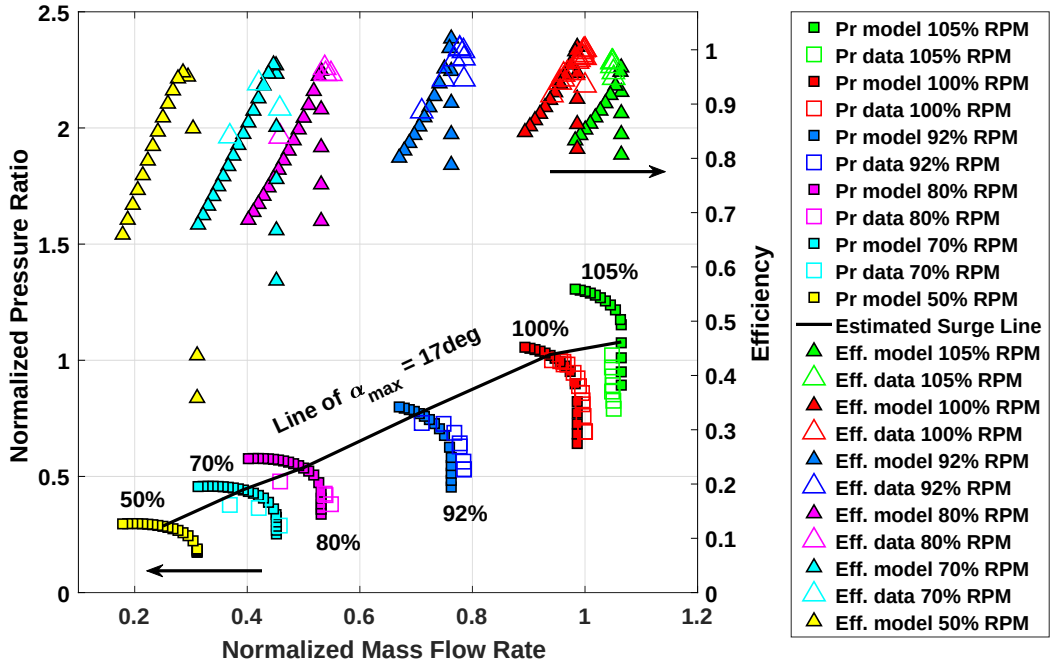

Figure 4.4: Predicted and measured pressure ratios and efficiencies at various compressor speeds for model $\xi_{ml} = k$ with $k = 0.0178$

pressure drop is observed. This looks little surprising at first glance since an increase in mixing losses in a stage would induce higher losses in that stage. However, looking into the model's stage-by-stage predictions, it is found out that indeed the losses in the front stages

do increase with increase in ξ_{ml}. However, these excess losses cause a temperature increase, thus velocity increase which tends to reduce the angle of attack in the succeeding stages. This reduction in the angle of attack further decreases the stagnation pressure rise and at the same time causes a decrease in the turning losses. This actually results in the back stages to gain efficiency, ultimately keeping the overall compressor nearly neutral with respect to the total efficiency change. Further, it can be observed from Figure 4.3 that the pressure as well as the efficiency follow closely the data points and choking happens at a flow rate less than 1.4% of the last measured data point.

Once the parameters of the model get established, they are not perturbed any further. For part-speed predictions, only the IGVs and stators' angles get modified as prescribed for that particular speed. The vanes schedule, as can been seen in Table 4.1, shows that IGVs and first stator are reset to high angles for better matched stages at speeds below 90%. Next, the performance maps are predicted in large range of speeds from 50% to 105%, and the results are shown in Figure 4.4. Here, some intermediate speed lines have been omitted for better clarity of the figure. Figure 4.4 shows that the model predicts the maximum flow at each speed with good accuracy but fails to curve properly near the surge flow rate, and further overpredicts the pressure ratios for most speeds. A neutrality of the slope as suggested by the data near the surge line does not get replicated, thus leading to the conclusion that this tuning process contains some deficiencies. As a result, a second tuning process, as explained next, is performed to improve the predictions.

4.2.2 Second Tuning Process

The tuning parameter ξ_{ml} is an indicator of the extent of mixing within each stage element, i.e., rotor and stator. Since each stage operates at a different incidence angle, in this second tuning process, ξ_{ml} is taken to be a function of the incoming angle of attack α. A linear symmetric relationship of the form $\xi_{ml} = k|\alpha|$ seems to work well, where k is used as the tuning parameter. As shown in Figure 4.5, first the null mixing branch is traced with

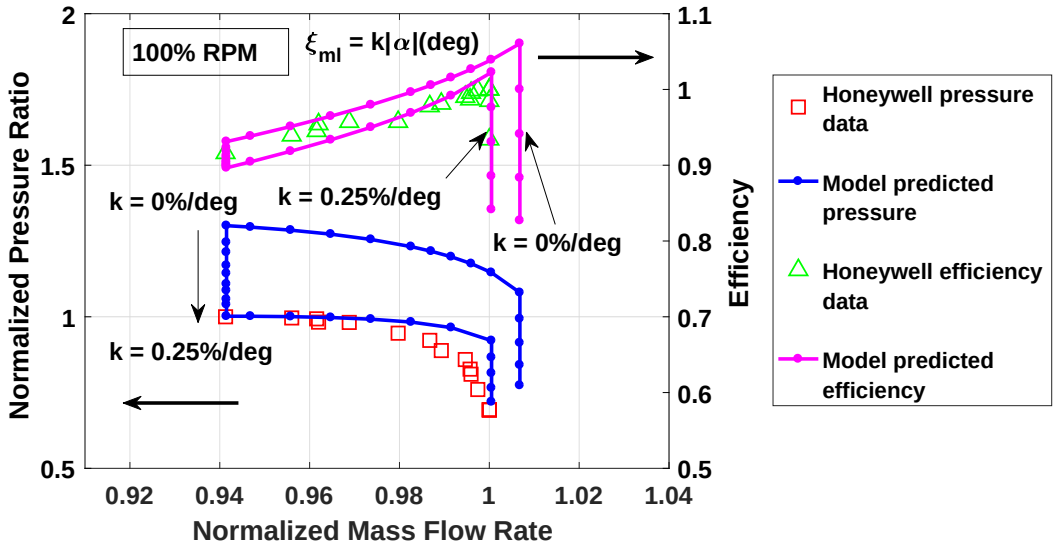

Figure 4.5: Adjustment process of $d\xi_{ml}/d|\alpha|$ at 100% speed for model with $\xi_{ml} = k|\alpha|$

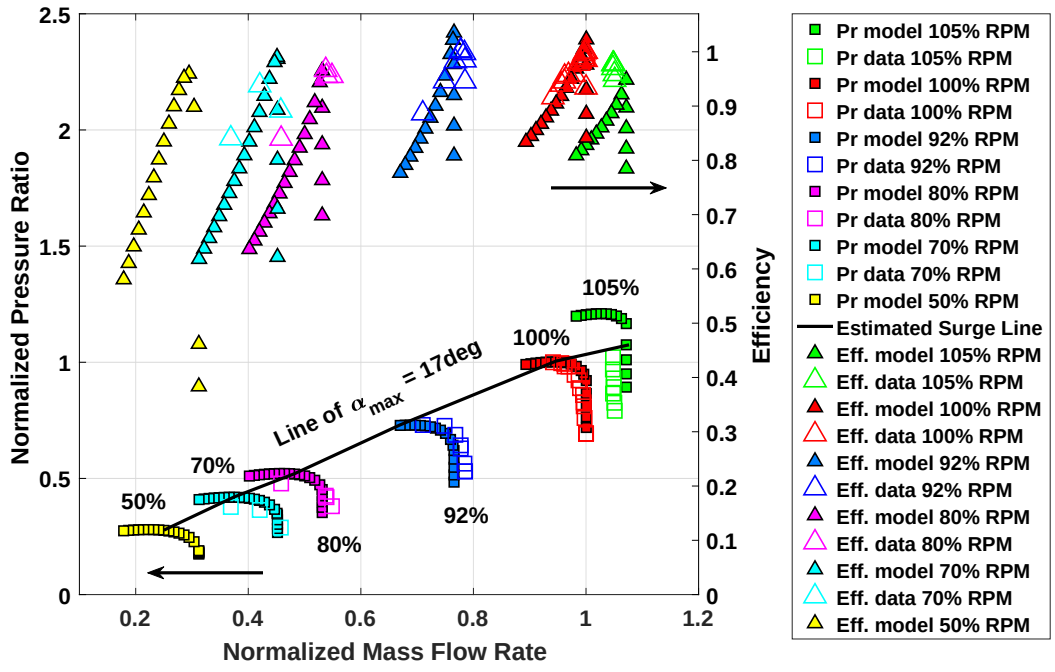

Figure 4.6: Predicted and measured pressure ratios and efficiencies at various compressor speeds for model $\xi_{ml} = k|\alpha|$ with $k = 0.0025$

$k = 0\%$/deg and at the measured surge flow rate, k is slowly increased starting from the maximum pressure ratio. This causes a reduction in pressure ratio in the form of a vertical drop where a good match is obtained for $k = 0.25\%$/deg. During this tuning process

too, isentropic efficiency hardly changes as an increase in losses in the front stages gets compensated by lower losses in the last stages, essentially keeping the overall efficiency nearly the same. Next, the pressure ratio is traced for higher flow rates with this k value, which as can be seen from the figure results in exact match for the choked flow rate.

After establishing the model parameter k, pressure ratios and efficiencies are predicted for different compressor speeds ranging from 50% to 105% as shown in Figure 4.6. The measured data for various speeds has also been shown for quick comparison, which points out a good match for the stagnation pressure ratios and choked flow rates. Note that the last case of 50% speed does not have any measured data for the comparison. As can be further noted, the model closely follows the data points and captures correctly the slope of pressure characteristics near the surge line. The choked flow rate also turns out to be predicted accurately for all the speeds, except for 105% at which it is calculated out to be slightly higher than the measured value. The surge line has been drawn by taking the critical angle of attack to be 17 degrees, which coincides well with the near neutral slope of the characteristic curves (except for the 105% speed case) as they cross the surge line. This stall condition ($\alpha > \alpha_c$), being simple in nature, is so-chosen to match the surge data point at the 100% speed and seems to follow the surge points at other speeds quite well.

As for further validation, the model with the same tuned parameters, i.e., 3% wall friction and tip leakage losses, around 20% trailing edge deviation and $k = 0.25\%$/deg is used to predict the performance of NASA stage 37 [68] which is a highly loaded inlet stage. As can be seen from Figure 4.7, the agreement is pretty good for pressure ratios and efficiencies in speeds ranging from 50% to 100%. The mass flow rate and pressure ratio have been shown in the dimensional form since the data for NASA stage 37 is available in the open literature. A slight overprediction of the choked flow rate can be seen at speeds close to the nominal one. This mismatch can also be witnessed in the four-stage compressor for 105% speed, which thus indicates a slight underprediction of high-speed losses.

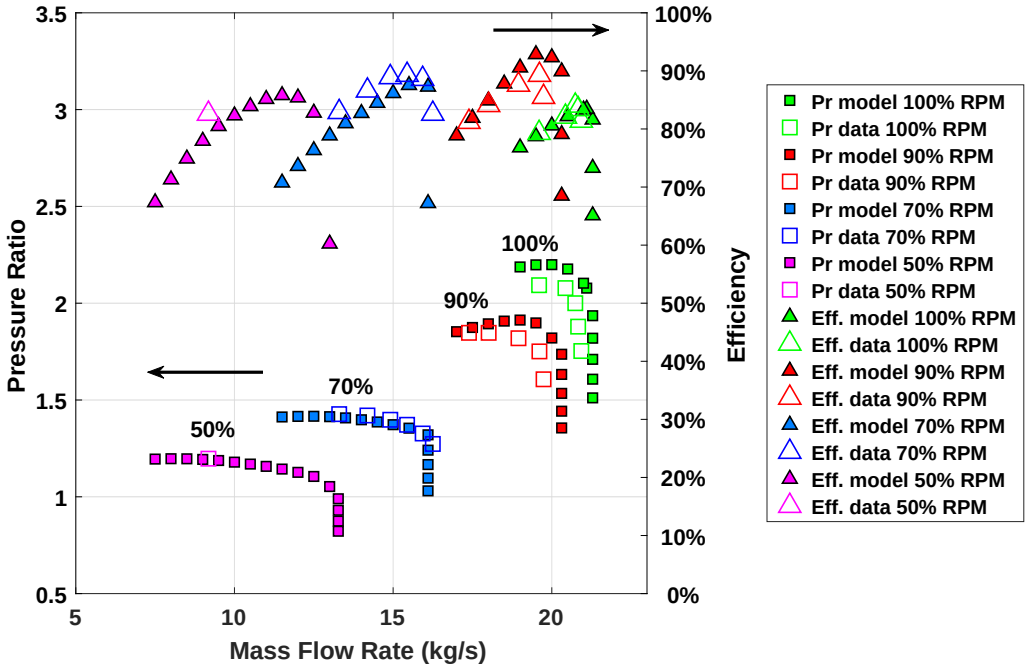

Figure 4.7: Predicted and measured pressure ratios and efficiencies for NASA stage 37 at various speeds using the tuned model

4.2.3 Further Assessment of Model Predictions

To further assess the model, individual stages of the four-stage compressor are analyzed. Figure 4.8 depicts the incidence or attack angle to various stage elements as a function of normalized flow rate at the 100% speed. It can be seen that it is the stator 4 which experiences highest angle of attack between the surge and maximum flow rates, and thus is going to stall first. Other stage elements remain below 11 degrees incidence. However, as the flow rate is increased, the incidence angle rapidly decreases for all the stages. Particularly for stator 1, the angle of attack is first to reach the zero degree mark, and thus becomes the cause of compressor choking due to the choking of turning element. Further, normalized pressure rise over each stage versus mass flow rate is plotted in Figure 4.9. The figure shows that stator 4 and much more so rotor 4 operate at positive pressure slope in large range of flow rates without destabilizing the compressor. Thus, it seems that the individual stage stall that occurs gradually, i.e., the soft stall is affecting the stability of the compressor by

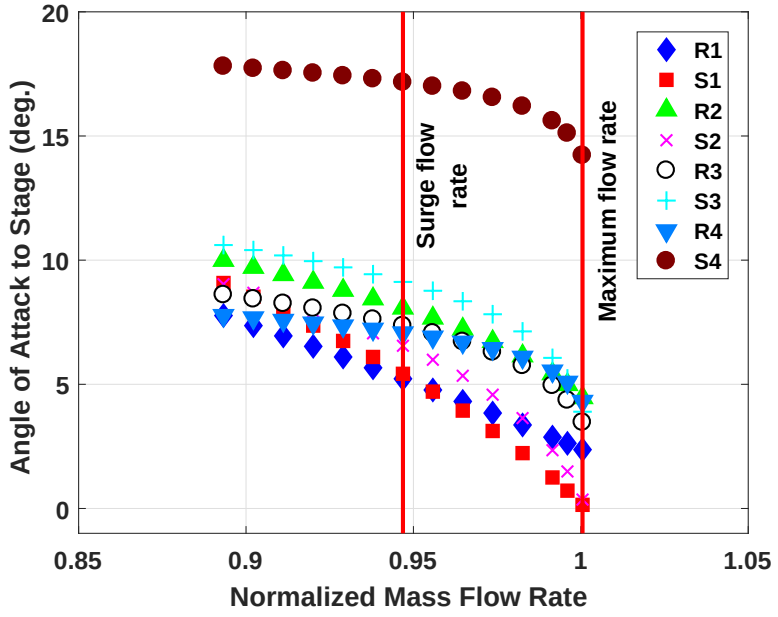

Figure 4.8: Predicted angle of attack (deg.) to various blade rows as a function of normalized flow rate for 100% speed

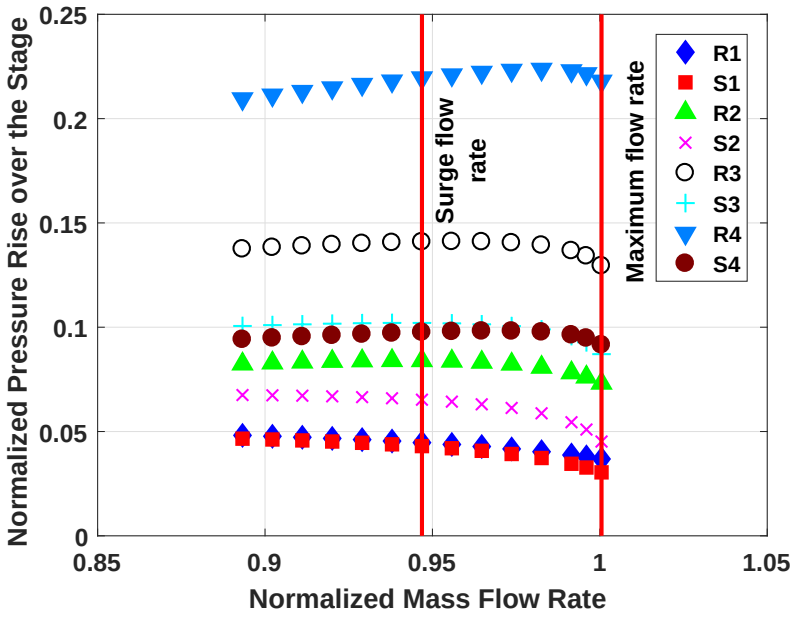

Figure 4.9: Predicted normalized pressure rise over various blade rows as a function of normalized flow rate for 100% speed

contributing to the overall pressure characteristic of the compressor, but by itself might not be sufficient for destabilizing the compressor.

Table 4.1: Summary of comparison between model predictions and measured data

Speed NC%	IGVs and vanes schedule (deg)				Maximum measured flow rate	Predicted choked flow rate	Predicted choked stage	Stage with highest angle of attack
	IGVs	S1	S2	S3				
105%	0	0	0	0	1.05	1.07	S1	S4
100%	2	0	0	0	1.00	1.00	S1	S4
97%	6.3	0.3	0	0	0.94	0.94	S2	S4
95%	13	2	-1.5	-3	0.86	0.85	S1	S4
92%	20	2.5	-2.3	-3	0.78	0.77	S1	S4
84%	30	10	1.5	-3	0.61	0.59	S1	S4
80%	33.4	12.7	5.5	-3	0.55	0.53	S1	S4
70%	36	16	4.8	-3	0.46	0.45	S1	S3
50%	40.6	20.8	3.5	-3	N/A	0.31	R4	R2

A summary of choked flow rate comparison between the model and measured data is presented in Table 4.1. The choked stage and likely to stall stage with highest angle of attack are also noted for various speeds. It can be seen that at high speeds, the compressor chokes at the first stage and likely to stall at the last stage. However for low speeds, the stalling stage moves to the front. With the exception of 50% speed, it is mostly one of the front stages which chokes the compressor. Overall, the comparison between predicted and choked flow rates is quite good and differs at most by 3%.

4.3 Overall Predictions for Axial-Centrifugal Compressor

After estimating the axial compressor performance, the tuned model is now used to predict the performance of axial-centrifugal compressor by adding centrifugal stage specific losses as mentioned earlier in the section 2.1.4. The turning, mixing, wall friction and tip leakage losses have also been included.

Figure 4.10 shows predicted pressured ratios for the entire axial-centrifugal compressor at different speeds. The axial compressor results, as obtained earlier, have also been shown on the left axis for reference. The peak pressure ratio of 1.0 at the nominal speed, as shown in the figure, is calculated by normalizing the axial-centrifugal pressure ratios using a different reference state. Importantly, it is found that at 92% speed and above, the axial-centrifugal compressor chokes due to the choking of stator 1, i.e., an axial stage. Below that speed, it is the vaned diffuser that chokes before any of the axial stages. Especially at low speeds, the difference between the choked flow rates of the two compressors is quite significant,

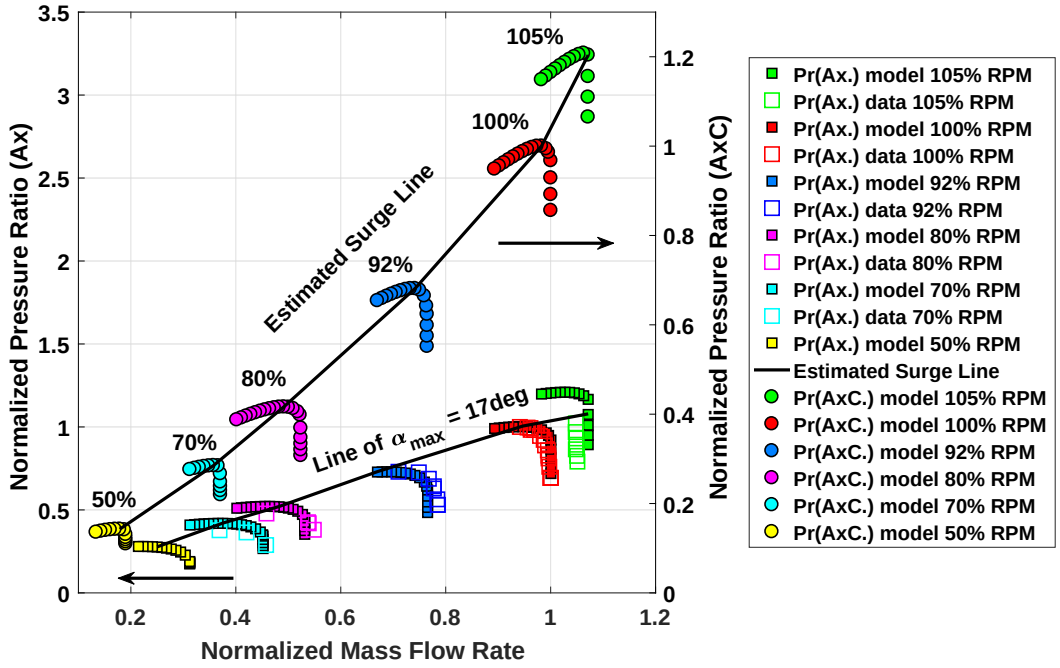

Figure 4.10: Predicted pressure ratios for the axial-centrifugal compressor at various speeds using the tuned model. The axial compressor predictions and data are shown for reference.

reaching approximately 39% for 50% speed and 18% for 70% speed.

Looking into the instability criteria for speeds 80% and above, the axial-centrifugal compressor reaches neutral slope at relatively higher flow rate than the axial one. Hence, it can be predicted that in case of large plenum present at the compressor end, the compressor would surge close to the peak pressure of constant speed curve. Therefore, it is the dynamic instability nearly governed by Greitzer's B-parameter [43] that leads to the compressor surge. Note that in the case of axial compressor, however, fundamental mode like rotating stall could manifest itself as the instability mode before any surge/reverse flow appears. The surge line, as shown in Figure 4.10, is drawn by taking the peaks of pressure characteristics, except for the 105% speed at which it is the abrupt stall of stage 4 that causes total flow breakdown. The axial compressor data shows that the surge point occurs very near to the peak of constant speed characteristic, which thus illustrates that this data is possibly collected by adding a large volume at the compressor end. Clearly, the role of plenum is quite crucial in dictating the surge boundary and would be explored in more details in the next chapter. However, at the 105% speed, instead of gradual slope change, it is the severe stalling of a highly-loaded stage which leads to stage breakdown and so plunges the compressor into surge.

The low-speed operation of the axial-centrifugal compressor, i.e., below 80% is different than the high-speed operation in a sense that both the choking and surging are controlled by the centrifugal stage. Considering its lower choked flow rates than the axial compressor, even though one or several of the axial stages might have been stalled, the compressor would still operate in a stable manner due to the efficient centrifugal stage. This can also be observed from the efficiency plots as shown in Figure 4.11, where at low speeds and close to the choked flow rates, the overall compressor is more efficient than the axial compressor. For close to the nominal speed operation, however, the addition of centrifugal compressor marginally changes the adiabatic efficiencies, and particularly for 100% and 105% speeds even reduces its peak value.

The flow field inside a centrifugal compressor is generally more complex than the axial

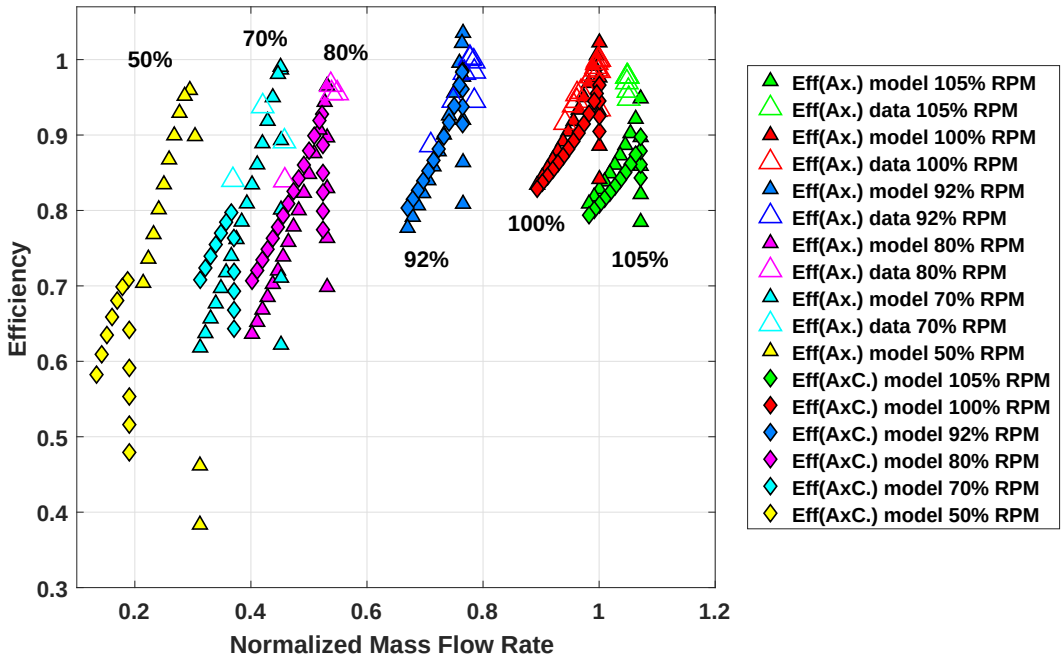

Figure 4.11: Predicted adiabatic efficiencies for the axial-centrifugal compressor at various speeds using the tuned model. The axial compressor predictions and data are shown for reference.

compressor and hence is more difficulty to analyze. An often mentioned feature in the literature [69], which can also be noted from Figure 4.10, is the small difference between the surge and choked flow rates at speeds close to the nominal one. Clearly, soon after getting out of the choke, the axial-centrifugal compressor will experience instabilities. Hence, it is crucial to maintain enough surge margin for rotorcraft/aircraft engines operating with the centrifugal compressors at high pressure ratios. Nevertheless, the issue of compressor instabilities would be explored in details in the next chapter through the simulation of unsteady flow model.

A summary of model predictions for the overall compressor is shown in Table 4.2. As mentioned earlier, at 92% speed and above it is the axial compressor that chokes first. Below that speed, compressor choking occurs due to the choking of vaned diffuser. Predicted first to stall stage is noted in the last column of the table, however, the stalling of a stage might or might not lead to compressor surge, i.e., complete flow breakdown. At and above 80%

Table 4.2: Summary of model predictions for the axial-centrifugal compressor

Speed NC%	IGVs and vanes schedule (deg)				Predicted choked flow rate	Predicted choked stage	Predicted first to stall stage
	IGVs	S1	S2	S3			
105%	0	0	0	0	1.07	Axial (S1)	Centrif.
100%	2	0	0	0	1.00	Axial (S1)	Centrif.
92%	20	2.5	-2.3	-3	0.77	Axial (S1)	Centrif.
80%	33.4	12.7	5.5	-3	0.52	Diffuser	Centrif.
70%	36	16	4.8	-3	0.37	Diffuser	Axial (S3)
50%	40.6	20.8	3.5	-3	0.19	Diffuser	Axial (R2)

speed, the centrifugal stage is predicted to stall first. However, one of the axial stages is likely to stall first at speeds lower than 80%, but might not initiate surge as the neutral slope of overall pressure characteristic would still have not been reached.

4.3.1 HECC Comparison and Diffuser Losses

NASA HECC was designed in collaboration with UTRC to represent the last stage of axial-centrifugal compressor, typically used in rotorcraft engines. The centrifugal compressor was successfully tested by Braunscheidel *et al.* [27] at NASA Glenn Research Center and was computationally analyzed by Medic *et al.* [70]. The predictions from the 1D model with the tuned parameters are now used to validate the results mentioned in the UTRC report.

Figure 4.12 presents incidence angle to the diffuser for nominal and low-speed (70% RPM) cases versus corrected flow rate along with the measured data. To validate the data,

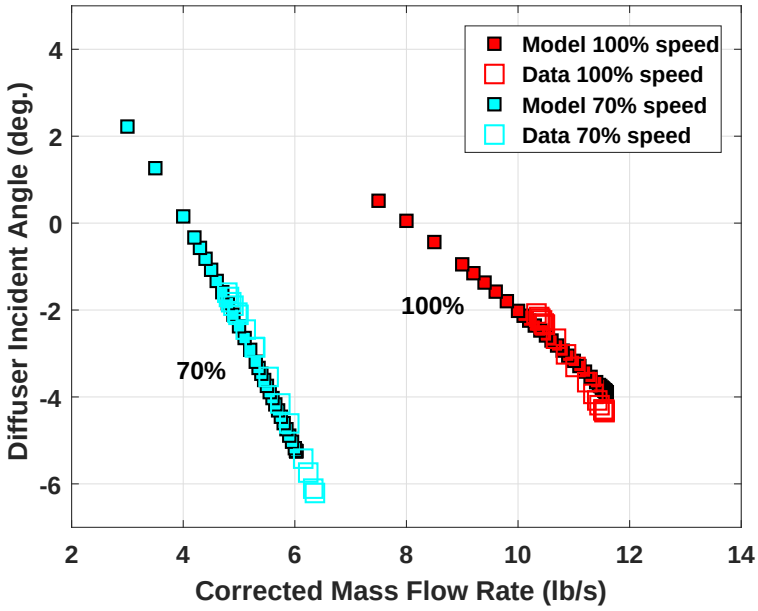

Figure 4.12: Comparison of predicted HECC diffuser incidence angle with data

model is applied solely to this centrifugal compressor without any front axial stages. As can be seen from the figure, the results perfectly match with the data except for the choked flow rate at the 70% speed, which is found to be slightly lower. Moreover, it is also observed that the diffuser operates at negative incidence for a wider flow range without introducing any "negative stall". As the compressor is throttled towards choke, Mach number at the diffuser throat is noted as shown in Figure 4.13. For both the speeds, throat Mach number initially decreases as the flow rate is increased, however, as the throat gets choked Mach number rapidly climbs up to the sonic value, thus choking the diffuser.

Figure 4.14 shows diffuser losses for HECC versus corrected mass flow rate, which again demonstrates a good match between the data and present model predictions. Close to the design point, losses are near to minimum, but reach high values for off-design conditions. The diffuser choking can also be demonstrated through this figure as the loss of incoming dynamic head rises steeply, reaching more than 80% close to the choke point. To calculate the vaned diffuser losses in the four-stage axial plus one-stage centrifugal compressor, the tuned model is further utilized. Figure 4.15 notes the diffuser losses for various speeds. For

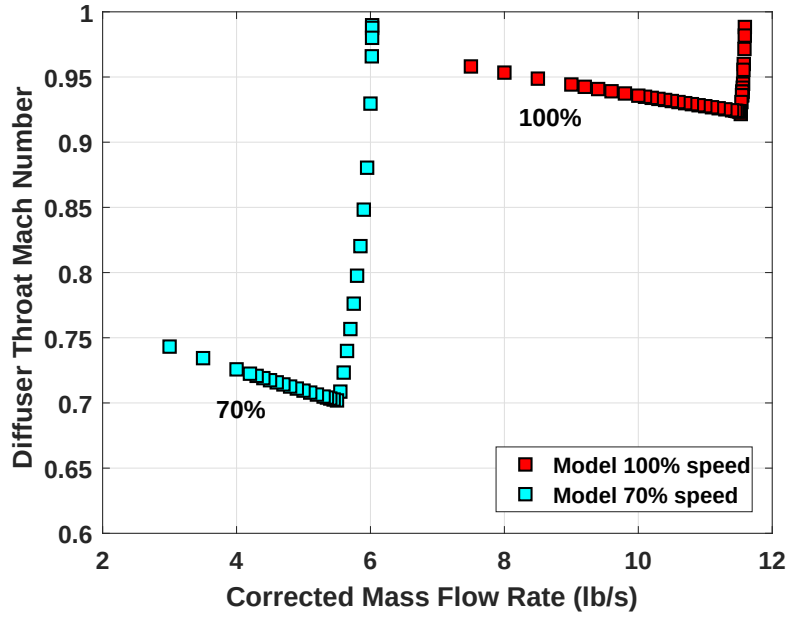

Figure 4.13: Diffuser throat Mach number for HECC at two speeds

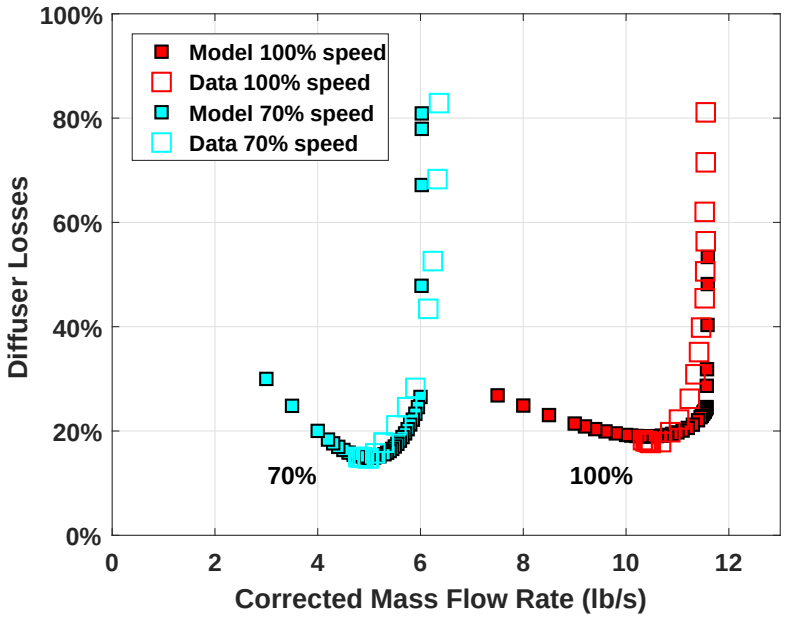

Figure 4.14: Comparison of predicted HECC diffuser losses with data

80% speed and below, since the compressor choking is controlled by the vaned diffuser, the losses are found to be high near the choked flow rates. For higher speeds, on the other hand, they more or less remain constant to around 20% value. Two particular features in the

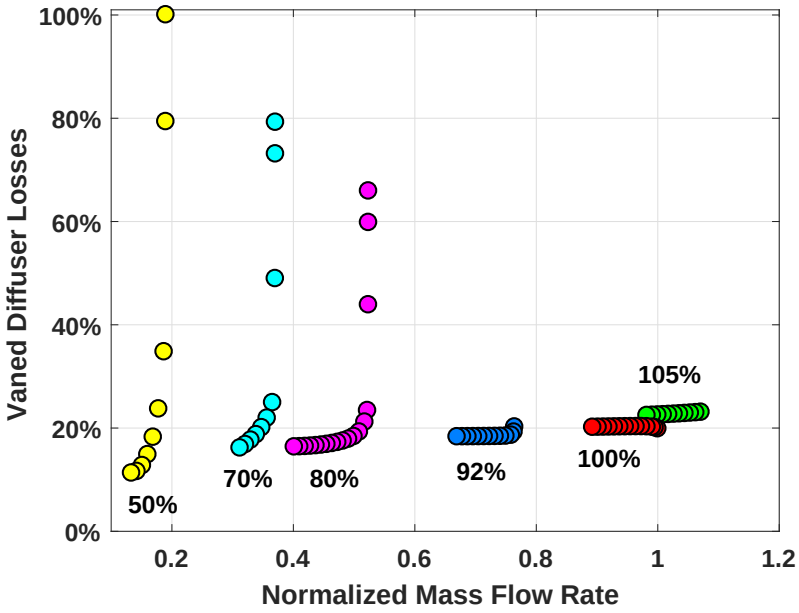

Figure 4.15: Losses in vaned diffuser for Honeywell axial-centrifugal compressor at various speeds

Honeywell compressor simulation: (a) occurrence of maximum 80% diffuser losses at the 70% speed, (b) presence of nearly 20% losses at the nominal speed similar to the HECC suggest that this centrifugal diffuser might have been designed on the lines of HECC.

Furthermore, a good match between the model results and HECC data demonstrates that the developed 1D model successfully captures majority of the impeller and diffuser losses. The predictions related to stage choking, diffuser incidence angle and diffuser separation losses also turn out to be quite accurate.

4.4 Evaluation of Trailing Edge Deviation Model

In the 1D model, flow deviation at the trailing edge is estimated according to the Carter's rule [53, 54] as depicted in equation (2.35). Deviation angle at the trailing edge of an axial stage is given by

$$\delta_{dev} = m\frac{\theta}{\sigma^n} \tag{4.1}$$

The parameters m and n are now varied from their tuned values of 0.2 and 1.0 respectively.

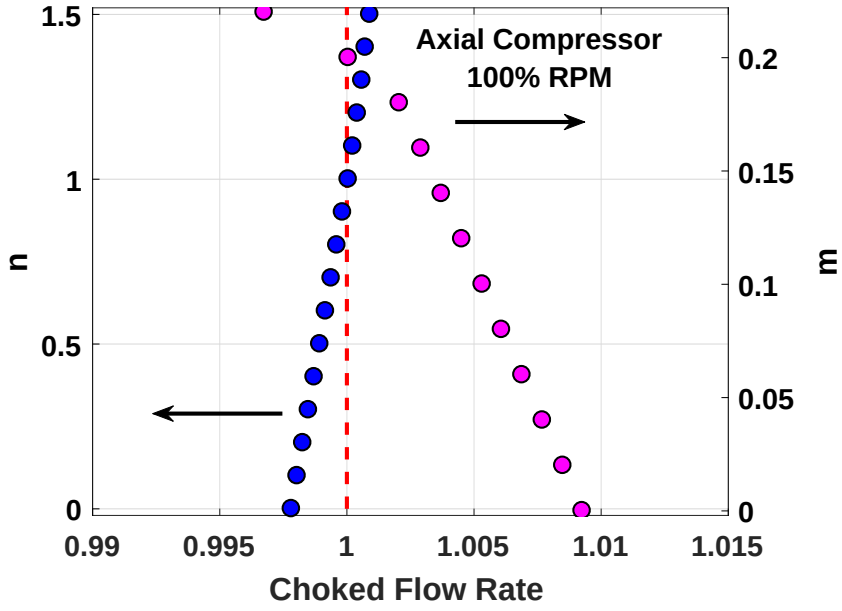

Figure 4.16: Trailing edge deviation model evaluation with choked flow rate variation shown versus parameters m and n

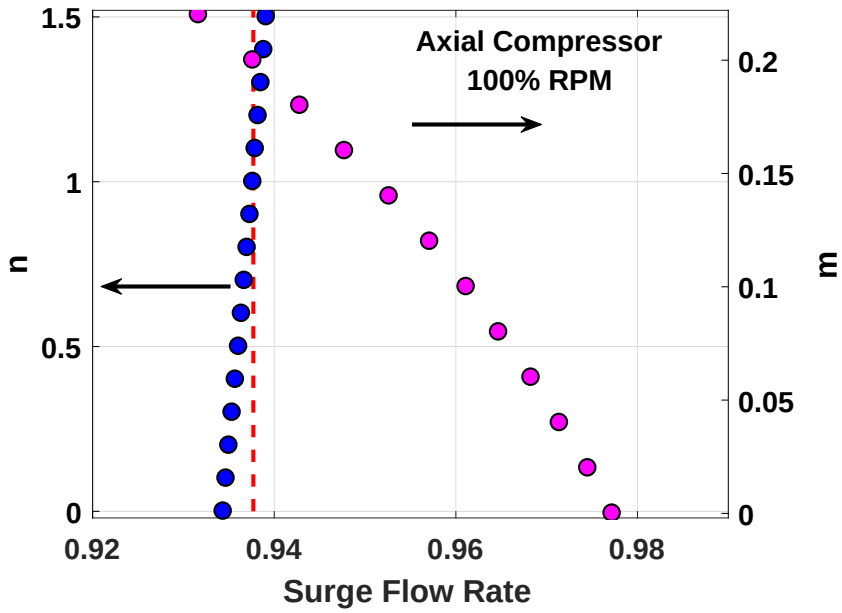

Figure 4.17: Trailing edge deviation model evaluation with surge flow rate variation shown versus parameters m and n

Figure 4.16 and Figure 4.17 illustrate changes in the choked and surge flow rates respectively for the four-stage axial compressor as the model parameters are modified. These flow rates

turn out to be more sensitive towards parameter m. A zero deviation from the geometric trailing edge, i.e., $m = 0$ could lead to incorrect predictions with nearly 1% error in the choked flow rate and 4% error in the surge flow rate. The parameter n, however, shows less sensitivity towards these flow rates and if taken to be zero would bring about less than 0.5% error. This is due to the near unity solidity (σ) of the axial stages, thus making this parameter less important for this compressor.

4.5 Instability Criterion and the Case of High-Speed Stall

As discussed earlier and shown in Figure 4.6, both the model and data agree that for the four-stage Honeywell axial compressor, stability gets lost when the overall characteristic changes slope. This is known to be true for a compressor operating with a large B-parameter which can easily be manipulated by changing the end plenum volume. In such a case, the compressor would become unstable close to the peak of overall characteristic, eventually leading to surge/flow reversal. However, for a compressor with low B-parameter or no end plenum, few stable operating points on the positively-sloped side of the characteristic could be obtained. As would be shown through the unsteady simulations, the instability mode which subsequently appears on the unstable branch then manifests itself in the form of an oscillatory pattern resembling an axial/longitudinal mode.

In some cases, typically at high speeds, the compressor loses stability even on the negatively-sloped side of the characteristic. The model can now be used to simulate this case when stability is lost due to an abrupt change in a stage characteristic initiated by sudden increase in losses. This scenario is simulated by introducing a sharp change in the mixing loss factor ξ_{ml}. In extreme cases, the change is abrupt and this parameter assumes its maximum possible value, i.e., $\xi_{ml,stall}$ = 1.0. For the discussion that follows, it shall be assumed that a stage that reaches 17 degrees angle of attack on the negatively-sloped side gets into such stall. For example, a high-speed close to 105% is chosen at which the compressor gets out of the choked conditions without stall, but upon slight flow rate

reduction crosses the critical angle of attack at one of the stages when the compressor characteristic is still at sharp negative slope. This behavior of the compressor characteristic is shown in Figure 4.18. The solid lines are the model predictions and the unconnected symbols are the data at 105% speed, shown here for reference. Let us now consider the process starting with the throttle line that intersects point 1 on the choked branch. As the throttle is closed, point 2 is reached where the compressor gets out of the choked conditions and as the throttle is gradually closed, point 3 is obtained where the angle of attack of stator 4 reaches 17 degrees. Now, this stator stalls followed by a sharp drop in the characteristic to point $3'$. This imbalance between the throttle and compressor characteristic would drive a tremendous pressure wave from back to front which upon arrival at the compressor inlet will get reflected as a strong expansion wave. These strong waves would cause flow reversal and the compressor would then plunge into surge. Point 4 which is depicted with a dashed throttle line is theoretically a stable point but there is no way to reach it without experiencing violent stall in the process. Thus, with this kind of stall the compressor cannot operate with

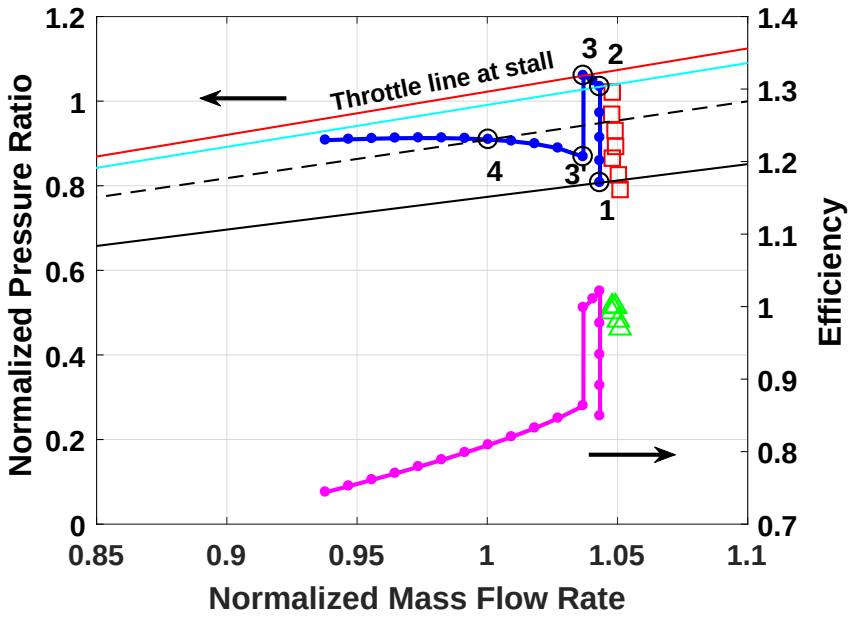

Figure 4.18: Compressor pre- and post-stall characteristics at high-speed with criticality criterion invoked, the unconnected symbols are 105% speed data

a fully stalled stage.

Camp & Day's study [71] on spike and modal stall phenomena also demonstrates this critical incidence idea. Their simple model illustrates that compressor stalls on the negatively-sloped side if the critical incidence value is reached. On the other hand, if the peak of overall characteristic is reached before the critical incidence value, the compressor would stall through modes occurring at the peak.

4.6 Summary

The model validation and assessment studies in this chapter provide a viable way to benchmark the reduced-order 1D model. It has been shown that the tuning parameter ξ_{ml} plays a crucial role in the overall predictions. For the four-stage axial compressor, the choked flow rate and surge point at various speeds are accurately predicted when ξ_{ml} is modelled as a function of incoming angle of attack α. For the other three compressors (NASA stage 37, axial-centrifugal and HECC), the tuned model provides reasonable results and correctly validates the compressor performance data trends. Regarding the instability criterion, the steady model illustrates the neutrality of characteristic slope as a valid criterion for nominal and part-speeds. In case of a complete stage breakdown, however, the compressor cannot operate in a stable manner even when the slope of characteristic is still negative.

CHAPTER 5

DYNAMIC MODEL EVALUATION AND COMPRESSOR INSTABILITIES

Continuing on to further analyze the proposed compressor fluid dynamic model, this chapter evaluates the dynamic performance using the unsteady runs. First, the four-stage axial compressor is simulated and its performance on the choked side is demonstrated. Next, the crucial area of compressor instabilities is explored by analyzing the loss of stability for different B-parameter values. In this chapter, the B-parameter has been simply manipulated by changing either the end-volume size or the compressor shaft speed. Further distinction between the stall at low and high speeds is done using the unsteady simulations. Finally, the performance of axial-centrifugal compressor is simulated on the stall side for both the speeds.

5.1 Unsteady Simulation of Axial Compressor

In this section, the results of unsteady simulations for the four-stage axial compressor, as discussed earlier, are presented. The nominal configuration of the simulated compressor is shown below in Figure 5.1. In this configuration, stator 4 discharges into the plenum which is interfaced to the ambient through a throttle. With plenum of volume 2.2 cu. ft. and length

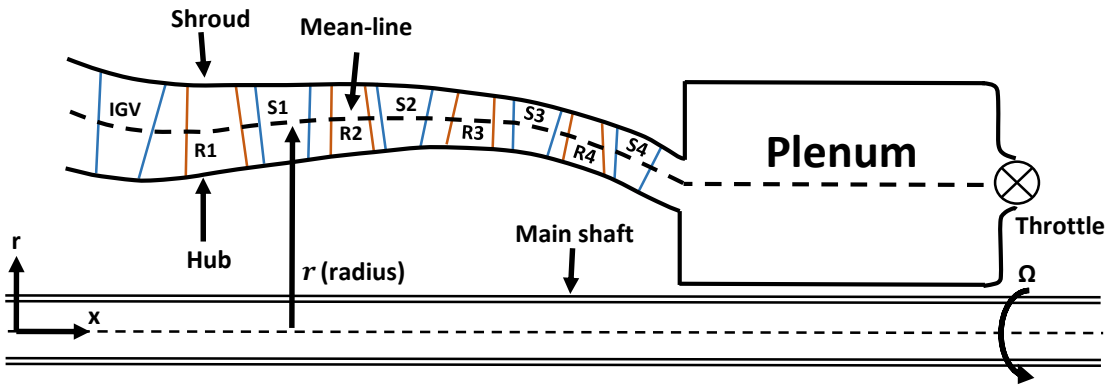

Figure 5.1: Geometry of simulated four-stage axial compressor with an end plenum

1 ft., the B-parameter is calculated out to be around 0.94. According to Greitzer's theory and associated measurements [45], this is above the critical value at which the instability modes get transitioned from rotating stall to surge. The dynamic behavior of the compressor is also investigated with reduced B-parameter when the throttle is connected directly to the exit of stator 4.

A transient simulation requires an initial distribution of state variables for the time-marching procedure. For this, steady form of the flow equations (2.69)-(2.73) are solved over the mean-line to provide the necessary initializer routine. The inlet is at standard sea-level conditions ($p = 101.325$ kPa, $T = 288.15$ K) and no other model parameter is varied except for the skin friction coefficient (C_{fw}) which is tuned to match the nominal choked flow rate between the steady initializer and stage-by-stage calculations as described in the previous chapter. First, a mesh sensitivity study is conducted to validate the numerical procedure, as shown in Table 5.1. Considering a stable point on the negatively-sloped side of the compressor characteristic (point 1 in Figure 5.2), the table shows that with maximum CFL number of 0.92, the variations in pressure and mass flow rate between the nominal and refined grids appear only after four decimal places. These results are deemed good and for all the subsequent calculations in this chapter, the nominal grid has been used.

Table 5.1: Summary of mesh refinement study using two different grids

Case	Δm	Δt	Max. CFL number	Exit $\dot{m}$	Exit p
Nominal Grid	1.52 mm	0.2 μs	0.92	0.984641	0.919642
Refined Grid	0.76 mm	0.1 μs	0.92	0.984653	0.919680

5.1.1 Throttling and Choking at the Nominal Speed

The inclusion of a "large" plenum in 1-D scheme may be done in two ways. If the plenum has large enough aspect ratio, it can be included as a part of the waveguide passages in the scheme, where the governing equations as discussed in the Chapter 3 are solved. This requires proper interface to the compressor on one side and throttle on the other. Otherwise, the plenum can be evaluated as a lumped volume in which the velocity is negligible and the pressure is uniform throughout the volume. In the results shown below, both the approaches are followed to demonstrate the choking process.

With a real plenum present, Figure 5.2 shows the progression from an initial stable point towards and into the choked branch. The steady points shown in this figure as well as in the other figures are obtained from the initialization procedure which is part of the numerical scheme. In the initializer routine, a flow rate is set and the pressure distribution along the compressor is calculated. The required throttle area is also calculated as a part of the initializer routine by assuming the throttle to be choked. The calculated spatial distribution

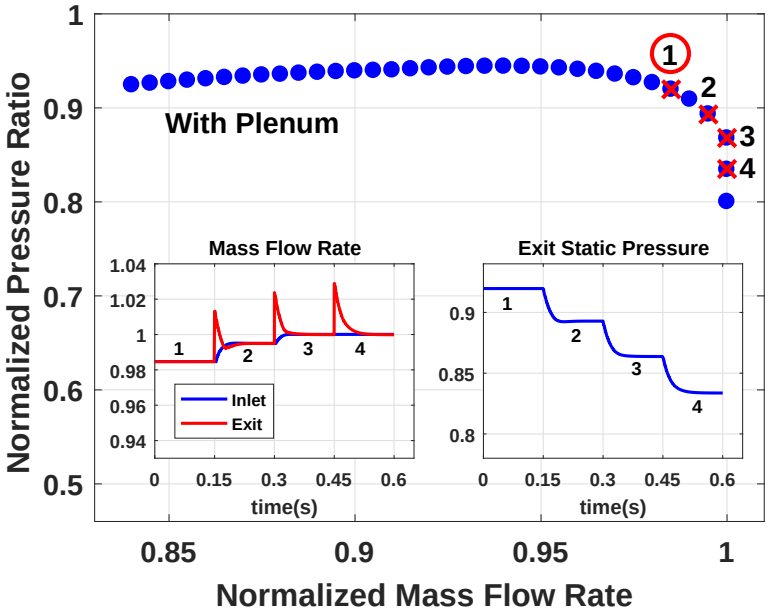

Figure 5.2: Mass flow rate and exit static pressure response at 100% speed for operating points 1 to 4 with a real end plenum

of flow variables and throttle opening are subsequently used as the initial conditions for the time marching scheme. After an initial settling time in which any small deviations from the calculated steady state are settled, the throttle is switched to a 3% area increase followed by another settling period. This process is repeated three times. Points 1 and 2 are on part of the characteristic in which the flow is not choked at any location along the compressor. Points 3 and 4 are on the choked branch where one or more stages experience choking conditions. The time traces of the mass flow rate at the inlet and exit show that upon each throttle change, the mass flow rate at the throttle surges up and subsequently settles down, whereas the flow rate at the inlet grows gradually, eventually matching the flow rate at the exit. At the switch between point 3 and point 4, flow rate at the inlet experiences no change and the flow rate at the exit overshoots initially, but eventually settles to the flow rate of the previous throttle setting.

Following the same process with a lumped plenum, Figure 5.3 illustrates the three throttle switches with area change of 3% after each settling period. Clearly in comparison to

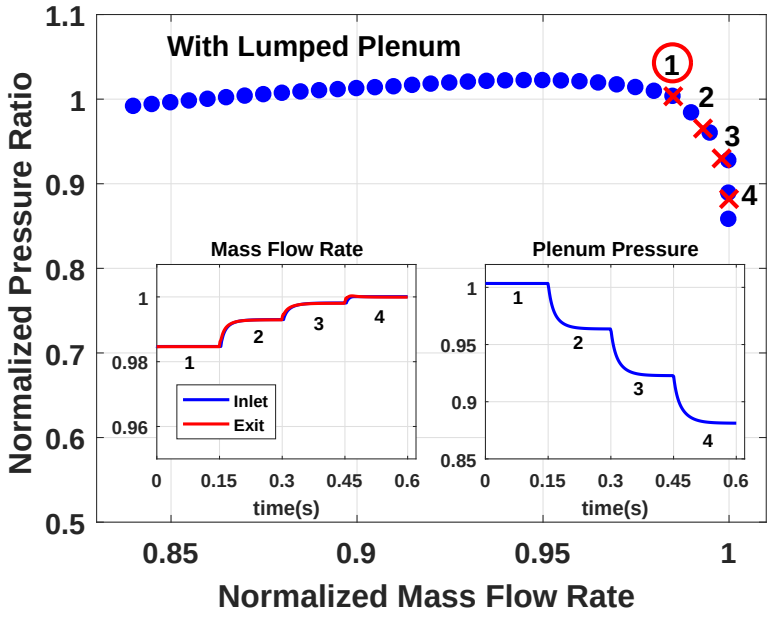

Figure 5.3: Mass flow rate and plenum pressure response for operating points 1 to 4 with a lumped plenum

the real plenum, the response is much faster with inlet flow rate closely following the exit flow rate. There is hardly any overshoot except in the case of last switch when the choking happens, and a very small overshooting occurs. In contrast to the real plenum case, second throttle switch, in this case, does not choke the compressor, but settles to just below the choked flow rate. Since the lumped plenum suppresses the wave interaction phenomena, for all the subsequent simulations in this chapter (unless mentioned specifically), the plenum is included as a real geometric component with prescribed volume and length. Note that due to the large plenum to compressor exit area ratio, the incurred losses are higher in a real plenum, thus leads to lower pressure ratios.

Let us now look into the details of the wave structure in the plenum and compressor section for the dynamic simulation results shown in Figure 5.2. The area ratio of the plenum to compressor exit is about 13:1, large enough to represent a near solid wall for waves impinging from the plenum side and an open end for the waves impinging from the compressor side. Also, the choked throttle at the plenum exit is nearly a solid termination

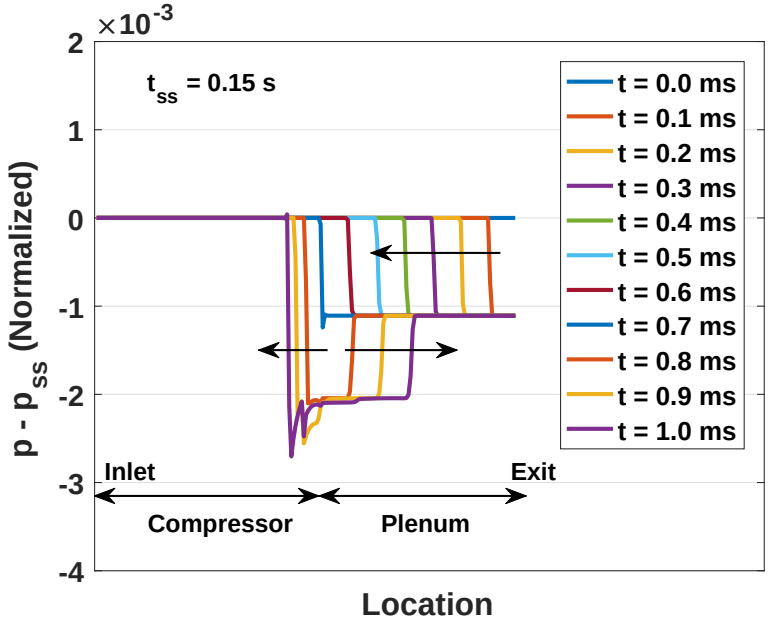

Figure 5.4: Time snapshots of wave front from 0-1 ms evaluated from the previous steady state ($t_{ss} = 0.15$ s)

for the impinging waves. The low Mach number and length of the plenum imply that about 2/3 of a millisecond is needed for a wave moving at the speed of sound to traverse the plenum in each direction. However, once the wave enters the compressor from the back, it is significantly slowed down by the opposing mean flow velocity in the compressor passages. As a result, it takes about 4 ms for the wave to traverse the distance from the throttle to inlet.

To be able to follow the relatively small variations in the pressure and flow rate which follow this throttle switch, incremental differences from the previous steady state are shown. Accordingly in the following figure, at $t = 0$ ms, the pressure and flow rate are uniformly zero across the compressor. Figure 5.4 shows the wave formation dynamics for the first millisecond after the throttle is stepped from point 1 to point 2 as depicted in Figure 5.2. It shows a steep expansion wave moving from the throttle to the left and reaching the interface with the compressor in about 0.75 ms. The impinging expansion wave is partially reflected as an expansion wave and partially transmitted into the compressor. Because of the high area ratio, the reflection is almost full as evident by the near doubling of the amplitude of the reflected wave. It should be noted that the transmitted pressure wave has essentially the same amplitude as the reflected wave.

Figure 5.5 shows lower time resolution snapshots of the spatial distribution of the flow rate and static pressure following the throttle switch from point 1 to point 2. As already shown for one millisecond after the switch, the red line corresponding to $t = 1$ ms shows that the expansion wave which originated at the throttle opening and caused a rush of flow at the exit has moved through the plenum into the compressor and has partially reflected as an expansion wave that has further traveled half way through the plenum back towards the throttle. One millisecond later at $t = 2$ ms, this expansion wave has already impinged on the throttle side and has gotten reflected also as an expansion wave, almost reaching the compressor-plenum interface, shown as the green line. Meanwhile, the initial wave inside the compressor keeps propagating towards the inlet, also shown as the green line. At $t = 3$ ms, the wave front has impinged on the interface, moved back as an expansion wave and

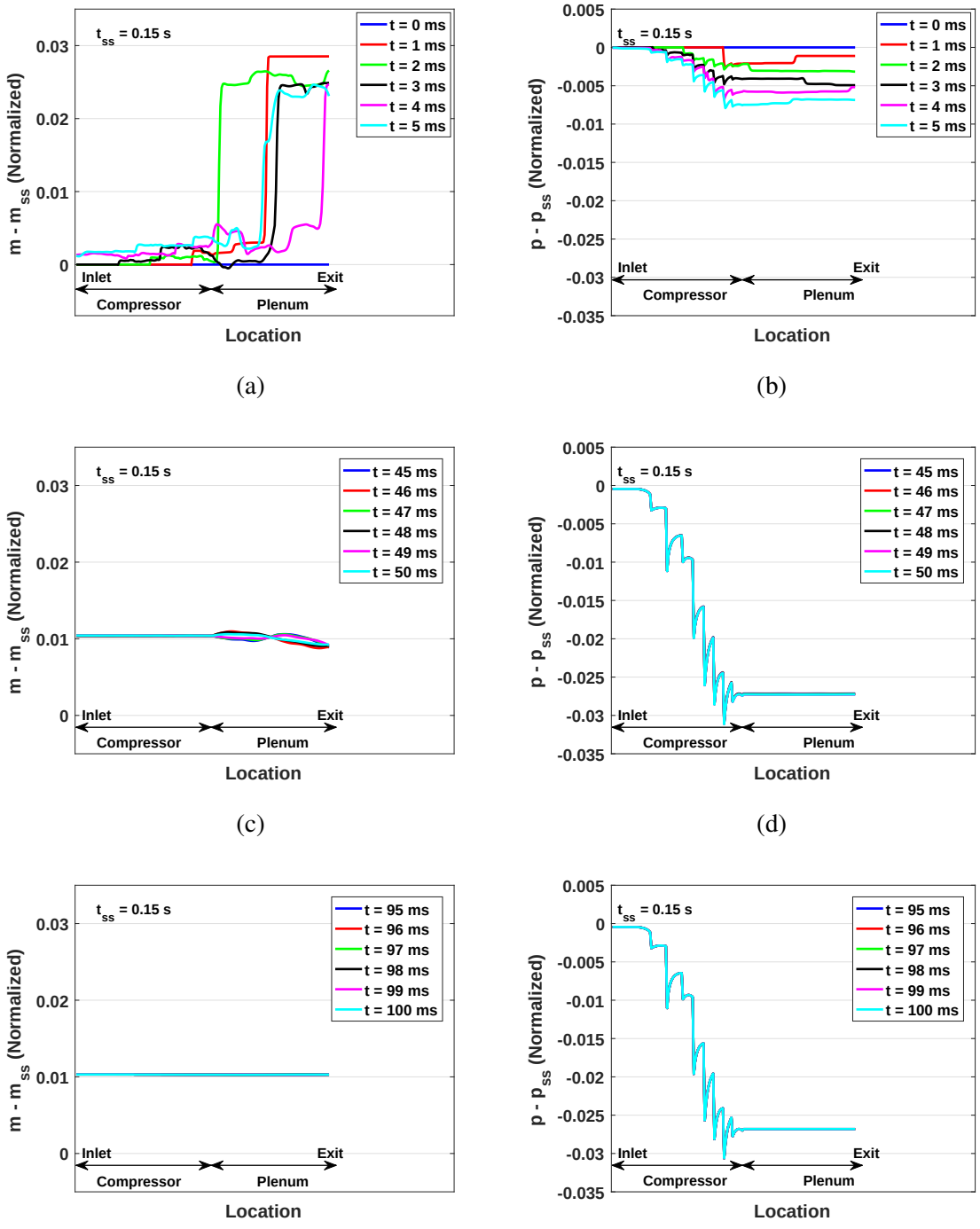

Figure 5.5: Mass flow rate and pressure deviation corresponding to Figure 5.2 evaluated from the steady state ($t_{ss} = 0.15$ s). Wavefront transmission and reflection occur at the compressor-plenum interface.

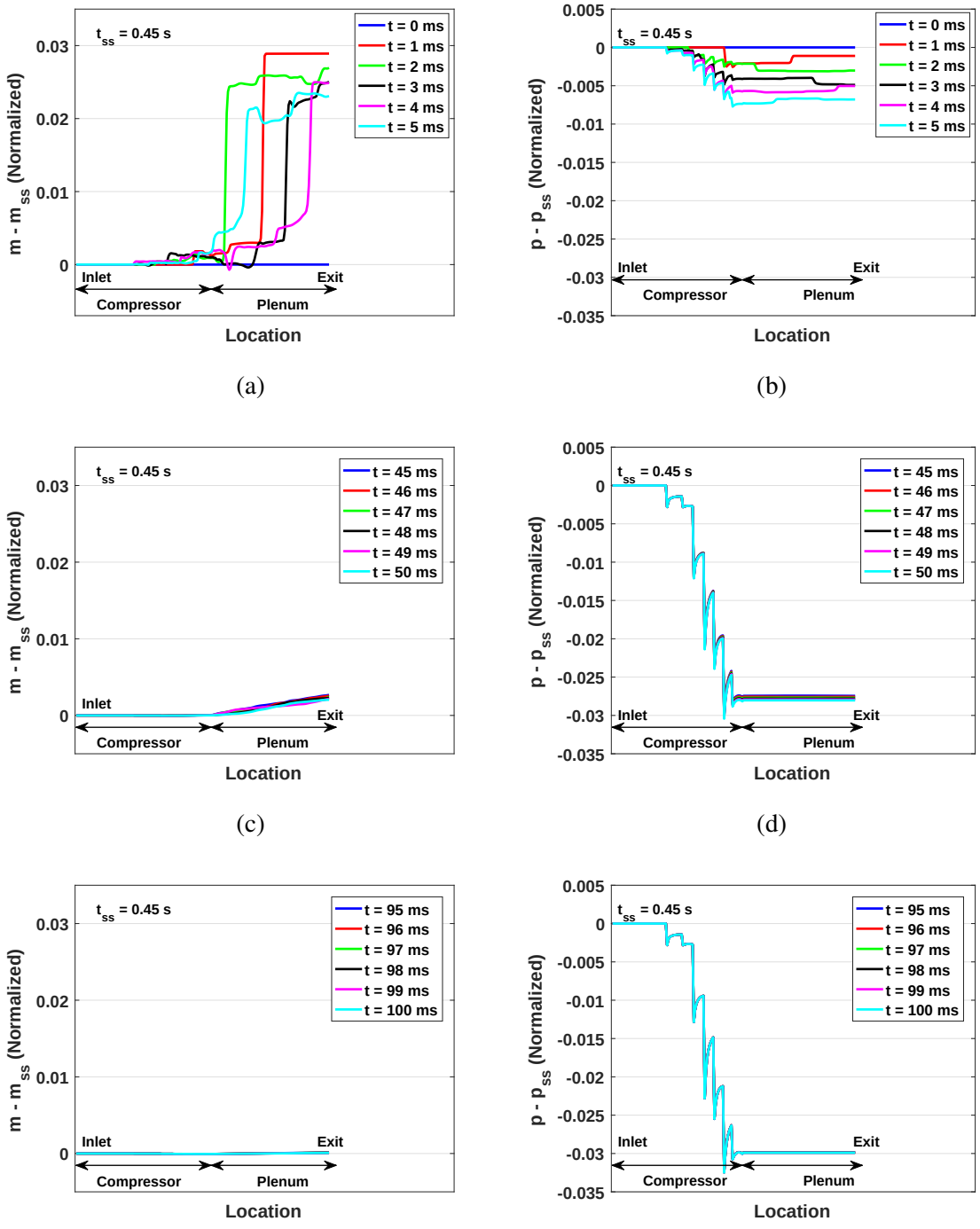

Figure 5.6: Mass flow rate and pressure deviation corresponding to Figure 5.2 evaluated from the steady state ($t_{ss} = 0.45$ s). Inlet remains unperturbed due to the choking of front part of the compressor (stator 1).

reflected back from the throttle side, again propagating into the plenum as an expansion wave, the front of which is evident as the black line nearing the middle of the plenum. By $t = 4$ ms, the front of the black line has impinged on the compressor interface, traveled back and is just about to impinge on the throttle side, shown as the magenta line. This process continues with ever so diminishing wave amplitude, which gradually decreases the plenum pressure. While the waves are bouncing inside the plenum, they are of course affecting the flow in the compressor too. By looking at the flow rate and pressure variations in the compressor, it can be seen that at $t = 3$ ms (black line) the front of the initial wave has not yet reached the inlet. By $t = 4$ ms, the wave front has reached the inlet as evident by the change in flow rate at the inlet (magenta line). The interval of 45-50 ms shows that the compressor has nearly settled at the new operating condition, except inside the plenum as seen through the small deviations in the flow rate. Interestingly, it can be seen that the wave formation in the plenum assumes the fundamental longitudinal mode. In the interval of 95-100 ms, all plots have been converged as the compressor has reached the new steady state. The scenario following the switch from point 3 to point 4 is shown in Figure 5.6, and is very similar to the switch between point 1 and point 2 discussed above. But it can be seen here that the front half of the compressor experiences no change in pressure and mass flow rate, indicating the location of the choked point to be the inlet to stator 1.

5.1.2 Compressor Stability Loss with Plenum

Let us now turn attention to the throttling schedule shown in Figure 5.7. In this run, the mass flow rate decreases as the throttle is closed in steps and the pressure increases until in the last step, the compressor loses stability resulting in an escalating drop in the pressure and flow rate. Figure 5.8 shows the high resolution time snapshots of the pressure wave structure in the first 1 ms after the throttle step from point 1 to point 2. It is similar to the previous scenario of throttle opening, except for the fact that the waves are now compression rather than the expansion waves.

Figure 5.9 shows the corresponding snapshots of the waves during the first 5 ms following the switch from point 1 to point 2. The scenario is very similar to the choking process discussed above, hence has been left to the reader to follow the back and forth motion of the waves. Also similar to the response of throttle opening, at the end of the first 5 ms, flow through the plenum is still vastly different from the flow through the compressor. However, it could be understood that 100 ms later, the flow through the plenum will perfectly match to that of the compressor, figures not shown for the sake of brevity.

Let us now turn to analyze the critical switch between points 3 and 4 that ends ultimately with the loss of compressor stability. The behavior in the first five milliseconds, shown at the top of Figure 5.10, is very similar to that after switching from point 1 to point 2. However, $t = 5$ ms trace (cyan line) of the flow rate shows that flow through the compressor is dropping at an accelerated rate in comparison to the first switch. Plots of the traces between 6-11 milliseconds as shown in Figure 5.10, confirm that the flow through the compressor is indeed dropping in increasing fashion, even if the pressure ratio is still

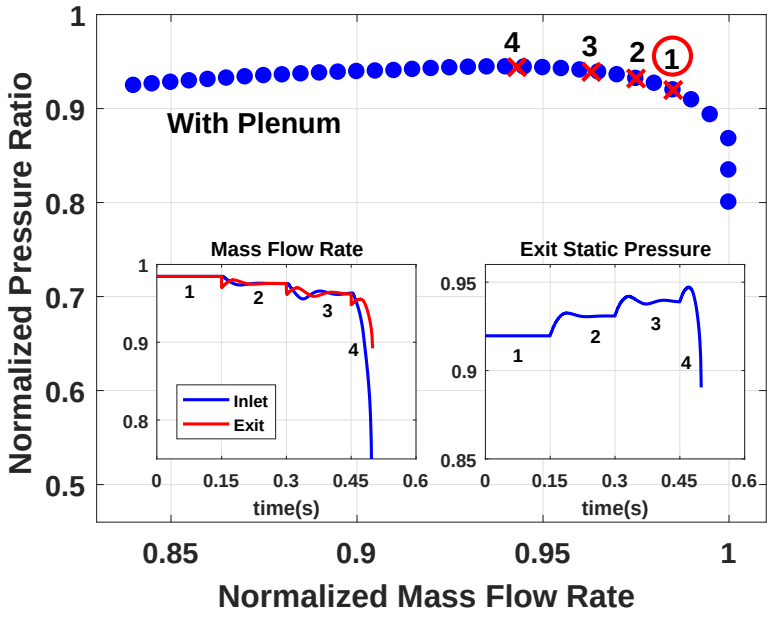

Figure 5.7: Mass flow rate and exit static pressure response at 100% speed for operating points 1 to 4 showing loss of stability close to the peak pressure with real end plenum

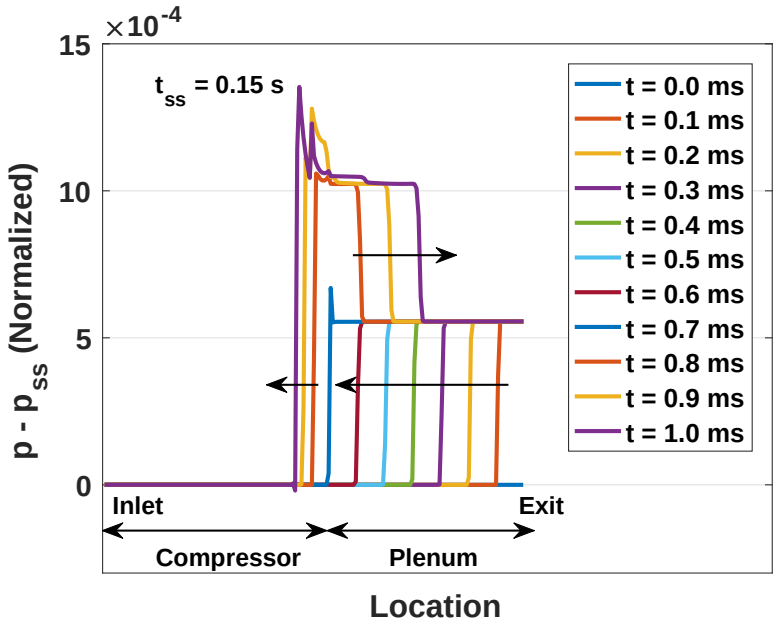

Figure 5.8: Time snapshots of wave front from 0-1 ms evaluated from the previous steady state ($t_{ss} = 0.15$ s)

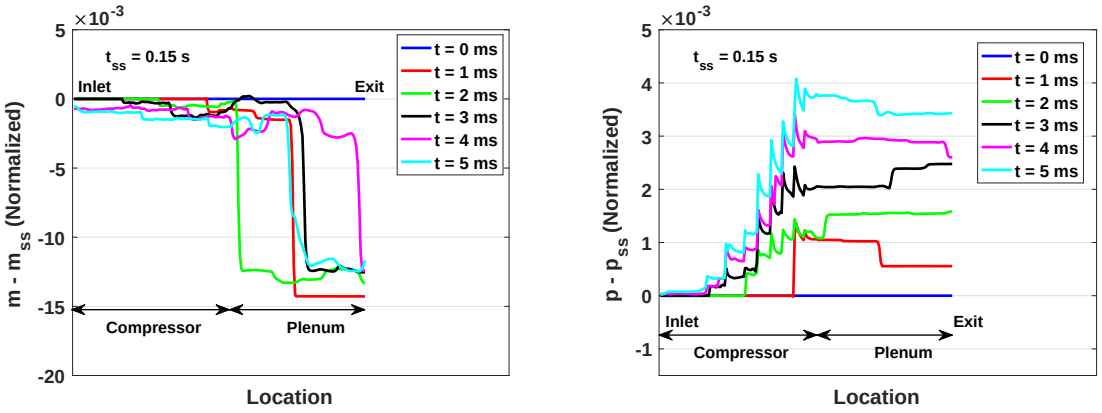

(a) (b)

Figure 5.9: Mass flow rate and pressure deviation corresponding to Figure 5.7 evaluated from the steady state ($t_{ss} = 0.15$ s) showing the propagation of compression wave and reflections from the compressor-plenum interface

increasing across the compressor. This divergence ultimately leads to a flow reversal at $t = 49.5$ ms corresponding to the surge. It is important to notice that the gradual flow divergence in the first 10 ms is manifested almost uniformly along the compressor, thus indicating that flow in the compressor responds mostly as bulk. This suggests that the wave

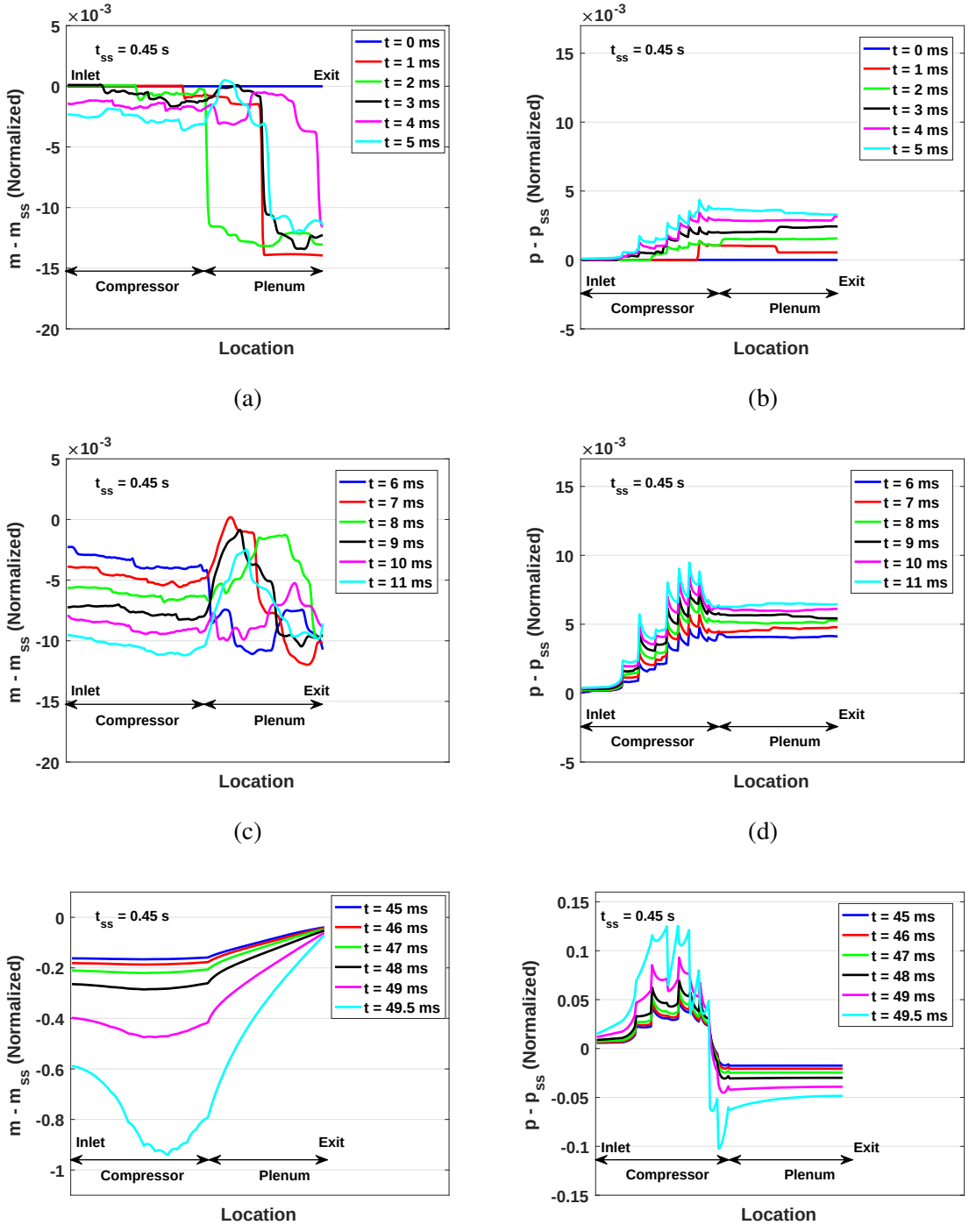

Figure 5.10: Mass flow rate and pressure deviation corresponding to Figure 5.7 evaluated from the steady state ($t_{ss} = 0.45$ s) showing sudden drop in mass flow rate and compressor pressure

motion across the compressor has little to do with the mechanism that is responsible for this divergence. In essence, the behavior of the system follows more or less like the compressor dynamics described by Greitzer's model [1, 2]. Accordingly, the loss of stability that occurs once the overall characteristic of the compressor is near its peak is associated with the B-parameter which increases with the plenum volume. Thus, one might expect that the dynamics of the compressor will be significantly altered if the plenum is eliminated and a throttle is attached at the exit of the last stator or in its vicinity.

5.1.3 Compressor Stability Loss without Plenum

The behavior of the compressor without a plenum is shown in Figure 5.11 for a sequence of step closings of the throttle along the marked points. In this configuration, the compressor successfully operates at point 3 which is beyond the peak as is evident in the pressure time trace showing that at the throttle setting 3, the pressure is lower than that at the throttle setting 2. Moving yet further to the left results in oscillations that ultimately reach limit

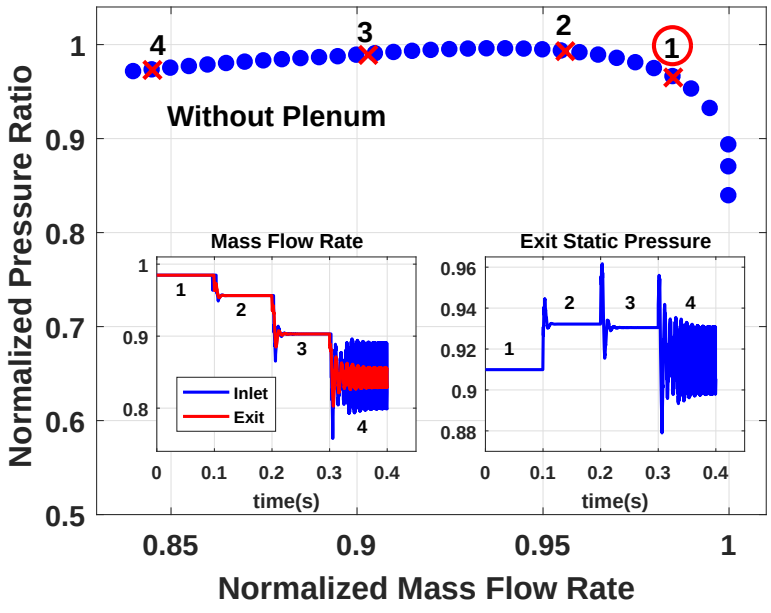

Figure 5.11: Mass flow rate and exit static pressure response at 100% speed for operating points 1 to 4 without end plenum

cycle of about 4% peak-to-peak amplitude near the throttle end. The oscillations have two distinct frequencies, a low frequency near 100 Hz and a high frequency of about 4 kHz. These oscillations are addressed in the next section, but first a comparison is done between the transitions to the steady points obtained with and without the plenum.

Comparing the time traces in Figure 5.11 to those in Figure 5.7, it can be seen that without the plenum, the time response to the step change in the throttle is much shorter. After further examining the pressure traces, overshoot with faster settling can be seen compared to the slower and much less overshooting monotonic convergence that occurs when the plenum is connected. Examining the mass flow rate and pressure variation distributions after the first switch as shown in Figure 5.12, the progression of the initial front can be followed, shown as the red line at $t = 1$ ms, the green line at $t = 2$ ms and the black line at $t = 3$ ms that is about to impinge on the inlet. Analysis of the pressure past this point is difficult because the sharp stationary jumps at the interfaces obscure the more subtle pressure wave fronts propagating back and forth along the compressor. On the other hand, the flow rate distribution variation is much easier to contemplate because the flow rate is continuous, and therefore, there are no jumps across the interfaces. It is thus easier to follow the wave propagation in the flow rate snapshots. Particularly, the black line shows the distribution of the compression front just before it gets reflected as an expansion wave from the inlet. Note that the left moving compression wave has high pressure at the back, (which is the right side of the front) and low pressure upstream (in the left side of the front), and so it enables flow from right to left. Thus combined with mean flow to the right, the effect of the compression front is to reduce the flow rate in the wake of the propagating front. The reflected expansion wave that moves from left to right having low pressure in the left of the front and high pressure ahead is likewise enabling flow from right to left, further lowering the flow rate in the wake of the front. Since the speed of the front from left to right is about three times more than the speed from right to left, a 1 ms interval cannot catch a good snapshot of the front of the expansion wave.

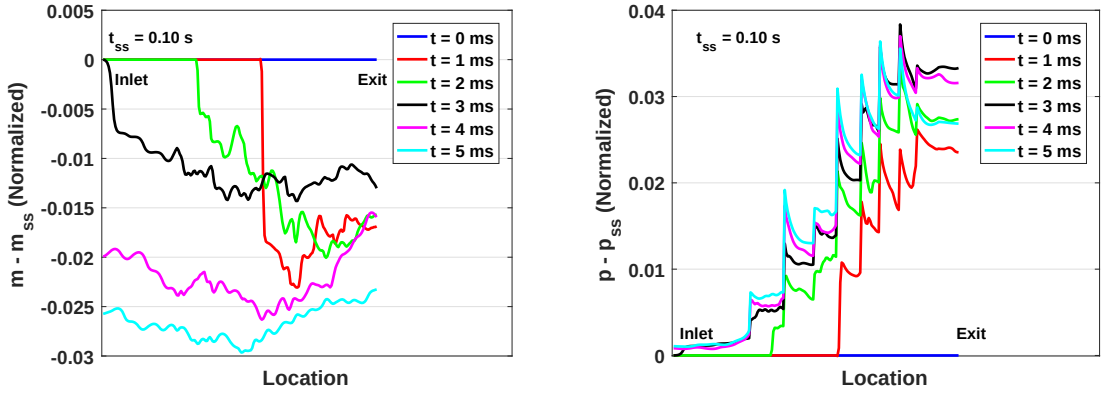

(a) (b)

Figure 5.12: Mass flow rate and pressure deviation corresponding to Figure 5.11 evaluated from the steady state ($t_{ss} = 0.1$ s) showing the propagation of compression front

To get the propagation of the reflected wave, ten snapshots have been made between the 3 ms and 4 ms interval, as shown in Figure 5.13. As can be seen, the propagation of front of the expansion wave is clearly detected in the flow rate snapshots and is all but unobservable in the background of the stationary structures of the pressure distribution. It is worth noting that this front of the flow rate loses its sharpness by the time it gets reflected from the throttle and moves to the left, shown as the cyan line at $t = 5$ ms in Figure 5.12. In comparison, the structure of the flow fronts during the 5 ms interval inside the plenum shown in Figure 5.8

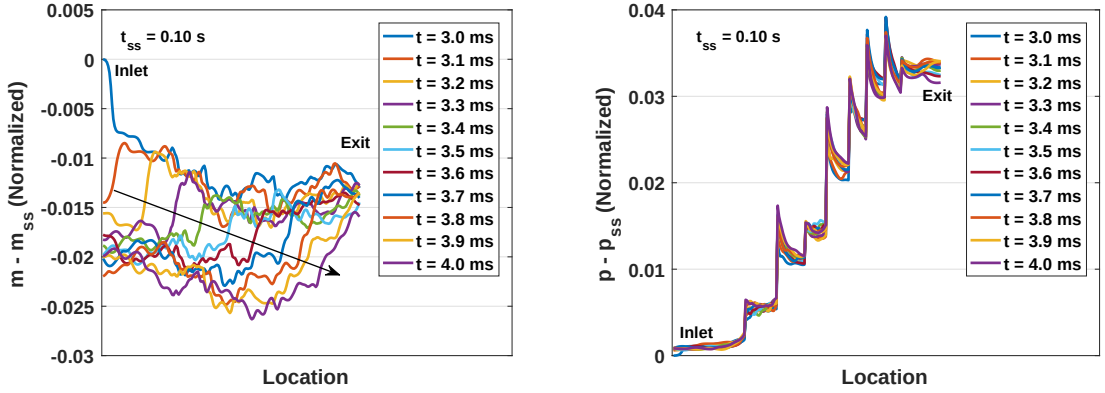

(a) (b)

Figure 5.13: Mass flow rate and pressure deviation in time interval of 3-4 ms evaluated from the steady state ($t_{ss} = 0.1$ s) showing the reflection from compressor inlet

and Figure 5.9, keep their sharpness with no apparent deterioration. The deterioration of the wave fronts in the compressor is because of the dissipative impedance of the interfaces between the rotors and stators.

5.1.4 A Brief Discussion about High Frequency Oscillations

This section is dedicated to address the high frequency oscillations of about 4 kHz that dominate the limit cycle shown in Figure 5.11. The period of the oscillations of about 0.25 ms is about three orders of magnitude longer than the 0.2 microsecond time step of the simulation program, thus suggesting that these oscillations are not due to the numerical artifacts. To get an idea about the spatial distribution of the amplitude of the high frequency mode, first a high pass filter is applied to the pressure distribution, then the absolute value of filter output is taken, and further, the result is passed through an appropriate low pass filter. The final output at t = 0.4 s is shown in Figure 5.14. In the inlet duct, the amplitude distribution assumes the classical shape of standing wave in a cavity without sources. At some interfaces, the mode experiences sharp change in its shape, with most noticeable are

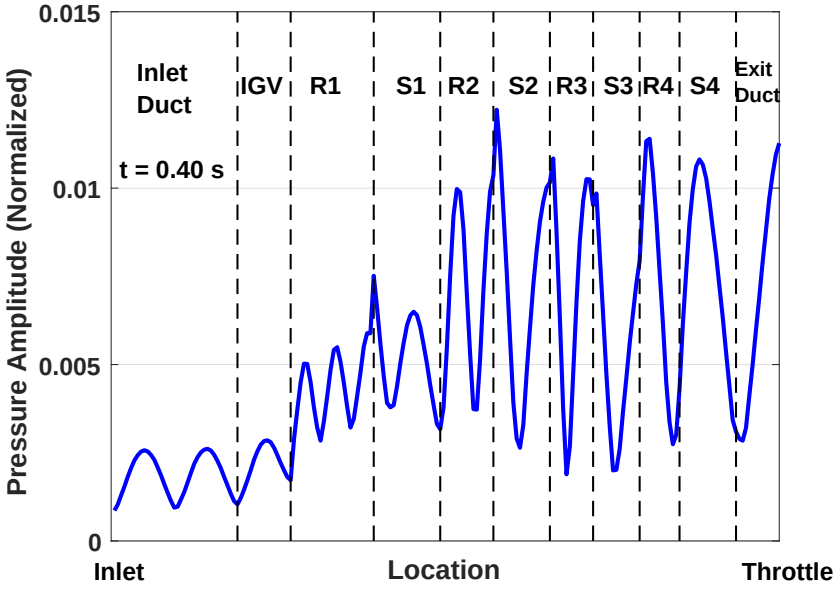

Figure 5.14: Spatial distribution of the amplitude of high frequency mode

the interfaces R1-S1 and R2-S2.

Such variations suggest that it is the source of oscillating energy which provides driving or damping at the interfaces. According to Rayleigh's criterion, which is widely used in thermoacoustics [72], pressure oscillations are maximally amplified/attenuated when heat addition is in phase/out of phase with the pressure oscillations. In the compressor, there is no heat addition from external source, rather there is kinetic energy addition due to the rotation. Therefore, it is interesting to examine the addition of kinetic energy in the compressor. The addition of the kinetic energy per second from the shaft is given by

$$\Delta E_{ke,shaft} = (U^2 - 2UV_e\sin(\beta_e))\dot{m}_e \tag{5.1}$$

where U is the shaft circumferential velocity and the subscript e denotes the velocity and mass flow rate at the row exit. Figure 5.15 shows the shaft power contribution at the various interfaces as the throttle is switched along the points 1 to 4 as shown in Figure 5.11. It is worth noting that the shaft power addition at the exit of the rotors such as R2-S2 and R3-S3

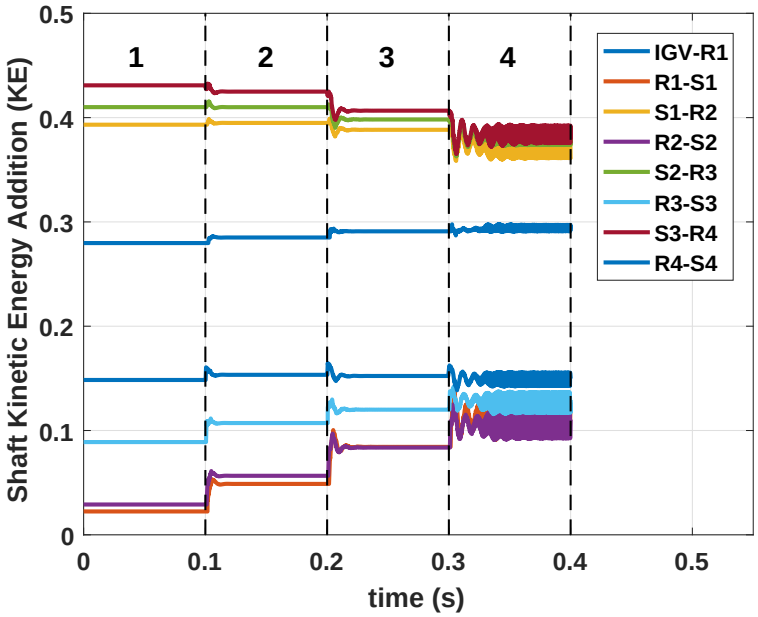

Figure 5.15: Shaft kinetic power addition provided at the rotor-stator interfaces for the throttling process shown in Figure 5.11

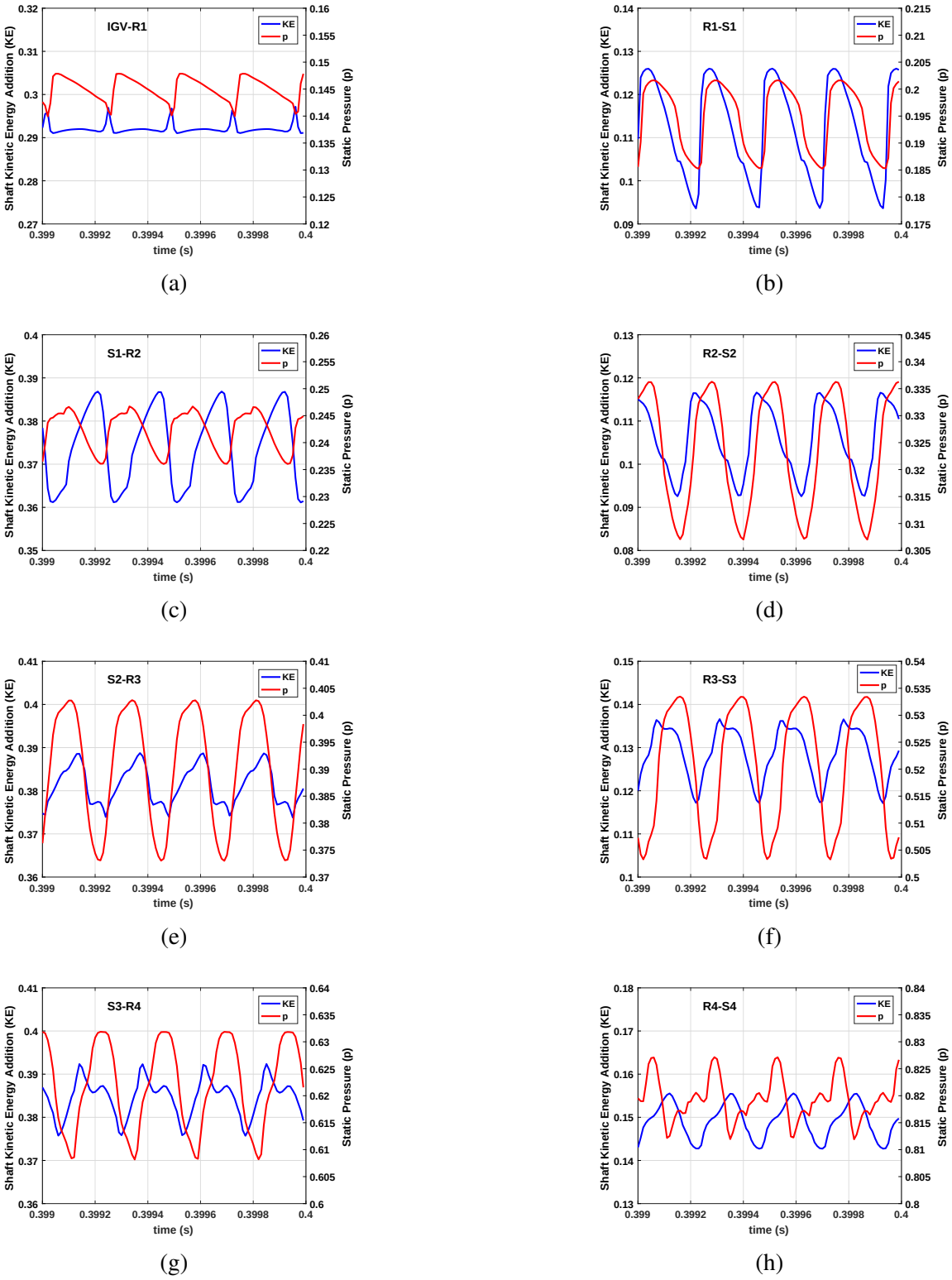

Figure 5.16: Oscillating pressure and shaft power addition at the compact interfaces along the compressor

is much less than that at the exit of corresponding stators such as S2-R3 and S3-R4. This seems to be the result of conservative diffusion load in the rotors that dictates relatively high angle β_e at the rotor discharge; tangential component of the velocity negates the addition of rotating velocity and thus reduces the addition of shaft power.

Figure 5.16 shows the pressure and shaft power addition at the various interfaces for the last millisecond of throttle switch 4, see Figure 5.11. It can be seen that the interfaces R1-S1 and R2-S2 have high pressure amplitude and high shaft power amplitude that are in supporting phases. This is the reason behind the sharp increase in the mode amplitude at these interfaces as seen in Figure 5.14. On the other hand, at the S1-R2 interface, oscillations of both pressure and shaft power are smaller and close to 90 degrees phase apart, thus implying no amplification/suppression as per Rayleigh's criterion. This is corroborated by the smooth transition of the mode through this interface as shown in Figure 5.14.

The above discussion of the driving mechanism of the pressure oscillations brings to the conclusion that all oscillations, including and particularly those associated with the rotating stall, should obey the same physics. Overall, they are impacted by the phase between the static pressure and shaft power addition. The fact that the rotating stall has a non-uniform circumferential distribution does not play any role in determining the growth or decay of the oscillations, as for a fixed point on the circumference, the velocity oscillations and the corresponding shaft power response are related in exactly the same way as if the oscillations are axisymmetric.

5.1.5 Loss of Stability at a Low-Speed

After investigating the compressor stability loss at the nominal speed, this section is focused on stability loss of axial compressor at a low-speed (70% RPM). Figure 5.17 demonstrates the unsteady response as the throttle is closed in successive progressions by 4% during each switch. Starting from point 1 which is a stable point, throttle closure leads to point 2 which also settles to a stable state. Further step on throttle results in point 3 which lies

close to the peak of constant speed characteristic. At point 3, the unsteady response contains both the high and low frequency oscillations as described earlier. Although this point is stable, subsequent closing of the throttle causes a sudden drop in the mass flow rate and exit pressure, thus pushes the compressor into surge.

In this run, the plenum has been used as a real geometric component. In comparison to the nominal speed case, shown in Figure 5.7, this case shows both the high and low frequency modes before stall, mostly due to reduced B-parameter value. It is to be noted that these modes were actually absent before stall in the nominal speed simulation with plenum, and were seen only in the no plenum simulation (Figure 5.11), i.e., with the reduced B-parameter. After the second switch, the unsteady flow response depicts the low frequency mode to be decaying, but the appearance of high frequency mode makes these oscillations diverge. Nevertheless, a clear drop in pressure and mass flow rate is observed after the last switch as the operating point crosses the peak of compressor characteristic.

The progression of compression waves upon first throttle switch is illustrated in Figure

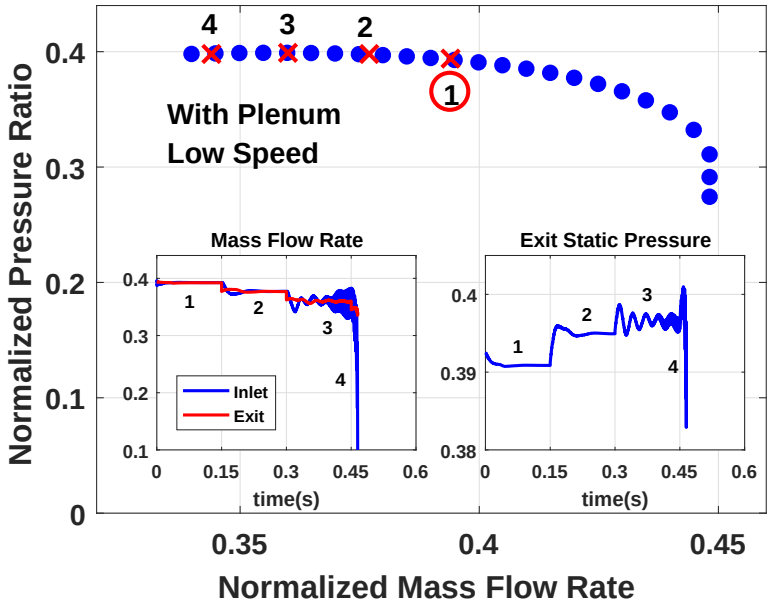

Figure 5.17: Mass flow rate and exit static pressure response at 70% speed for operating points 1 to 4 with a real plenum

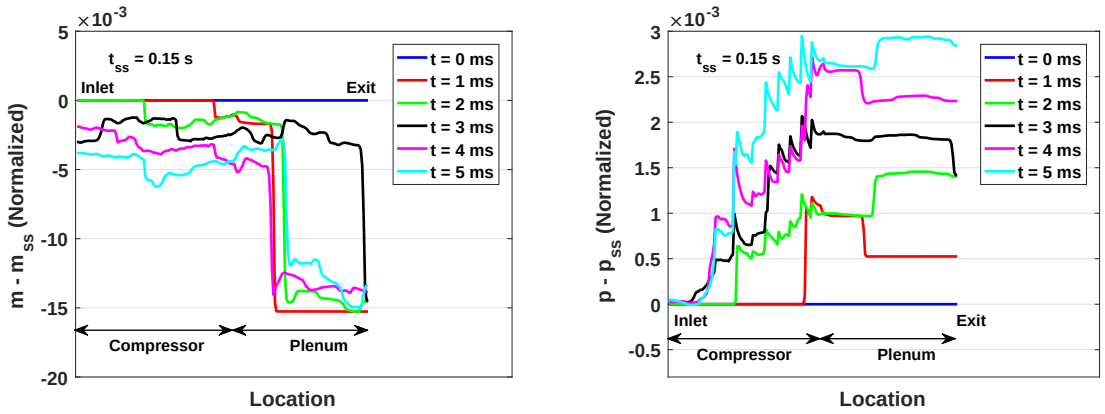

(a) (b)

Figure 5.18: Mass flow rate and pressure deviation at low-speed corresponding to Figure 5.17 evaluated from the steady state ($t_{ss} = 0.15$ s)

5.18. A quick comparison of the first five milliseconds with the nominal speed case (i.e., Figure 5.9) shows that the compression wave initiating at the plenum exit reaches the inlet in less than 3 ms. This is slightly lower than the nominal speed case where the compression front took around 4 ms to reach the inlet. This is due to the lower velocity of the oncoming flow, hence wave travelling with effective velocity of $V - c$ takes less time to travel upstream. Furthermore, the back and forth progression of compression wave can be seen in this case also and is quite similar to the nominal speed case.

5.2 Unsteady Simulation of Axial-Centrifugal Compressor

After discussing the axial compressor unsteady results, this section focuses on simulation of the axial-centrifugal compressor, nominal configuration of which can be seen in Figure 4.1. In order to investigate the behavior of the compressor deep into the stall branch, as has been done in the case of the axial compressor, compact throttle is applied after the 90 degree bend, also shown in Figure 4.1. Starting at just below the choked flow rate at 100% speed, the high frequency oscillations develop even at operating points which lies on the right side of the peak. Moreover, moving further into the choked branch does not affect the generation of these oscillations as seen through the unsteady simulation in Figure 5.19. These oscillations

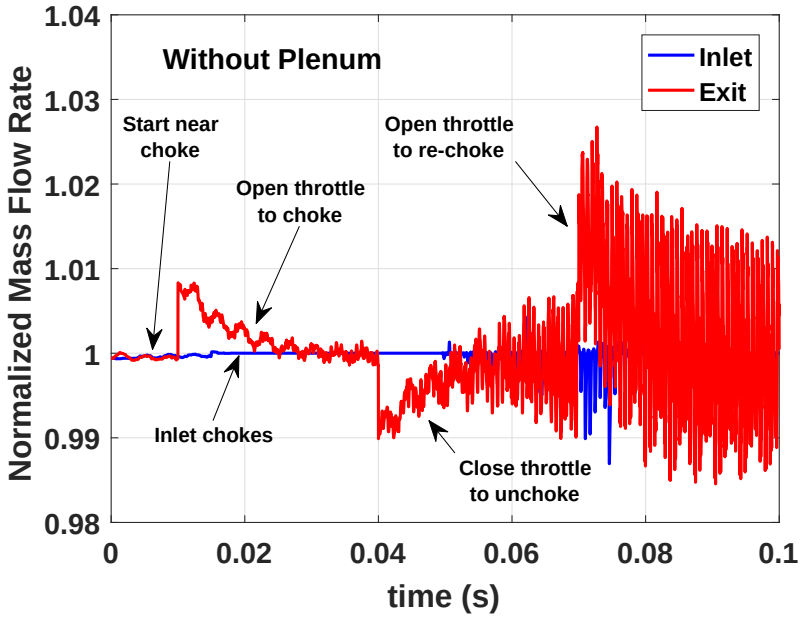

Figure 5.19: Presence of high frequency oscillations when the axial-centrifugal compressor is operating near and in choked conditions

are similar in nature to those observed during the axial compressor response without plenum, see Figure 5.11. It is, however, to be noted that the high frequency oscillations in the axial compressor appear only at a point well onto the left side of the characteristic at conditions which are rarely, if at all, encountered during rig tests. It is, therefore, difficult to estimate if such high frequency oscillations would appear during a real compressor operation. However, the high frequency oscillations encountered in the axial-centrifugal compressor, as shown in the Figure 5.19, are at a point well within the expected operating regime of the compressor. Let us now consider the following two questions:

1. Can a high frequency acoustic resonance mode be excited in a real compressor?

2. What is the cause of excitation of the resonance mode in the present 1D model?

The answer to the first question is a yes! Day *et al.* [73] measured high frequency oscillations of around 10-13 times the shaft frequency in two of the four high-speed compressors. Hellmich & Seume [74] noted the following features of acoustic resonances in real machines.

1. They occur as non-synchronous pressure fluctuations at discrete frequencies.

2. The acoustic field in most cases has a helical structure.

3. In most cases, vortex shedding is assumed to be the excitation mechanism driving the resonance.

In addressing the second question above, it is to be recognized that in a complex 3D compressor flow environment, there are a number of factors which can amplify or damp out the resonance modes. In the present mean-line model, these modes are expected to get decayed due to the friction term which is included in the momentum equation. In addition, the dynamic compact interfaces between the blade rows have complex losses which are, in general, non-linear terms and may act to augment or suppress the resonance modes. It should be kept in mind that those terms have inherent empiricism which was introduced to achieve a good correlation with the measured steady state characteristics. For instance, the mixing loss parameter ξ_{ml} was changed from $\xi_{ml} = k$ to $\xi_{ml} = k|\alpha|$ during the second tuning process to correct the slope of the characteristics near the surge line. In the latter form, ξ_{ml} is modulated by the dynamic variations in the incidence angle α. Hence, it is

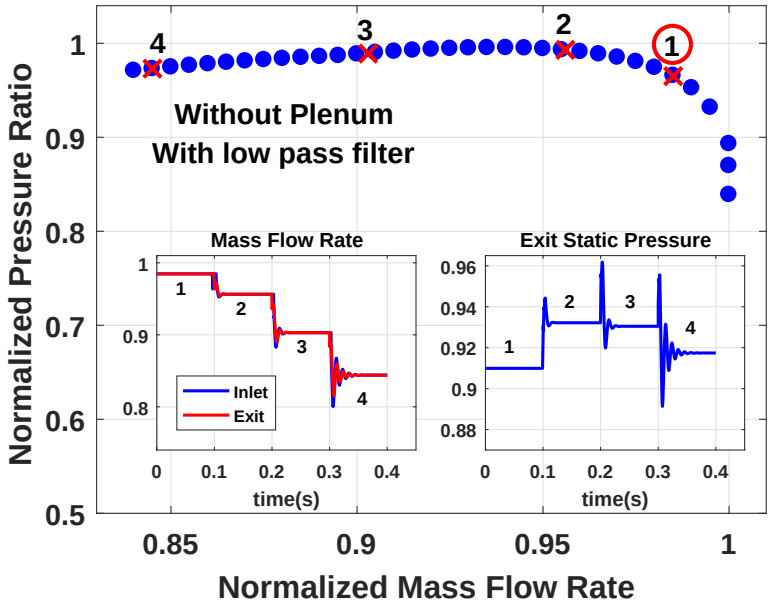

Figure 5.20: Unsteady response of the axial compressor at nominal speed with low pass filtering of the term $k|\alpha|$ with time constant of 1 ms

conceptualized that this kind of term needs to be filtered by a low pass filter in such way so as to minimize the unintended effect upon the dynamic response. Figure 5.20 shows unsteady response of the axial compressor without any plenum along the marked points shown in the Figure 5.11. A low pass filter with time constant of 1 ms is applied to the term $k|\alpha|$. The significant effect is evident in the fast damping of the high frequency oscillations at point 4. It should, however, be noted that the damping of this high frequency mode decreases as more points on the left side are approached. Thus, it is expected that as the compressor is further throttled towards left and the slope of the characteristic steepens, this mode would become unstable.

5.2.1 Comparison between Nominal and Low-Speed Cases

The loss model of the centrifugal stage includes more coupling terms that are highly non-linear and thus are subjected to the low pass filtering. These include Δh_{DF} (equation (2.37)), Δh_{BL} (equation (2.39)) , Δh_{RC} (equation (2.42)) and the vaned diffuser loss (equation (2.48)). Subsequent to the application of filter, results of the throttling schedule at the nominal speed without plenum are shown in Figure 5.21a. Starting from point 1 which lies close to the choked branch, 0.6% closing of the throttle leads to another stable point. Subsequent throttle closure shifts the operating point near to the peak pressure, marked by point 3, which in this case also turns out to be stable. This is in accordance with B-parameter value which gets significantly lowered due to the absence of any end plenum. A further 0.6% closing of the throttle after point 3 destabilizes the compressor, which is associated with the escalating drop in the exit pressure and mass flow rate. An important thing to note is that the inlet flow rate responds very quickly to the throttle changes with highly damped response. Overall, the simulation shows smooth operation on the right side with transition towards stall as the compressor is throttled in steps to the left side. Further, Figure 5.21b confirms that similar to the case of axial compressor, the addition of plenum destabilizes the compressor near to the peak, thus leads to surge.

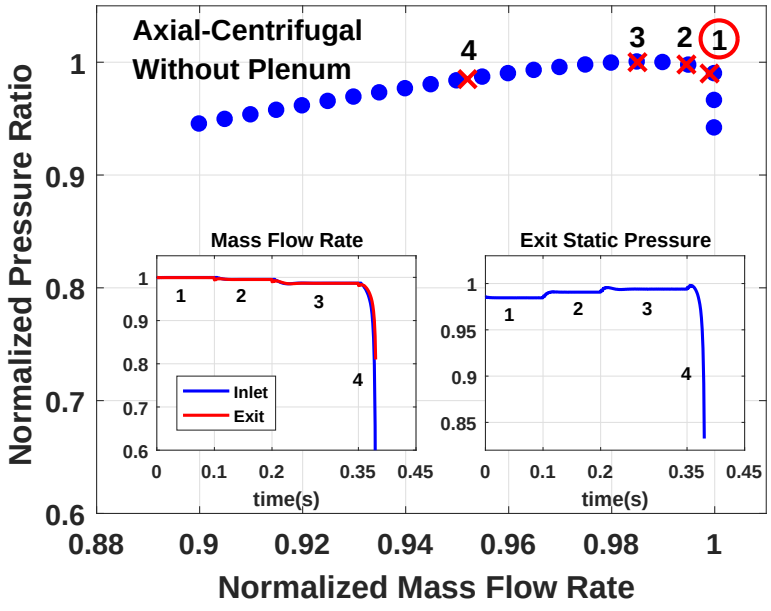

(a)

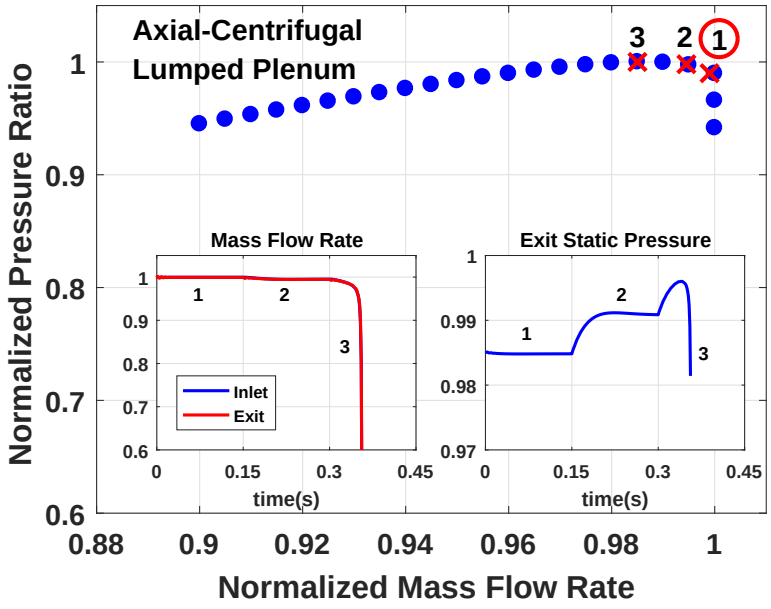

(b)

Figure 5.21: Mass flow rate and pressure response at 100% speed for the axial-centrifugal compressor showing (a) stability loss to the left of the peak without plenum, (b) stability loss near to the peak with lumped plenum

To analyze the last throttle switch which leads to overall compressor instability, pressure and mass flow snapshots, evaluated from the previous steady state ($t = 0.35$ s) corresponding

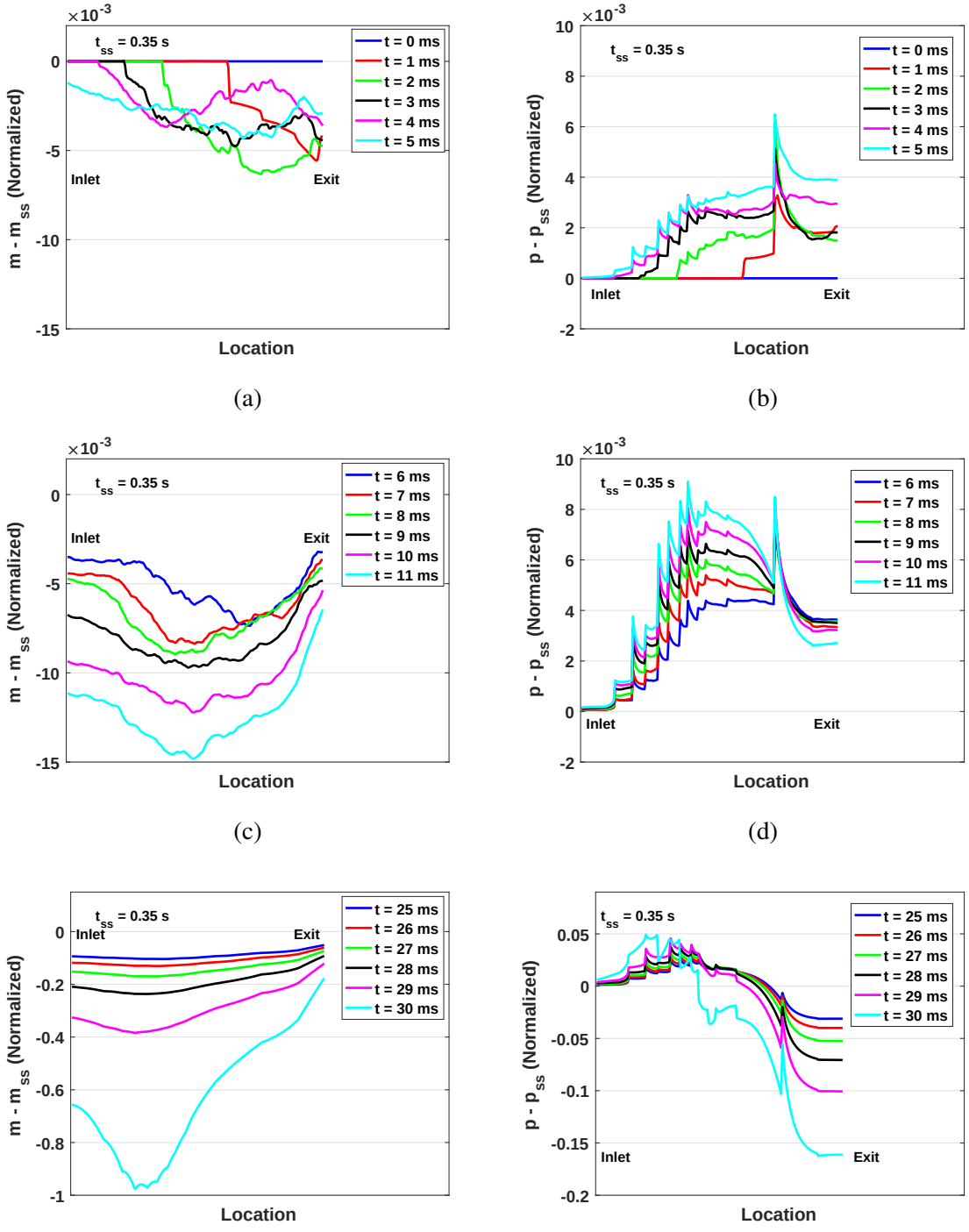

Figure 5.22: Mass flow rate and pressure deviation corresponding to Figure 5.21a evaluated from the steady state ($t_{ss} = 0.35$ s) depicting escalating drop in the flow rate

to Figure 5.21a, are shown in Figure 5.22. As the flow rate plot shows, the compression front that gets initiated due to throttle step travels towards the inlet and reaches there in nearly

5 ms. However, the sharpness of the compression front deteriorates due to the diffusive compact interfaces. Moreover, the sharp discontinuities are clearly visible in the pressure deviation plot, with most significant being the impeller-diffuser interface. During the next 5 ms (6-11 ms), both the flow rate and pressure drop along the compressor while trying to achieve the next operating point on the left side. This sudden drop in the mass flow rate manifests itself almost uniformly across the compressor, leading to the flow reversal at around $t = 30$ ms. Here, the flow reversal first occurs inside one of the axial stages as seen in the figure.

Next, the operation of the axial-centrifugal compressor without plenum at part-speed is studied. It is expected that with reduced B-parameter that accompanies the reduced shaft speed, the compressor should be able to avoid surge at some points to the left of the peak. Figure 5.23 illustrates the throttling process towards stall at the 70% speed. Following the marked points as shown, it can be seen that points 1, 2 and 3 are stable, even though point 3 lies slightly to the left of the peak. Further closing of the throttle by 1.5% leads to point 4

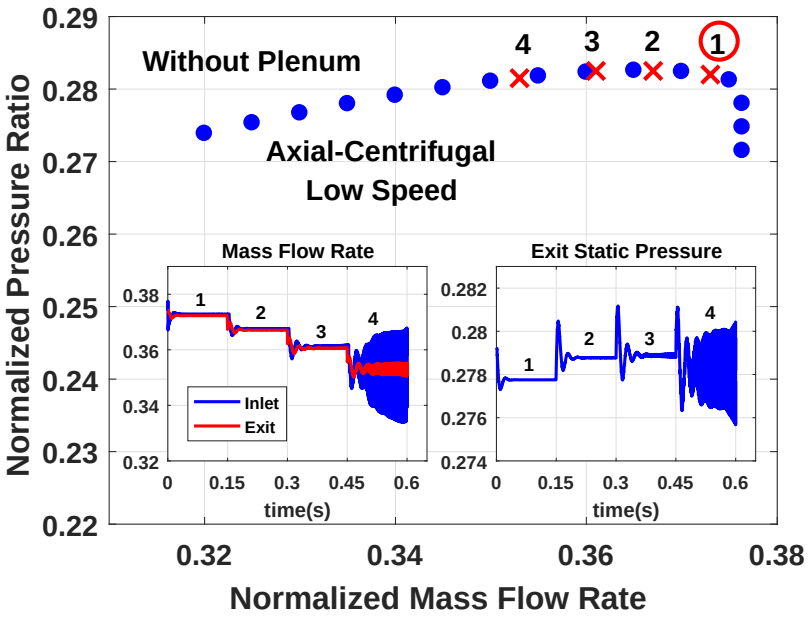

Figure 5.23: Mass flow rate and pressure response at 70% speed for the axial-centrifugal compressor with excitation of high frequency mode

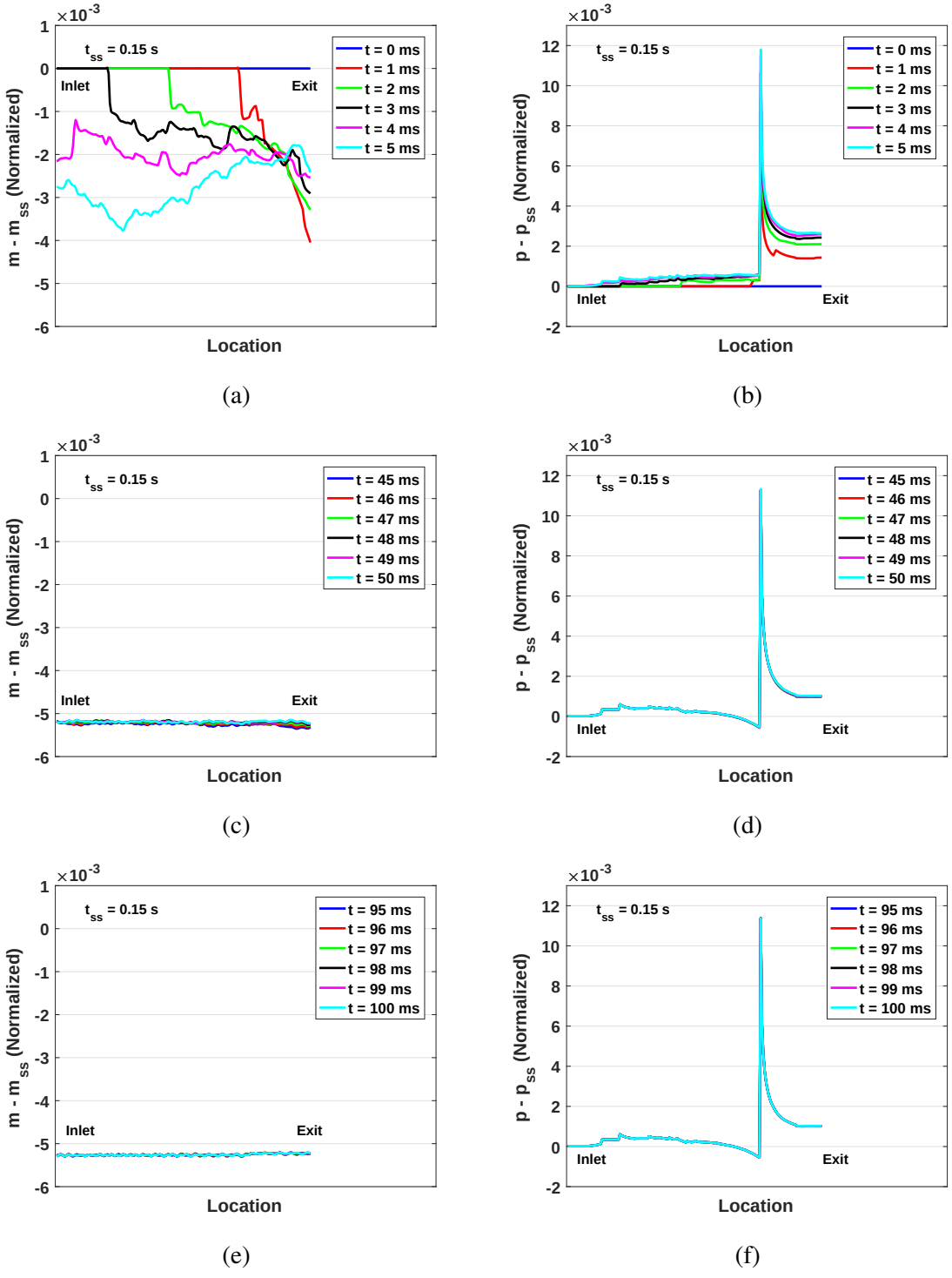

Figure 5.24: Flow rate and pressure deviation at low-speed corresponding to Figure 5.23 evaluated from the previous steady state ($t_{ss} = 0.15$ s)

where the acoustic resonance in the form of high frequency mode gets excited. In this case, the high frequency mode is excited at a point which is not expected to get achieved when a

plenum is coupled to the compressor.

Figure 5.24 shows the wave propagation snapshots after the first throttle switch at $t = 0.15$ s. The compression front that gets originated upon this throttle switch propagates towards the inlet, which now takes around 3.5 ms to travel upstream. A less travel time compared to the nominal speed case is kind of expected due to the lower velocity of the oncoming flow. Similar to the nominal speed case, a sharp peak is clearly visible in the pressure deviation plot at the diffuser inlet. After 100 ms, the new state shows that although the axial compressor results in nearly the same exit pressure as the previous throttle setting, the centrifugal compressor keeps on operating efficiently, thus providing higher overall pressure at point 2 compared to point 1.

5.3 Stability Loss due to Abrupt Stage Collapse

Finally, the effect of stability loss mechanism caused by "collapse" of a stage (i.e., stall of a stage) is investigated. The loss of stability, discussed so far, develops while the slope of the characteristic is still significantly lower than the slope of throttle characteristic. Here, a more radical possibility is discussed where the compressor characteristic slope becomes larger than that of the throttle line as depicted in Figure 5.25. This case leads to much more violent loss of stability and it is referred to as "stall" for the purpose of discussion presented further. The simulated configuration of axial compressor is the same as that discussed earlier (Figure 5.1) with the nominal plenum present at the back of the compressor. Stall is triggered by setting $\xi_{ml} = 1.0$ in equation (2.28) when the angle of attack to the inlet of any of the stages increases above 17 degrees. This abrupt change is supposed to emulate a sudden flow separation that in turn would cause an abrupt change in the compressor response. Figure 5.26 records the pressure and flow distribution snapshots in short intervals before and after the stalling event. The event initiates at 27.5 milliseconds after the last switch when the angle of attack of stator 4 becomes larger than 17 degrees. It can be seen that a large pressure pulse is created just ahead of the inlet to stator 4 and starts to progress forward as a compression

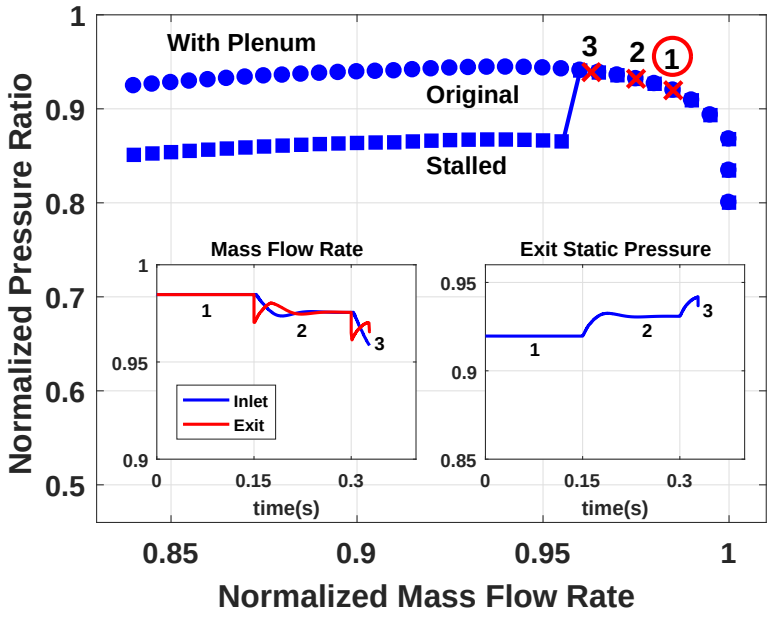

Figure 5.25: Mass flow rate and static pressure response at 100% speed depicting loss of stability to the right of peak pressure when stator 4 crosses the critical/stall angle of attack

front while moving backward as an expansion front as evident by the undershoot of pressure at the back edge of the pulse. Considering that the location of the stall is near the plenum, the expansion wave pressure signature is all but unrecognizable when it travels through the plenum, but is very evident upstream as the compression wave moves forward towards the inlet. Nevertheless, the dramatic influence on the flow rate is evident at both upstream and downstream of the stalling stage as the negative flow pulse progresses fast into the plenum as well as towards the inlet. In such an event, one can expect that a pressure gauge capable of fast enough response will jump in front of the stalling stage and drop down at the back of the stage, thus providing the identification of the stalling stage.

In a more realistic scenario, however, the compressor may first lose stability due to the change of slope of the characteristic as shown in Figure 5.10. During this relatively slow process of about 45 ms, the flow rate through the compressor decreases significantly. Further during this process, the angle of attack to all the stages increase until at one of the stages, it reaches its critical value resulting in the “stall” and thus manifesting itself as a

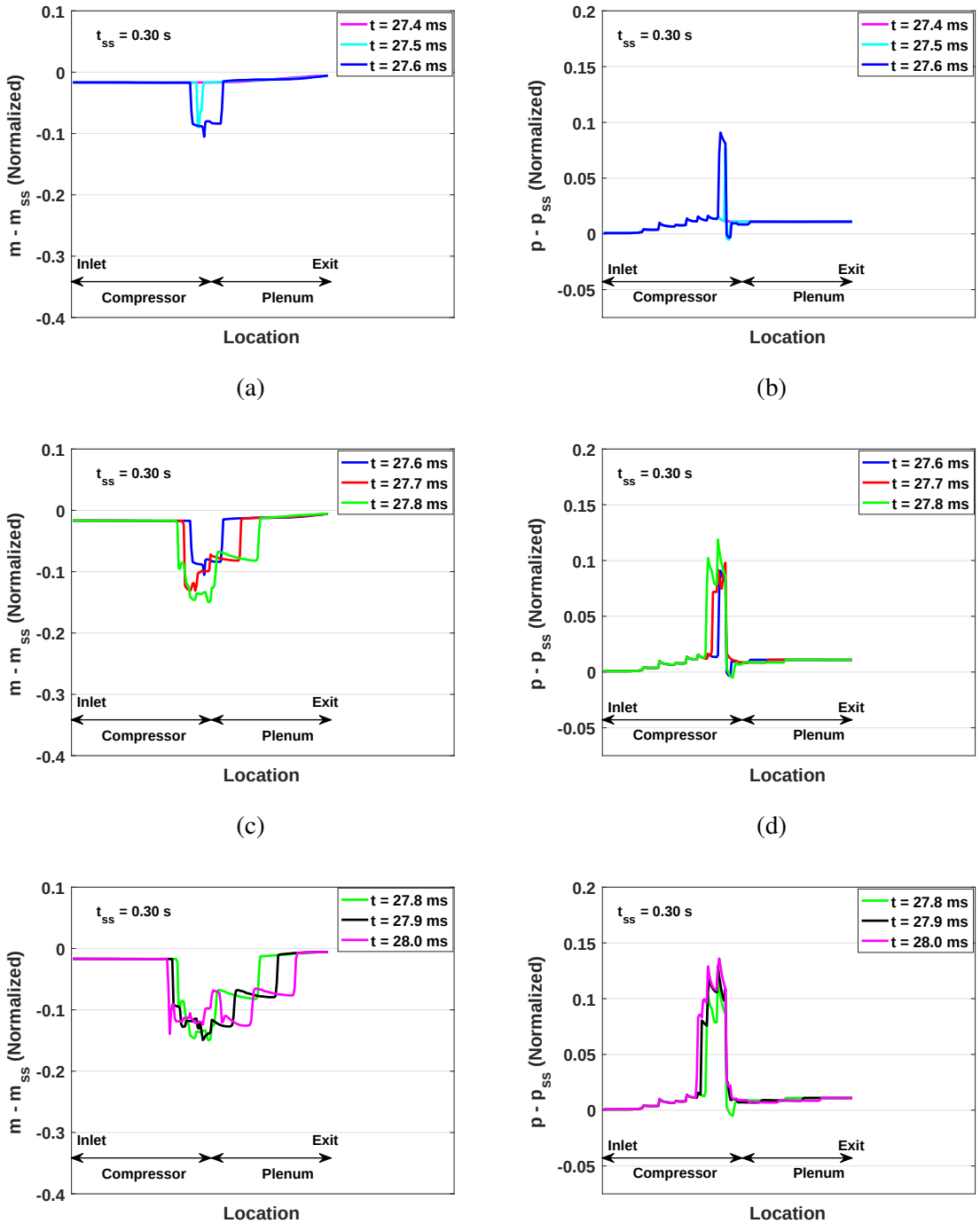

Figure 5.26: Flow rate and pressure deviation distribution during the development of stall taken from switch at $t_{ss} = 0.30$ s corresponding to Figure 5.25

much faster pressure variation of the fractions of a millisecond, as described above. This case has been simulated by increasing the stall trigger angle of attack to 20 degrees. Figure

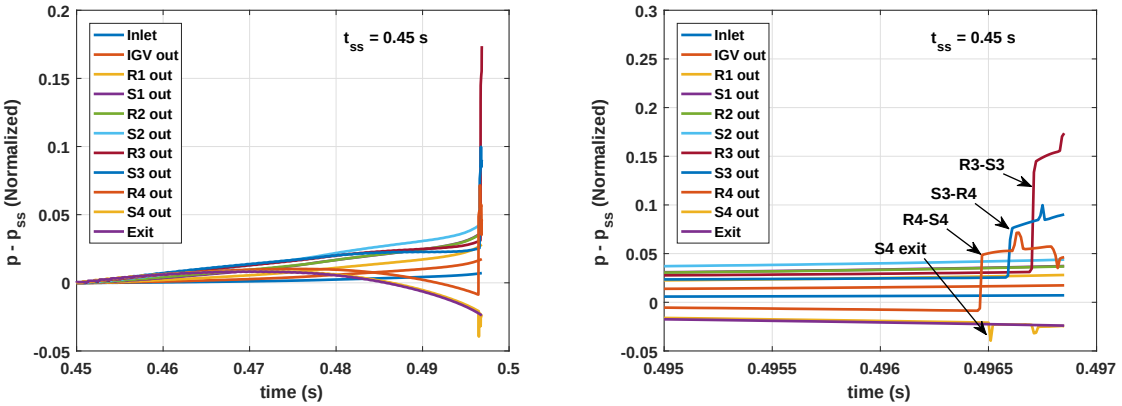

(a) (b)

Figure 5.27: (a) Time history of pressure sensor readings during a stall event, (b) refined pressure signals during last few milliseconds

5.27 shows the pressure history recorded by the virtual sensors located between rows along the compressor. This simulation shows that a sharp pressure jump appears as far back as the exit of rotor 4, while a clear pressure drop appears at the exit of stator 4, thus correctly identifying stator 4 as the source of the stall. However, this is only a partial indication of the stall, as the compressor pressure was already diverging for around 45 ms before the actual appearance of stall. The development of this instability prior to the stall is apparent by the gradual pressure drop at the back of the compressor, which starts after 20 ms of the last throttle step (analogous to the third switch, point 4 in Figure 5.7). It is interesting to note that in the front three stages, pressure was going up even as the pressure at the back was already decreasing starting from the exit of rotor 4. This pressure reversal at the back is the indication of stability loss and the flow rate at that time thus indicates the stability limit.

5.4 Summary

In this chapter, the unsteady responses of axial and axial-centrifugal compressor have been simulated using the mechanism of dynamic compact interfaces which can be seen as general boundary conditions between two domains (see Appendix B). In particular, the entire dynamics of the compressor occurs due to the addition of kinetic energy by the

main shaft and the mechanisms of stagnation pressure losses. Further, the framework of characteristics-based approach provides the right tool to implement this dynamics in a 1D model in simple and convenient manner. By setting the appropriate throttle position, features like compressor choking and stalling have been simulated along with pressure signatures that correctly give identification of the choking and stalling stages.

Furthermore, it has been demonstrated that with a large end plenum, the compressor becomes unstable close to the peak of constant speed characteristic curve. This correlates well with Greitzer's simplified theory which introduced B-parameter. With low B-parameter, i.e., simulations without any end plenum or low shaft speed, left side operation on the positively-sloped region is possible. But subsequent closing of throttle, therefore, pushes the compressor into an unstable operation. Instability modes prior to the stall have been detected in both the axial and axial-centrifugal compressors. Significantly, the simulation suggests that a general Rayleigh's like criterion that relates the oscillating energy addition to pressure fluctuations can be devised to predict the ultimate stability of the compressor without the need to refer to a specific mode including rotating stall. Finally, the model has been used to simulate the pressure sensor responses in a virtual test environment, where the stall is initiated by sudden stage collapse.

CHAPTER 6

PARAMETRIC STUDIES AND STABILITY ENHANCEMENT

The main advantage of 1D model is that it can be easily used to implement the sensitivity studies for the purpose of design optimization and improvement of stability margin. A design procedure, in general, is an iterative process where the reduced-order quasi-1D model can perform these iterations in short time. This chapter explores the sensitivity of compressor performance with respect to IGVs and stationary vane deflections.

6.1 Effect of IGVs Deflection on Compressor Performance

The guide vanes placed in front of the compressor direct flow to the first rotor at optimal angle. During the part-speed operation, these Inlet Guide Vanes (IGVs) are moved and set to a different angle for optimal performance.

In this section, sensitivity of the axial and axial-centrifugal compressor with respect to IGVs setting is studied using the steady model at the nominal speed (100% RPM). Figure 6.1 depicts the pressure ratio versus normalized flow rate for 2 degrees IGVs variation from the default setting. As shown, a 2 degree IGVs closure (+2 deg) reduces the choked flow rate by approximately 2%. In a similar manner, a 2 degree opening of IGVs (-2 deg) from the nominal setting increases this flow rate by 2%. While this linear relationship seems trivial, there is an increase in peak pressure for both the compressors as the IGVs are opened. Upon first look, this might give a false impression regarding optimal IGVs angle. But by carefully looking at the efficiency plots, as shown in Figure 6.2, it becomes clear that this improvement in peak pressure ratio is associated with lower overall efficiency. Similarly, the reduction in peak pressure ratio, as the IGVs are deflected by +2 deg, is accompanied with improved compressor efficiency. Hence, the default IGVs setting is, therefore, a trade-off between the maximum pressure ratio and maximum efficiency, thus leading to the design

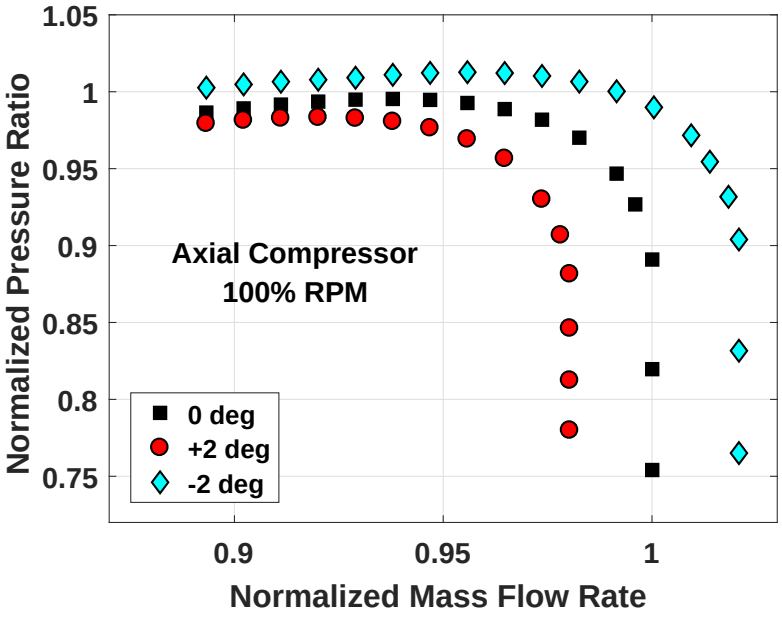

(a)

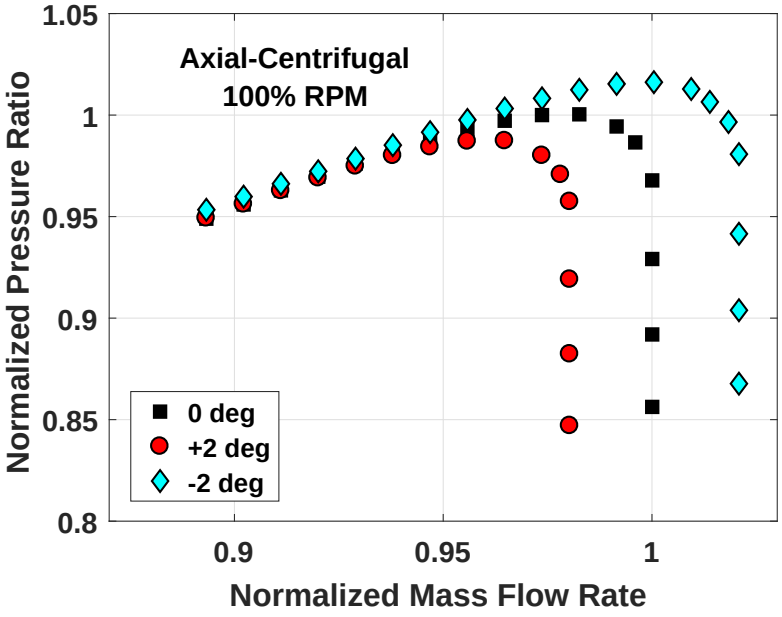

(b)

Figure 6.1: Predicted pressure ratios for the (a) axial, (b) axial-centrifugal compressor for 2 degrees IGVs deflection from the nominal setting

intent performance.

The axial-centrifugal compressor, on the other hand, is comparatively less sensitive to IGVs deflection. Apart from the difference in the choked flow rate which is governed by

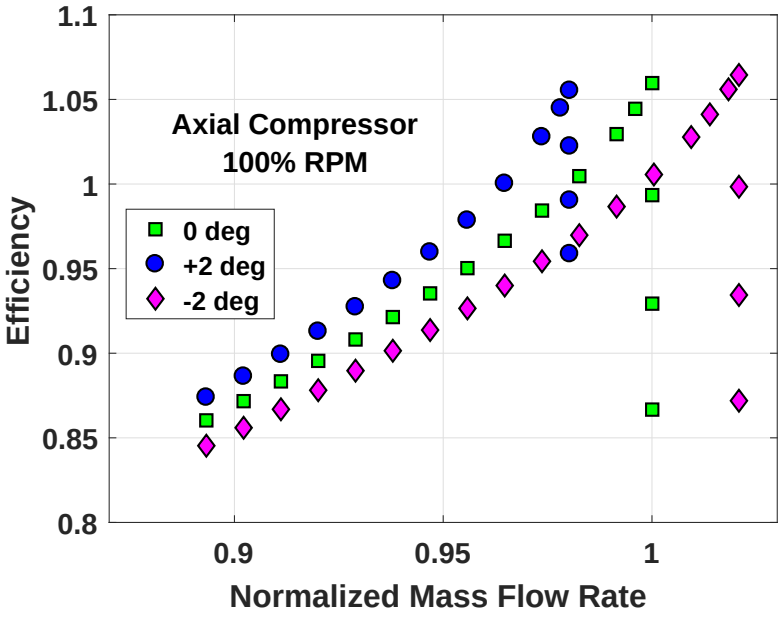

(a)

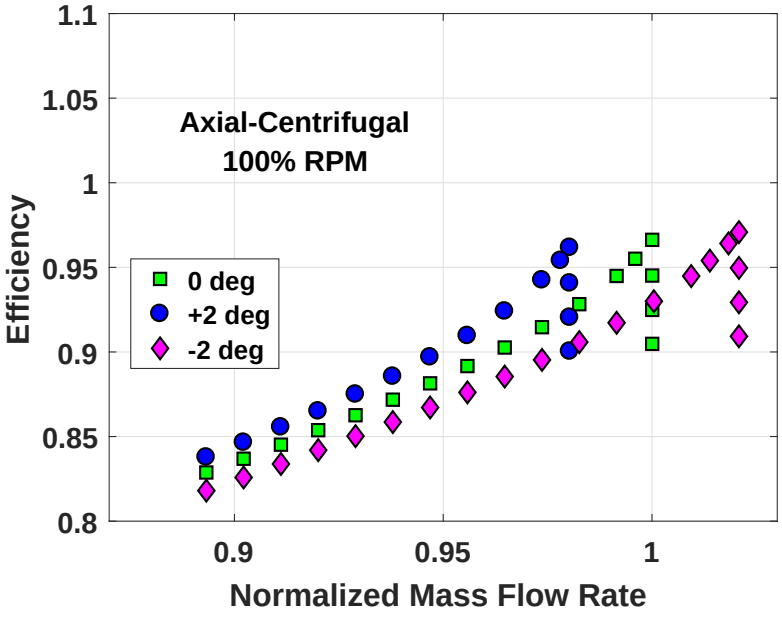

(b)

Figure 6.2: Predicted efficiencies for the (a) axial, (b) axial-centrifugal compressor for 2 degrees IGVs deflection from the nominal setting

one of the axial stages, the pressure ratios and efficiencies away from the choked branch, i.e., for lower flow rates, converge onto the same curve for the different IGVs settings.

6.2 Stationary Vane Deflection for Stability Enhancement

Next, the deflection sensitivity of final stationary vane (Stator 4) of the four-stage axial compressor from its nominal setting is studied. First three stators of this industrial compressor are designed to be variable geometry to optimize the part-speed operation. The fourth stator S4, however, is stationary and has been kept for the design optimization purposes.

For conducting S4 deflection sensitivity study, it is first offset by a selected value (in degrees) and then the compressor steady results are evaluated. The pressure ratios for axial and axial-centrifugal compressors for 5 degrees offset of stator 4 are shown in Figure 6.3. As can be observed, a positive offset leads to higher stage diffusion, thus increases the pressure ratios for both the compressors. Contrary to the earlier case of IGVs deflection, in this case, the adiabatic efficiencies hardly change (figures not shown for the sake of brevity). This gives an indication that this particular stator is not set to its optimum inlet and exit angles, thus needs to be optimized for maximum performance. Since at the nominal speed, the compressor choking is governed by the first axial stage, small S4 deflections do not affect the choked flow rate.

Next, the variations in surge flow rate for both the compressors with S4 deflection are obtained, results of which are shown in Figure 6.4. Note that in the case of large plenum attached behind the compressor, the peak is identified as the surge point, hence has been taken to represent the surge flow rate. As shown in the figure, the deviation in surge flow rate is minimal for below 10 degrees of S4 deflection. However, as the deflection is further increased, the surge flow rate reduces and at 15 degrees deflection decreases by nearly 1%. Clearly, a higher surge margin can be achieved if the stator 4 is offset by 15 degrees or more. However, it is found that a further deflection of stator 4 shifts the choking stage from front to the back of the compressor, thus reduces the choked flow rate substantially. This kind of sensitivity study can be done at part-speed operation also, to further improve the stability margin at those speeds.

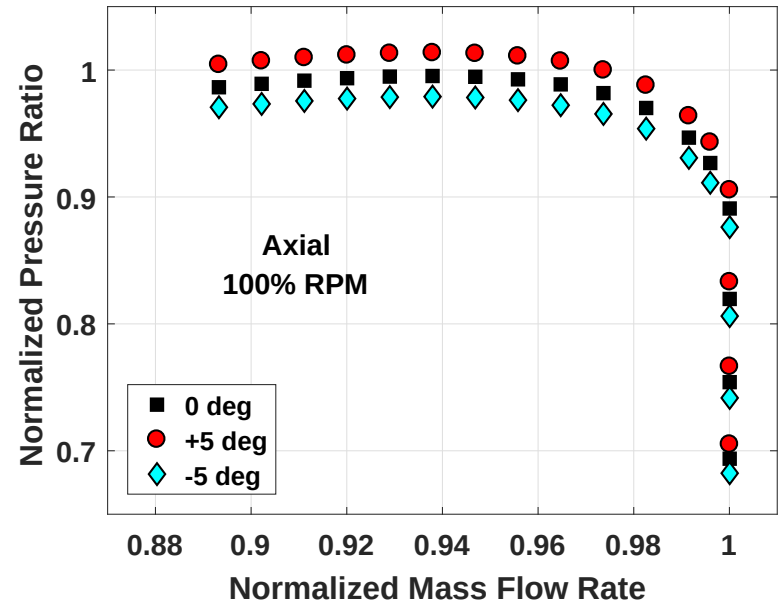

(a)

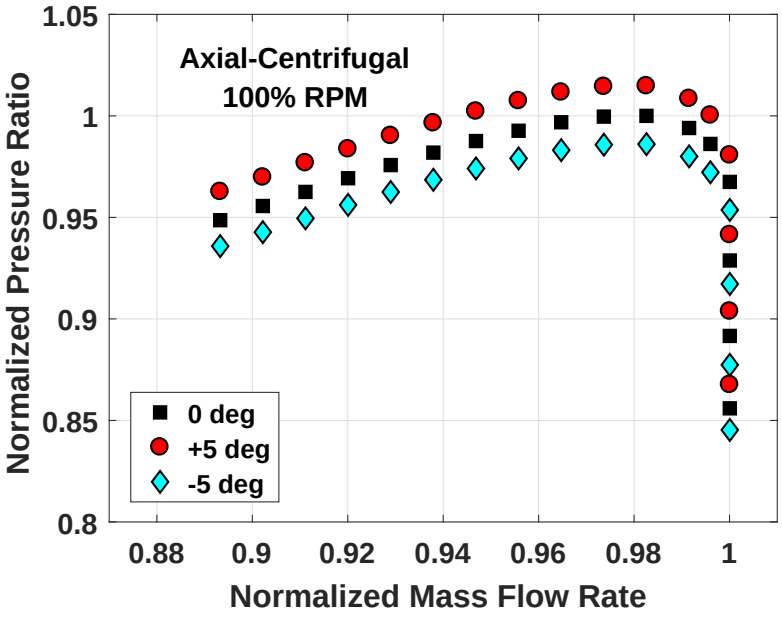

(b)

Figure 6.3: Predicted pressure ratios for the (a) axial, (b) axial-centrifugal compressor for 5 degrees stator 4 deflection from the nominal setting at 100% speed

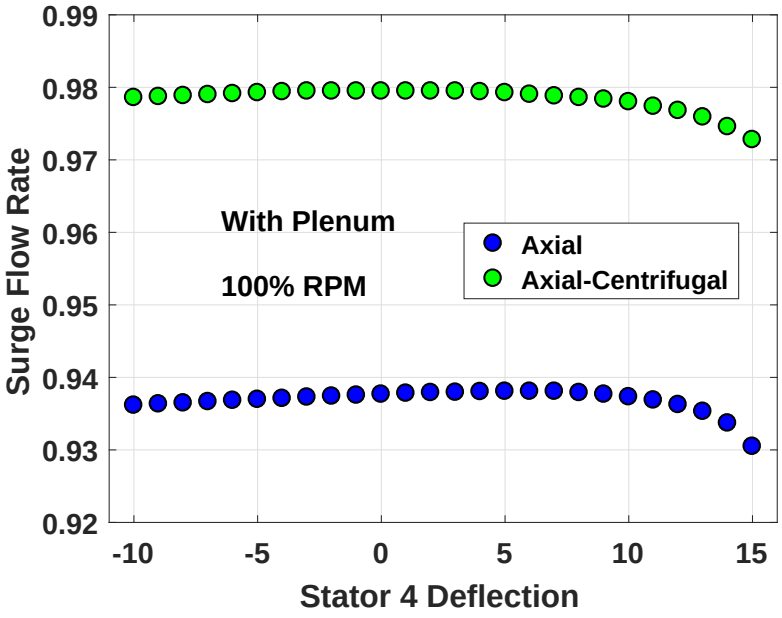

Figure 6.4: Predicted surge flow rate versus stator 4 deflection for the axial and axial-centrifugal compressor

CHAPTER 7

CONCLUSIONS AND RECOMMENDATIONS FOR FUTURE WORK

This chapter summarizes conclusions from the research work described in this thesis and outlines few recommendations for future work.

7.1 Conclusions

The main focus of this research has been on the development of a quasi-1D streamtube based fluid dynamic model through a generic compressor containing both the axial and centrifugal stages by modelling stage elements as successive diffusers. The relative rotation between the consecutive elements has been accounted through the inclusion of velocity addition junctions by the construction of vector diagrams as the reference frame is switched. During the steady state operation, an ideal compressor generates significantly higher pressure around three to four times the actual operation. But with the inclusion of appropriate mechanisms for stagnation pressure losses, the compressor pressure ratio gets lowered and matches with the measured data for an industrial compressor.

The conclusions and main findings of this study can be summarized as:

- 1D model based upon the mean-line analysis presents a viable tool to evaluate compressor performance during both at design and off-design operations. High fidelity CFD models along with core rig test data provide validation cases for the 1D model, thus help in benchmarking it for industrial or research use.

- Most of the compressor simulation tools work by taking input from the user in the form of aerodynamic/blade sources typically represented in terms of work and force coefficients. However, the model developed in this work is entirely independent of external source terms, and predicts the compressor performance through the mech-

anism of losses. The model is designed to capture off-design losses, wherein most important of all are the losses occurring due to inlet turning and subsequent blade passage mixing, which are incorporated after the formulation of the so-called *sliding scale equation*.

- Simplicity of the model lies in the fact that by the tuning of a single parameter (representative of mixing loss inside a passage) at the nominal speed, it is able to accurately predict the surge flow rate, peak pressure ratio and choked flow rate of the four stage axial compressor and is further able to validate NASA stage 37 performance at a range of speeds. It is found that the tuning process works well if the mixing loss factor ξ_{ml} is taken to be dependent on the conditions of stage incoming flow. Further, the predicted surge line using the tuned model matches well with the measured one.

- The general framework of following mean-line through the streamtubes of stage elements is physically more intuitive than just following the axial or radial coordinate. First, a mean-line can be easily constructed to track the flow quantities by accommodating both the axial and radial stages, which might not be possible in the framework constituting a single coordinate system. Second, since the axial flow is not same as the bulk flow, hence one might mistakenly assume an axial flow feature to be representative of the bulk flow. The mean-line, on the other hand, follows general blade direction, hence is a better approximation to the bulk compressor flow.

- An important contribution in this work is the formulation of novel dynamic compact interfaces to establish communication between the neighboring stage elements. It has been demonstrated that such an interface acts as a general boundary condition between two domains and can be easily modified to include various complex mechanisms like vaneless space losses, incidence loss, shock loss, trailing edge deviation etc.

- The dynamic performance of compressor is further demonstrated through unsteady simulations. Greitzer's theory which introduced B-parameter is validated by illus-

trating that a compressor becomes unstable close to the peak of constant speed characteristic when simulated with large end plenum. With reduced B-parameter, the compressor is able to operate on the left side of the peak, but settles into a limit cycle if throttled further. The transients observed during the onset of instabilities thus mimic test data and provide identification of stalling stage through the mechanism of expansion and compression waves.

- Further, it has been conceptualized that the instability modes including rotating stall occurring close to the peak of characteristic curve must be connected to the phase between pressure and shaft power oscillations through Rayleigh's criterion.

7.2 Model Usage in Design and Diagnostics

Importantly, the developed model for the compressor unsteady flow analysis can find applications in design and diagnostics. As a design tool, it would be possible to examine the effects of bulk and distributed volumes on the stability margin of the compressor. As was shown that given a large enough volume of end plenum, the compressor loses stability once the pressure characteristic reaches a local peak. However, simplified models such as described by Greitzer are insufficient in predicting how the compressor stability changes when the plenum volume is sufficiently reduced. This is due to the fact that the simplified models do not account for the "real" compressible flow effects which indicate that significant operation margin can be gained by volume reduction.

Another important aspect of instability in gas turbine is the link between combustion driven oscillations in the combustor and the compressor. It is possible that natural modes of the combustion system could couple with the natural modes of the compressor, thus studying these natural modes and their respective damping is of interest to the gas turbine designer. As a diagnostic tool, the model can be used in conjunction with the test results to find out the reason and process through which the compressor loses stability. Further, the measured pressure signals along the compressor may be correlated with the simulated

results so that the origin of the divergence can be traced. Oftentimes, it is found that the compressor loses stability even at a negative slope of the characteristic. Such a case, which is not uncommon, suggests that at least one stage went through a sudden radical change in the flow pattern. The model in conjunction with the measured data can identify the "faulty" stage. The results, as shown in Chapter 5, demonstrate this scenario by creating a sudden change in the loss function of a stage.

7.3 Recommendations for Future Work

In regard to the work presented in this thesis, further research can be conducted in the following directions:

- During the entire model development process, primary focus has been on the elimination of external source terms in the model equations and inclusion of only necessary terms. To comply with this, the flow governing equations retain only skin friction, centrifugal force and work terms. However, more complex loss mechanisms like separation loss, tip and endwall losses which are mainly three-dimensional in nature, can be converted into 1D functions and included as source terms in the unsteady equations. Ideally, this should be approached by using entropy generation function corresponding to each loss mechanism as described in the literature [36] and deriving an equivalent 1D drag function, wherever possible.

- To identify stages undergoing rotating stall and to calculate the stall speed, the quasi-1D model needs to be converted into a 2D model by including circumferential flow gradients in mass, momentum and energy equations. The comprehensive work done by Moore [3] on rotating stall was mainly concentrated towards obtaining modal solutions for the flow perturbations. In a general case, however, additional work is needed to obtain numerical solutions of the 2D governing equations using high performance computational tools.

- In the first and second tuning processes, mixing loss factor ξ_{ml} is tuned to match the measured pressure ratio at the surge flow rate. To make these tuning processes more robust, various compressor test data are required to develop a correlation measure for ξ_{ml}. Significant cost-savings during new compressor development program can be achieved, if losses inside the compressor are successfully predicted using the correlation measure.

- As the 1D model is relatively easy to handle, future work could be focused on new compressor design and geometry optimization. A number of iterations, typical of preliminary design stages, can be conducted in relatively short time to arrive at the desired geometry. Moreover, the sensitivity of geometry and model parameters on the compressor performance needs to be studied.

- The unsteady results from the 1D model accurately predict surge point and choking stage, and provide reliable estimates of the throttle change transients, at least on the qualitative level. For further benchmarking the unsteady model, the simulation results need to be quantitatively validated with either experimental data or high fidelity CFD simulations.

Appendices

APPENDIX A

A SIMPLIFIED THEORETICAL MODEL FOR TIP LEAKAGE LOSS EVALUATION

In order to model the tip clearance losses, the static pressure difference across the pressure and suction side needs to be estimated first. Let us consider the coordinate system shown in Figure A.1 and write the steady momentum equation normal to the primary flow direction m. This gives

$$\rho V^2 A \frac{\partial \theta}{\partial m} = b^2 \frac{\partial p}{\partial n} \tag{A.1}$$

where $\partial\theta/\partial m$ is the change in the flow path angle, b is a characteristic lateral dimension corresponding to channel width and blade height, and $\partial p/\partial n$ is the gradient of pressure normal to the primary flow path. Using a simplifying assumption that channel width is nearly the same as blade height, the flow path area A can be written as

$$A = b^2 \tag{A.2}$$

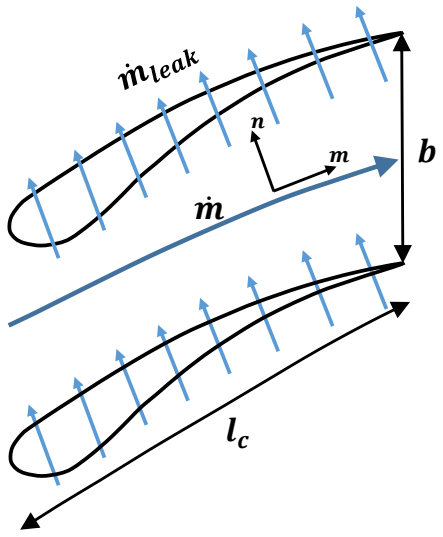

Figure A.1: Schematic of flow leaking as a jet over the blade tip clearance

Accordingly, the average pressure gradient gets expressed as

$$\frac{\partial p}{\partial n} \approx \frac{\Delta p}{b} \tag{A.3}$$

and similarly the gradient of flow path angle gets simplified to

$$\frac{\partial \theta}{\partial n} \approx \frac{\theta_c}{l_c} \tag{A.4}$$

where θ_c and l_c are the camber angle and blade chord length respectively. As per the definition of blade solidity σ, the passage dimensions can be related as

$$\sigma = \frac{l_c}{b} \tag{A.5}$$

Substituting the above formulations in equation (A.1) gives a simplified expression for the pressure difference

$$\Delta p = \frac{\rho V^2 \theta_c}{\sigma} \tag{A.6}$$

Now, let us take S_{gap} as the area over which the flow leaks into the adjacent blade. Assuming a rectangular cross section for flow leak, S_{gap} gets written down as

$$S_{gap} = \delta_{gap} l_c \tag{A.7}$$

where δ_{gap} is the tip clearance length. With a given pressure difference, the flow leakage rate through the clearance is approximated as

$$\dot{m}_{leak} = S_{gap} \sqrt{2\rho(\Delta p)} \tag{A.8}$$

Going back to equation (A.6) and noting that the bulk flow rate $\dot{m}$ is given by

$$\dot{m} = \rho V A \tag{A.9}$$

the pressure difference across the blade gets expressed as

$$\sqrt{\Delta p} = \frac{\dot{m}}{A}\sqrt{\frac{\theta_c}{\rho\sigma}} \tag{A.10}$$

Substituting equation (A.10) into equation (A.8) and using equations (A.2), (A.5) and (A.7), the ratio of leakage mass flow rate to bulk flow rate becomes

$$\frac{\dot{m}_{leak}}{\dot{m}} = \delta_{gap}\sqrt{\frac{2\sigma\theta_c}{A}} \tag{A.11}$$

In this analysis, it has been assumed that the area A is defined by a square cross-section of dimension $b \times b$, which means that the blade height is equal to b. Thus, the term $\delta_{gap}/\sqrt{A}$ is the ratio of tip gap to the blade height. Denoting this non-dimensional clearance as λ_{tip}, equation (A.11) becomes

$$\frac{\dot{m}_{leak}}{\dot{m}} = \lambda_{gap}\sqrt{2\sigma\theta_c} \tag{A.12}$$

The leakage losses occur as the kinetic energy imparted to the tip jet gets eventually dissipated. This relative reduction of kinetic energy after the dissipation is directly related to the stagnation pressure loss given in the equation (2.9). Based on this, the loss coefficient ($\omega_{tip\_leak,loss}$) can be written as

$$\omega_{tip\_leak,loss} = \frac{\dot{m}_{leak} \cdot \frac{1}{2}\rho v_{leak}^2}{\dot{m} \cdot \frac{1}{2}\rho V^2 + \dot{m}_{leak} \cdot \frac{1}{2}\rho v_{leak}^2} \tag{A.13}$$

Noting that $\dot{m} = \rho V A$ and $\dot{m}_{leak} = \rho v_{leak} S_{gap}$, equation (A.13) becomes

$$\omega_{tip\_leak,loss} = \frac{\frac{\dot{m}_{leak}^3}{S_{gap}^2}}{\frac{\dot{m}^3}{A^2} + \frac{\dot{m}_{leak}^3}{S_{gap}^2}} = \frac{\left(\frac{\dot{m}_{leak}}{\dot{m}}\right)^3}{\left(\frac{S_{gap}}{A}\right)^2 + \left(\frac{\dot{m}_{leak}}{\dot{m}}\right)^3} \tag{A.14}$$

Using equation (A.12) and noting that $S_{gap}/A = \lambda_{tip}\sigma$, the tip loss formula in its final form

gets expressed as

$$\omega_{tip\_leak,loss} = \frac{\lambda_{tip}(2\theta_c)^{3/2}\frac{1}{\sqrt{\sigma}}}{1 + \lambda_{tip}(2\theta_c)^{3/2}\frac{1}{\sqrt{\sigma}}} \tag{A.15}$$

It should be noted from above that large non-dimensional tip gap (λ_{tip}) and low solidity (σ) result in high loss.

APPENDIX B

COMPACT INTERFACE ELEMENT: A GENERAL BOUNDARY CONDITION

Boundary conditions are a subject of significant confusion that oftentimes bring upon improper implementation. The common perception of boundary is the interface between the computational domain and the ambient. However, the most general case should address the interface between two computational domains as shown schematically in Figure B.1, the classical boundary with the ambient thus being a special case.

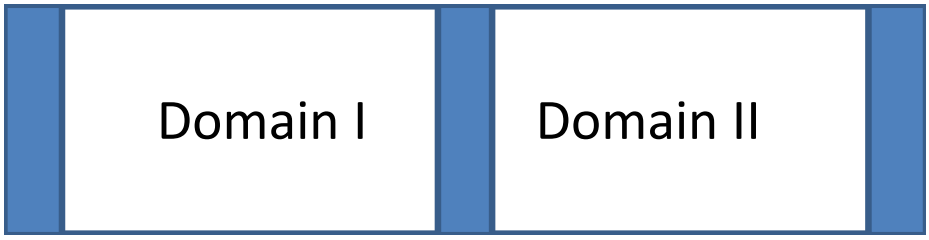

Figure B.1: Schematic of two computational domains with an interface and boundaries

Figure B.2 shows the iterative process at an internal point in the computational domain. Assuming an initial distribution of state variables, the spatial derivatives are obtained and by using Euler equations with the spatial derivatives, the time derivatives are computed, which in turn are integrated in time to update the state variables. At time t, the switch, as shown in the diagram, allows the current state variables as the initial conditions and henceforth connects the integration loop to update the state space.

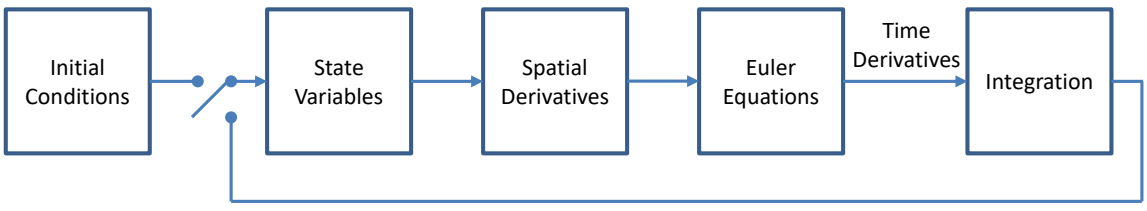

Figure B.2: Block diagram of the computational process at an internal point

Figure B.3 shows a block diagram of the computational process at the interface between

the two domains. In contrast to the internal point where the spatial derivatives obtained from the spatial distribution of the state variables are operated through Euler equations, here the spatial derivatives at the interface are modified before entering the Euler equation operation. Since, as would be seen, the focus is on using any general condition across the interface, the modifications to the derivatives cannot be calculated in a straightforward manner. Instead, this is required to be done using a trial and error process. Thus, upon obtaining the time derivatives from the Euler equations, a "trial" integration is done to obtain candidate states at the two sides of the interface. The next step requires evaluating the closeness of the proposed states to satisfy the matching conditions across the interface. It should be stressed that the interface could be quite complicated, for example, it might consist of frame transformation followed by vaneless compact space and subsequent expansion. The only condition available here is a vector of error functions pertaining to the conditions that need to be satisfied. Thus, the performed integration result is not returned to the computational domain until the errors are small enough, at which point the small error flag, through the switch, allows inclusion of the boundary states in the two domains. In the one-dimensional flow, there are three independent state variables. So, it would be not incorrect to assume that the error function will have three components as well. Thus, it can be guessed that the derivative modifier will have three modifying operators. The framework that provides intuitive tool for the

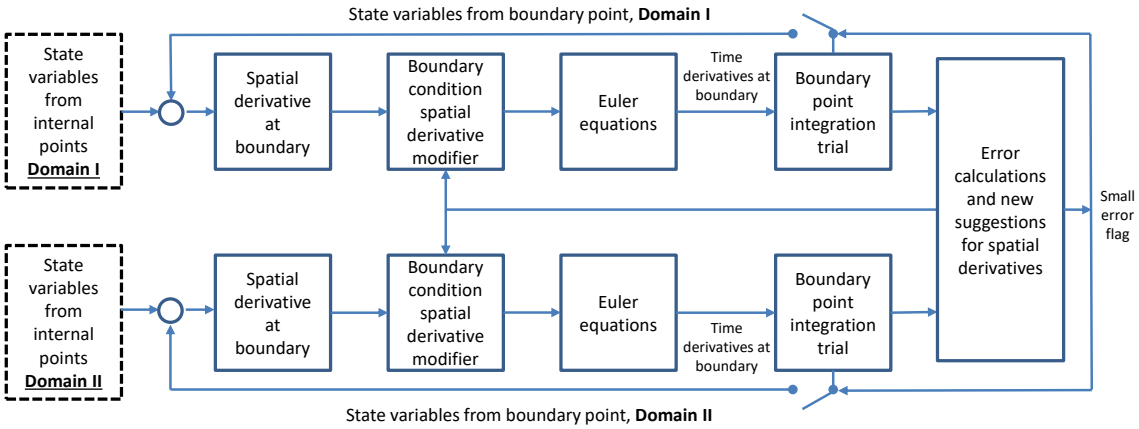

Figure B.3: Block diagram of the computational process at the interface between two domains

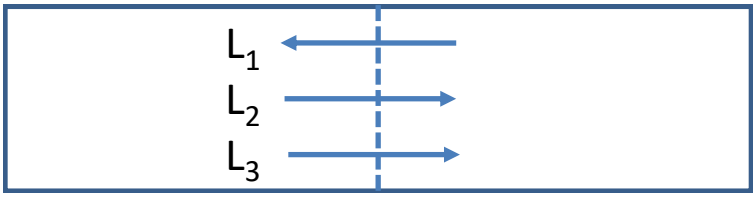

Figure B.4: Direction of characteristic waves at a grid point inside the domain

modifications is the characteristics method, the notation of which is shown in Figure B.4.

There are three characteristic velocities associated with the one-dimensional Euler equations [75] as shown below:

$$\begin{aligned} \lambda_1 &= V - c \\ \lambda_2 &= V \\ \lambda_3 &= V + c \end{aligned} \tag{B.1}$$

where c is the speed of sound, corresponding to three waves (as shown in Figure B.4), whose amplitudes are calculated using the below relations [66]:

$$L_1 = \lambda_1 \left(\frac{\partial p}{\partial m} - \rho c \frac{\partial V}{\partial m} \right) \tag{B.2}$$

$$L_2 = \lambda_2 \left(c^2 \frac{\partial \rho}{\partial m} - \frac{\partial p}{\partial m} \right) \tag{B.3}$$

$$L_3 = \lambda_3 \left(\frac{\partial p}{\partial m} + \rho c \frac{\partial V}{\partial m} \right) \tag{B.4}$$

With the above definitions, Euler equations including streamtube area variation and source terms assume the following form:

$$\frac{\partial}{\partial t}(\rho A) = -\rho V \frac{\partial A}{\partial m} - \frac{A}{c^2} \left(L_2 + \frac{1}{2}(L_1 + L_3) \right) \tag{B.5}$$

$$\begin{aligned}\frac{\partial}{\partial t}(\rho V A) = &- \rho V^2 \frac{\partial A}{\partial m} - \frac{A}{c^2}\left(\lambda_2 L_2 + \frac{1}{2}(\lambda_1 L_1 + \lambda_3 L_3)\right) \\ &+ \rho A \Omega^2 r \cos(\beta)\sin(\eta) - C_f(\rho V^2 b)\end{aligned} \tag{B.6}$$

$$\begin{aligned}\frac{\partial}{\partial t}(\rho e_s A) = &- \rho V h_s \frac{\partial A}{\partial m} - \frac{A}{2}\left[\frac{L_1}{\lambda_1}\left(\frac{\gamma V - c}{\gamma - 1} + \frac{1}{2}\frac{V^2}{c^2}(V - 3c)\right)\right. \\ &\left. + \frac{L_2}{\lambda_2}\frac{V^3}{c^2} + \frac{L_3}{\lambda_3}\left(\frac{\gamma V + c}{\gamma - 1} + \frac{1}{2}\frac{V^2}{c^2}(V + 3c)\right)\right] \\ &+ \rho V A \Omega^2 r \cos(\beta)\sin(\eta) - C_q\end{aligned} \tag{B.7}$$

Now considering the Compact Interface Element (CIE) with upstream node N_U and downstream node N_D, there are six characteristics, as can be seen in Figure 3.1, three at the upstream side and three at the downstream side. Respectively, there are six governing equations with (B.5)-(B.7) implemented at both the upstream and downstream nodes. The characteristics L_{2U}, L_{3U}, and L_{1D} are those which arrive at the interface from inner domains. These characteristics are determined from the spatial distribution of state variables (B.2)-(B.4). The other three characteristics L_{1U}, L_{2D} and L_{3D} enter each respective domain from the other domain after being modified by the boundary, those characteristics are thus determined by the boundary conditions. These boundary or matching conditions set the error functions through which the correct values of the three unknown characteristics could be found. Thus, after setting any arbitrary states at each side of the interface, the matching conditions are then used to calculate the corresponding error vector.

For demonstrating this, let us consider the following example of flow through an orifice plate shown schematically in Figure B.5, where the flow may be choked or unchoked. The flow converges isentropically from the inlet side to the throat and expands non-isentropically with losses downstream until it gets reattached to the wall at the end of the compact interface.

The three matching conditions across the interface can be devised as follows. The first

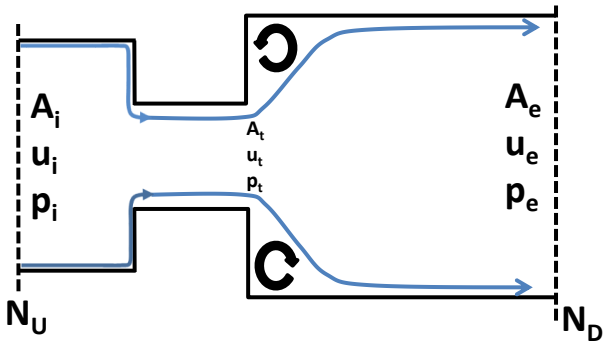

Figure B.5: Compact orifice element

condition is conservation of mass which implies

$$A_i \rho_i u_i = A_e \rho_e u_e \tag{B.8}$$

The second condition is conservation of energy, which preserves the total temperature across the compact element:

$$\frac{\gamma}{\gamma - 1}\frac{p_e}{\rho_e} + \frac{1}{2}u_e^2 = \frac{\gamma}{\gamma - 1}\frac{p_i}{\rho_i} + \frac{1}{2}u_i^2 \tag{B.9}$$

The third condition is obtained by calculating the Mach number at the throat. In the inlet section, the flow is isentropic and using the area ratio relationship the following relation is obtained:

$$\frac{A_i}{A_t} = \frac{M_t}{M_i}\left(\frac{2 + (\gamma - 1){M_i}^2}{2 + (\gamma - 1){M_t}^2}\right)^{\frac{\gamma+1}{2(\gamma-1)}} \tag{B.10}$$

It is convenient to replace M using $f(M)$ defined in equation (2.12), which thus gives

$$\frac{A_i}{A_t} = \left(\frac{1 - f_t}{1 - f_i}\right)^{\frac{1}{2}}\left(\frac{f_i}{f_t}\right)^{\frac{\gamma}{\gamma-1}} \tag{B.11}$$

On the downstream side, the relationship between throat discharge and exit section using the continuity equation gives

$$A_t \rho_t u_t = A_e \rho_e u_e = \dot{m} \tag{B.12}$$

and the energy equation simplifies to

$$\frac{\gamma}{\gamma-1}\frac{p_e}{\rho_e}+\frac{1}{2}u_e^2=\frac{\gamma}{\gamma-1}\frac{p_t}{\rho_t}+\frac{1}{2}u_t^2 \tag{B.13}$$

The momentum equation is evaluated by assuming a uniform pressure distribution at the back wall where the throat terminates and at the exit where the flow is reattached. This gives

$$\dot{m}(u_e-u_t)=A_e(p_t-p_e) \tag{B.14}$$

Using the function $f(M)$, the above equation gets recast into the following form:

$$\sqrt{1-f_t}+\frac{A_e}{A_t}\frac{\gamma-1}{2\gamma}\frac{f_t}{\sqrt{1-f_t}}=\sqrt{1-f_e}+\frac{\gamma-1}{2\gamma}\frac{f_e}{\sqrt{1-f_e}} \tag{B.15}$$

It is worth noting that equation (B.15) can be transformed into a quadratic equation by substituting $x=\sqrt{(1-f_t)}$. Denoting f_t calculated by equation (B.11) as f_{tU} and f_t calculated by equation (B.15) as f_{tD}, the matching requirement for both the choked and unchoked orifice is given by

$$f_{1U}=\begin{cases} f_{tD} & \text{if } f_{tU}\geq f^* \\ f^* & \text{otherwise} \end{cases}$$

where f^* is the sonic value. The three error functions can now be summarized as

$$\begin{aligned} E_1&=(\rho VA)_U-(\rho VA)_D \\ E_2&=\left(\frac{\gamma}{\gamma-1}\frac{p}{\rho}+\frac{1}{2}u^2\right)_U=\left(\frac{\gamma}{\gamma-1}\frac{p}{\rho}+\frac{1}{2}u^2\right)_D \end{aligned} \tag{B.16}$$

$$E_3=\begin{cases} f_{tU}-f_{tD} & \text{if } f_{tU}\geq f^* \\ f_{tU}-f^* & \text{otherwise} \end{cases}$$

APPENDIX C

NEWTON'S METHOD FOR FINDING UNKNOWN CHARACTERISTIC AMPLITUDES

This section summarizes Newton's method for determining the three unknown characteristic waves (L_{1U}, L_{2D}, L_{3D}) from the prescribed physical relations (3.15)-(3.17). Let us denote three unknown wave amplitudes as variables say $L_{1U} = x$, $L_{2D} = y$, and $L_{3D} = z$. Now for a given initial guess for $(x, y, z) = (x_0, y_0, z_0)$, three error functions can be formulated as shown below:

$$E_1(x_0, y_0, z_0) = (\rho V A)_U - (\rho V A)_D$$

$$E_2(x_0, y_0, z_0) = \left(h + \frac{1}{2}V^2\right)_U - \left(h + \frac{1}{2}V^2\right)_D$$

$$E_3(x_0, y_0, z_0) = (M_t)_U - (M_t)_D \quad \text{if } (M_t)_U < 1.0 \tag{C.1}$$

The above error functions are calculated at each time step by integrating equations (3.9)-(3.11) at the upstream node and similar equations at the downstream node. First, it is checked whether the maximum absolute value of each of the three error functions is below the specified tolerance:

$$\max(|E_1(x_0, y_0, z_0)|, |E_2(x_0, y_0, z_0)|, |E_3(x_0, y_0, z_0)|) < tol \tag{C.2}$$

where the tolerance value is taken as $tol = 10^{-6}$. If for the initial guess values, equation (C.2) is not satisfied (which generally happens), then small perturbations are introduced to

the initial guesses as shown below:

$$x_1 = x_0 + \delta x, \qquad y_1 = y_0 + \delta y, \qquad z_1 = z_0 + \delta z \tag{C.3}$$

Next, sensitivity of the error functions to these small perturbations are calculated by obtaining their partial derivatives in the direction of x, y and z. This can be expressed as

$$\begin{aligned}
\frac{\partial E_1}{\partial x} &= \frac{E_1(x_0 + \delta x, y_0, z_0) - E_1(x_0, y_0, z_0)}{\delta x} \\
\frac{\partial E_1}{\partial y} &= \frac{E_1(x_0, y_0 + \delta y, z_0) - E_1(x_0, y_0, z_0)}{\delta y} \\
\frac{\partial E_1}{\partial z} &= \frac{E_1(x_0, y_0, z_0 + \delta z) - E_1(x_0, y_0, z_0)}{\delta z} \\
\frac{\partial E_2}{\partial x} &= \frac{E_2(x_0 + \delta x, y_0, z_0) - E_2(x_0, y_0, z_0)}{\delta x} \\
\frac{\partial E_2}{\partial y} &= \frac{E_2(x_0, y_0 + \delta y, z_0) - E_2(x_0, y_0, z_0)}{\delta y} \\
&\vdots \\
\frac{\partial E_3}{\partial z} &= \frac{E_3(x_0, y_0, z_0 + \delta z) - E_3(x_0, y_0, z_0)}{\delta z}
\end{aligned} \tag{C.4}$$

The perturbations (δx, δy, δz) should be small enough to render accurate calculations for the local partial derivatives and at the same time should not be below the machine precision. Next, corrections (Δx, Δy, Δz) to the initial guesses are determined by expanding the error functions E_1, E_2 and E_3 in Taylor series around (x_0, y_0, z_0) and equating the resulting error values to zero. This gives a linear system of equations which in matrix form is shown below:

$$\begin{bmatrix} \frac{\partial E_1}{\partial x} & \frac{\partial E_1}{\partial y} & \frac{\partial E_1}{\partial z} \\ \frac{\partial E_2}{\partial x} & \frac{\partial E_2}{\partial y} & \frac{\partial E_2}{\partial z} \\ \frac{\partial E_3}{\partial x} & \frac{\partial E_3}{\partial y} & \frac{\partial E_3}{\partial z} \end{bmatrix} \begin{bmatrix} \Delta x \\ \Delta y \\ \Delta z \end{bmatrix} = - \begin{bmatrix} E_1(x_0, y_0, z_0) \\ E_2(x_0, y_0, z_0) \\ E_3(x_0, y_0, z_0) \end{bmatrix} \tag{C.5}$$

By solving equation (C.5), corrections to the initial guesses for the unknown wave amplitudes are obtained. Before obtaining the new characteristic amplitudes after this first iteration, it is generally better to scale the corrections by a relaxation factor ξ to ensure gradual convergence. Hence, the new amplitudes (L_{1U}, L_{2D}, L_{3D}) are given by

$$x_{new} = x_0 + \xi \Delta x, \qquad y_{new} = y_0 + \xi \Delta y, \qquad z_{new} = z_0 + \xi \Delta z \tag{C.6}$$

Using the updated values of x_{new}, y_{new}, and z_{new}, the errors are further calculated as per equation (C.1). Then, the equation (C.2) is checked, and if required, the process is repeated until the convergence is achieved.

It should be noted that the procedure described above is quite general and can be followed in a similar manner to implement the inlet boundary condition with two error functions and the outlet boundary condition with one error function.

REFERENCES

[1] F. K. Moore and E. M. Greitzer, "A theory of post-stall transients in axial compression systems: Part I–Development of equations," *ASME J. Eng. Gas Turbines Power*, vol. 108, no. 1, pp. 68–76, 1986.

[2] E. M. Greitzer and F. K. Moore, "A theory of post-stall transients in axial compression systems: Part II–Application," *ASME J. Eng. Gas Turbines Power*, vol. 108, no. 2, pp. 231–239, 1986.

[3] F. K. Moore, "A theory of rotating stall of multistage axial compressors: Part I–Small disturbances; Part II–Finite disturbances; Part III–Limit cycles," *ASME J. Eng. Gas Turbines Power*, vol. 106, no. 2, pp. 313–334, 1984.

[4] I. J. Day, "Axial compressor performance during surge," *Journal of Propulsion and Power*, vol. 10, no. 3, pp. 329–336, 1994.

[5] I. J. Day, "Stall inception in axial flow compressors," *Journal of Turbomachinery*, vol. 115, pp. 1–9, 1993.

[6] L. He, "Computational study of rotating-stall inception in axial compressors," *Journal of Propulsion and Power*, vol. 13, no. 1, pp. 31–38, 1997.

[7] K. Suder and C. S. Tan, "Three-dimensional aerodynamic instability in multi-stage axial compressors," no. NASA NRA Grant NAG3-2101, May 2003.

[8] O. Léonard and O. Adam, "A quasi-one-dimensional CFD model for multistage turbomachines," *Journal of Thermal Science*, vol. 17, no. 1, pp. 7–20, 2008.

[9] M. Dhingra, J. V. R. Prasad, P. Tiwari, T. Nakano, and A. Breeze-Stringfellow, "Impact of inter-stage dynamics on stalling stage identification," in *ASME 2011 Turbo Expo: Turbine Technical Conference and Exposition*, 2011, pp. 1799–1808.

[10] R. Kundu, J. V. R. Prasad, and Y. Neumeier, "Validation of a 1D transient simulation model of a multistage axial compressor," in *ASME 2015 Gas Turbine India Conference*, American Society of Mechanical Engineers, 2015, V001T01A010–V001T01A010.

[11] K. K. Botros and S. T. Ganesan, "Dynamic instabilities in industrial compression systems with centrifugal compressors," in *Proceedings of the Turbomachinery Symposium*, 2008, pp. 119–132.

[12] J. F. Sellers and C. J. Daniele, "DYNGEN: A program for calculating steady-state and transient performance of turbojet and turbofan engines," no. NASA TN D-7901, NASA Lewis Research Center, Apr 1975.

[13] R. M. Plencner, "Plotting component maps in the Navy/NASA Engine Program (NNEP): A method and its usage," no. NASA TM-101433, NASA Lewis Research Center, Jan 1989.

[14] J. P. Veres, "Axial and centrifugal compressor mean line flow analysis method," no. NASA TM-2009-215585, NASA Glenn Research Center, Nov 2009.

[15] R. J. Steinke, "STGSTK: A computer code for predicting multistage axial flow compressor performance by a meanline stage stacking method," no. NASA-TP-2020, NASA Glenn Research Center, Jun 1982.

[16] J. F. Schmidt, "BRSTK guide: A meanline blade-row, characteristic, off-design, computer code for calculating the aerodynamic performance of axial flow fans and compressors," *NASA NPSS Document# BRSTK*, 2005.

[17] M. S. Johnson, "One-dimensional, stage-by-stage, axial compressor performance model," in *ASME 1991 International Gas Turbine and Aeroengine Congress and Exposition*, American Society of Mechanical Engineers, 1991, V001T01A070–V001T01A070.

[18] A. Hale and M. Davis, "DYNamic turbine engine compressor code (DYNTECC)-theory and capabilities," in *28th Joint Propulsion Conference and Exhibit*, 1992, p. 3190.

[19] M. Mansour, S. Hingorani, and Y. Dong, "A new multistage axial compressor designed with the APNASA multistage CFD code: Part 1–Code calibration," in *ASME Turbo Expo 2001: Power for Land, Sea, and Air*, American Society of Mechanical Engineers, 2001, V001T03A045–V001T03A045.

[20] Y. Dong, M. Mansour, S. Hingorani, and J. Hayes, "A new multistage axial compressor designed with the APNASA multistage CFD code: Part 2–Application to a new compressor design," in *ASME Turbo Expo 2001: Power for Land, Sea, and Air*, American Society of Mechanical Engineers, 2001, V001T03A046–V001T03A046.

[21] J. J. Adamczyk, R. A. Mulac, and M. L. Celestina, "A model for closing the inviscid form of the average-passage equation system," in *ASME 1986 International Gas Turbine Conference and Exhibit*, American Society of Mechanical Engineers, 1986, V001T01A097–V001T01A097.

[22] R. H. Aungier, "Mean streamline aerodynamic performance analysis of centrifugal compressors," *Journal of Turbomachinery*, vol. 117, no. 3, pp. 360–360, 1995.

[23] R. H. Aungier, "Aerodynamic performance analysis of vaned diffusers," *Fluid Machinery Components, ASME FED*, vol. 101, pp. 27–44, 1990.

[24] R. H. Aungier, "Aerodynamic design and analysis of vaneless diffusers and return channels," in *ASME 1993 International Gas Turbine and Aeroengine Congress and Exposition*, 1993, V001T03A042–V001T03A042.

[25] F. J. Wiesner, "A review of slip factors for centrifugal impellers," *Journal of Engineering for Power*, vol. 89, no. 4, pp. 558–566, 1967.

[26] S. Kulkarni, T. A. Beach, and G. J. Skoch, "Computational study of the CC3 impeller and vaneless diffuser experiment," in *49th AIAA/ASME/SAE/ASEE Joint Propulsion Conference*, 2013, p. 3631.

[27] E. P. Braunscheidel, G. E. Welch, G. J. Skoch, G. Medic, and O. P. Sharma, "Aerodynamic performance of a compact, high work-factor centrifugal compressor at the stage and subcomponent level," no. NASA/TM2015-218455, 2015.

[28] M. R. Galvas, "Fortran program for predicting off-design performance of centrifugal compressors," no. NASA TN D-7487, 1973.

[29] D. Li, C. Yang, B. Zhao, M. Zhou, M. Qi, and J. Zhang, "Investigation on centrifugal impeller in an axial-radial combined compressor with inlet distortion," *Journal of Thermal Science*, vol. 20, no. 6, pp. 486–494, 2011.

[30] F. A. H. Breugelmans, Y. Carels, and M. Demuth, "Influence of dihedral on the secondary flow in a two-dimensional compressor cascade," *Journal of Engineering for Gas Turbines and Power*, vol. 106, no. 3, pp. 578–584, 1984.

[31] T. Sasaki and F. Breugelmans, "Comparison of sweep and dihedral effects on compressor cascade performance," *Journal of Turbomachinery*, vol. 120, no. 3, pp. 454–463, 1998.

[32] V. E. Garzon and D. L. Darmofal, "Impact of geometric variability on axial compressor performance," in *ASME Turbo Expo 2003, collocated with the 2003 International Joint Power Generation Conference*, American Society of Mechanical Engineers, 2003, pp. 1199–1213.

[33] M. B. Graf, T. S. Wong, E. M. Greitzer, F. E. Marble, C. S. Tan, H.-W. Shin, and D. C. Wisler, "Effects of non-axisymmetric tip clearance on axial compressor performance and stability," in *ASME 1997 International Gas Turbine and Aeroengine Congress and Exhibition*, American Society of Mechanical Engineers, 1997, V001T03A066–V001T03A066.

[34] Y. Sheoran, B. Bouldin, and P. M. Krishnan, "Compressor performance and operability in swirl distortion," in *ASME Turbo Expo 2010: Power for Land, Sea, and Air*, American Society of Mechanical Engineers, 2010, pp. 2453–2464.

[35] M. Inoue and N. Cumpsty, "Experimental study of centrifugal impeller discharge flow in vaneless and vaned diffusers," *Journal of Engineering for Gas Turbines and Power*, vol. 106, no. 2, pp. 455–467, 1984.

[36] J. D. Denton, "Loss mechanisms in turbomachines," in *ASME 1993 International Gas Turbine and Aeroengine Congress and Exposition*, American Society of Mechanical Engineers, 1993, V002T14A001–V002T14A001.

[37] D. E. Halstead, D. C. Wisler, T. H. Okiishi, G. J. Walker, H. P. Hodson, and H.-W. Shin, "Boundary layer development in axial compressors and turbines: Part 1 of 4–Composite picture," *Journal of Turbomachinery*, vol. 119, no. 1, pp. 114–127, 1997.

[38] D. E. Halstead, D. C. Wisler, T. H. Okiishi, G. J. Walker, H. P. Hodson, and H.-W. Shin, "Boundary layer development in axial compressors and turbines: Part 2 of 4–Compressors," *Journal of Turbomachinery*, vol. 119, no. 3, pp. 426–444, 1997.

[39] D. E. Halstead, D. C. Wisler, T. H. Okiishi, G. J. Walker, H. P. Hodson, and H.-W. Shin, "Boundary layer development in axial compressors and turbines: Part 3 of 4–LP turbines," *Journal of Turbomachinery*, vol. 119, no. 2, pp. 225–237, 1997.

[40] D. E. Halstead, D. C. Wisler, T. H. Okiishi, G. J. Walker, H. P. Hodson, and H.-W. Shin, "Boundary layer development in axial compressors and turbines: Part 4 of 4–Computations and analyses," *Journal of Turbomachinery*, vol. 119, no. 1, pp. 128–139, 1997.

[41] C. Koch and L. Smith, "Loss sources and magnitudes in axial-flow compressors," *Journal of Engineering for Power*, vol. 98, no. 3, pp. 411–424, 1976.

[42] C. Koch, "Stalling pressure rise capability of axial flow compressor stages," *Journal of Engineering for Power*, vol. 103, no. 4, pp. 645–656, 1981.

[43] E. M. Greitzer, "The stability of pumping systems–The 1980 Freeman scholar lecture," *Journal of Fluids Engineering*, vol. 103, pp. 193–242, 1981.

[44] E. M. Greitzer, C. S. Tan, and M. B. Graf, *Internal flow: concepts and applications*. Cambridge University Press, 2007, vol. 3.

[45] E. M. Greitzer, "Surge and rotating stall in axial flow compressors: Part I–Theoretical compression system model; Part II–Experimental results and comparison with theory," *Journal of Engineering for Power*, vol. 98, no. 2, pp. 190–211, 1976.

[46] H. W. Emmons, C. E. Pearson, and H. P. Grant, "Compressor surge and stall propagation," *Trans. ASME*, vol. 77, pp. 455–469, 1955.

[47] S. Lieblein, "Experimental flow in two-dimensional cascades," *NASA Special Publication*, vol. 36, p. 183, 1965.

[48] J. Dunham, "Non-axisymmetric flows in axial compressors," *Mechanical Engineering Science Monograph, MESM*, no. 3, 1965.

[49] H. Oertel, M. Bohle, D. Etling, U. Muller, U. Riedel, K. R. Sreenivasan, and J. Warnatz, *Prandtl's Essentials of Fluid Mechanics*, Second Edition. Springer Science & Business Media, 2004, vol. 158, pp. 163–165.

[50] H. Schlichting, *Boundary-Layer Theory*, Seventh Edition. McGraw Hill Book Company, New York, 1979.

[51] A. Mishra, Y. Neumeier, J. V. R. Prasad, and D. K. James, "Modelling of multistage axial compressor using successive diffusers with velocity sources: Part I–Steady state results," in *53rd AIAA/SAE/ASEE Joint Propulsion Conference*, 2017, p. 4734.

[52] Y. Senoo and M. Ishida, "Pressure loss due to the tip clearance of impeller blades in centrifugal and axial blowers," *Journal of Engineering for Gas Turbines and Power*, vol. 108, no. 1, pp. 32–37, 1986.

[53] A. D. S. Carter, *The Low Speed Performance of Related Aerofoils in Cascade*, Report No. R.55. Ministry of Supply, National Gas Turbine Establishment, 1950.

[54] A. D. S. Carter, *The Calculation of Optimum Incidences for Aerofoils*, C. P. No. 646. Ministry of Aviation, Aeronautical Research Council, 1963.

[55] S. J. Andrews, "Tests related to the effect of profile shape and camber-line on compressor cascade performance," *Aeronautical Research Council, R&M*, no. 2743, 1949.

[56] A. Yocum and W. O'Brien, "Separated flow in a low-speed two-dimensional cascade: Part I–Flow visualization and time-mean velocity measurements," *Journal of turbomachinery*, vol. 115, no. 3, pp. 409–420, 1993.

[57] V. Chandavari and S. Palekar, "Diffuser angle control to avoid flow separation," *Int. J. Tech. Res. Appl*, vol. 2, no. 5, pp. 16–21, 2014.

[58] J. D. Stanitz, "Some theoretical aerodynamic investigations of impellers in radial and mixed flow centrifugal compressors," ASME, 1952.

[59] P. L. Roe, "Approximate Riemann solvers, parameter vectors, and difference schemes," *Journal of Computational Physics*, vol. 43, no. 2, pp. 357–372, 1981.

[60] R. Mohanraj, Y. Neumeier, and B. T. Zinn, "Characteristic-based treatment of source terms in Euler equations for Roe scheme," *AIAA Journal*, vol. 37, no. 4, pp. 417–424, 1999.

[61] P. D. Lax, "Weak solutions of nonlinear hyperbolic equations and their numerical computation," *Communications on Pure and Applied Mathematics*, vol. 7, no. 1, pp. 159–193, 1954.

[62] A. Kurganov and E. Tadmor, "New high-resolution central schemes for nonlinear conservation laws and convection–diffusion equations," *Journal of Computational Physics*, vol. 160, no. 1, pp. 241–282, 2000.

[63] L. He, "Computational study of rotating-stall inception in axial compressors," *Journal of Propulsion and Power*, vol. 13, no. 1, pp. 31–38, 1997.

[64] M. D. Griffin and J. D. Anderson Jr., "On the application of boundary conditions to time dependent computations for quasi one-dimensional fluid flows," *Computers & Fluids*, vol. 5, no. 3, pp. 127–137, 1977.

[65] T. J. Poinsot and S. K. Lele, "Boundary conditions for direct simulations of compressible viscous flows," *Journal of Computational Physics*, vol. 101, no. 1, pp. 104–129, 1992.

[66] K. W. Thompson, "Time dependent boundary conditions for hyperbolic systems," *Journal of Computational Physics*, vol. 68, no. 1, pp. 1–24, 1987.

[67] J. D. Anderson, *Modern Compressible Flow: With Historical Perspective*. McGraw-Hill New York, 1982.

[68] L. Reid and R. D. Moore, "Design and overall performance of four highly loaded, high speed inlet stages for an advanced high-pressure-ratio core compressor," no. NASA TP-1337, Oct 1978.

[69] K. Toyama, P. Runstadler, and R. Dean, "An experimental study of surge in centrifugal compressors," *Journal of Fluids Engineering*, vol. 99, no. 1, pp. 115–124, 1977.

[70] G. Medic, O. P. Sharma, J. Jongwook, L. W. Hardin, D. C. McCormick, W. T. Cousins, E. A. Lurie, A. Shabbir, B. M. Holley, and P. R. Van Slooten, "High efficiency centrifugal compressor for rotorcraft applications," no. NASA/CR2014-218114/REV1, 2014.

[71] T. R. Camp and I. J. Day, "1997 best paper award–Turbomachinery committee: A study of spike and modal stall phenomena in a low-speed axial compressor," *Journal of Turbomachinery*, vol. 120, no. 3, pp. 393–401, 1998.

[72] D. Durox, T. Schuller, N. Noiray, A.-L. Birbaud, and S. Candel, "Rayleigh criterion and acoustic energy balance in unconfined self-sustained oscillating flames," *Combustion and Flame*, vol. 156, no. 1, pp. 106–119, 2009.

[73] I. J. Day, T. Breuer, J. Escuret, M. Cherrett, and A. Wilson, "Stall inception and the prospects for active control in four high speed compressors," in *ASME 1997 International Gas Turbine and Aeroengine Congress and Exhibition*, American Society of Mechanical Engineers, 1997, V004T15A022–V004T15A022.

[74] B. Hellmich and J. R. Seume, "Causes of acoustic resonance in a high-speed axial compressor," *Journal of Turbomachinery*, vol. 130, no. 3, p. 031 003, 2008.

[75] M. A. Saad, *Compressible fluid flow*, Second Edition. Englewood Cliffs, NJ, Prentice-Hall, Inc., 1985.

VITA

Abhishek Mishra was born in Jaipur, India on July 20, 1991. He earned his Bachelor of Engineering (B.E.) with Honours from Birla Institute of Technology and Science (BITS), Pilani in the summer of 2012 and Master of Engineering (M.E.) from Indian Institute of Science, Bangalore in 2014. Subsequently, he worked for COMSOL Multiphysics Private Limited in Bangalore as an Applications Engineer on a variety of model problems related to fluid dynamics, heat transfer, electrochemistry, transport phenomena among several others. Starting in Fall 2015, he joined the school of aerospace engineering at Georgia Institute of Technology, Atlanta for his doctoral studies and conducted research in the area of compressor reduced-order flow modelling. He is a student member of American Institute of Aeronautics and Astronautics, American Society of Mechanical Engineers and American Physical Society.